Università degli Studi di Padova

Dipartimento di Fisica

SCUOLA DI DOTTORATO DI RICERCA IN FISICA

CICLO XXIV°

Isomer decay spectroscopy in the region of neutron-rich lead isotopes from relativistic ^{238}U fragmentation

Direttore della Scuola : Ch.mo Prof. Andrea Vitturi

Supervisori : Ch.mo Prof. Santo Lunardi,

Dott. José Javier Valiente Dobón

Dottorando : Andrea Gottardo

And we are put on earth a little space,
That we may learn to bear the beams of love
And these black bodies and this sunburnt face
Is but a cloud, and like a shady grove.

The Little Black Boy – William Blake

Contents

Summary

The present thesis describes the results of an experiment which was performed at the GSI laboratory, Darmstadt, Germany in September 2009, aiming at studying neutron-rich nuclei in the region of lead nuclei. In the introduction the main modern research lines on nuclear structure are briefly described. A particular attention is devoted to the study of exotic nuclei, i.e. of nuclei far from the valley of stability. They are one of the most important themes of research in nuclear physics since their study may point out details of the nuclear interaction not easy to disentangle investigating only stable nuclei. Moreover, significant modifications of the nuclear structure are expected, as the disappearance of the known magic numbers and the appearance of new ones. The study of neutron-rich nuclei is also fundamental to quantitatively understand the nucleosynthesis of heavy elements via the rapid process thought to happen in supernovae.
However, the study of exotic nuclei is hampered by many difficulties, concerning both their production and their measurement. The region of neutron-rich lead nuclei, which is the object of the present thesis, has proved quite complicate to study due to the fact that these isotopes cannot be populated via fusion-evaporation or deep-inelastic reactions using stable beams. Therefore, other production mechanisms must be exploited, as the fragmentation reactions. The drawbacks of this method are the low production cross sections and the necessity of using high-energy uranium beams ($\sim$1 GeV·A) in order to facilitate the separation in mass and atomic number. As a consequence, the neutron-rich isotopes around doubly-magic ^{208}Pb have been less investigated with respect to regions with lower mass, as for example those around doubly-magic ^{132}Sn and ^{78}Ni. Nevertheless, these isotopes are very important. On the one hand, they are fundamental for evaluating the evolution of the nuclear shell structure beyond N = 126. On the other hand, the measurement of the β half lives of these nuclei is of paramount importance to better parameterize the models from which the half lives of the nuclei directly involved the rapid process stellar nucleosynthesis have to be extrapolated.
The exotic nuclei close to lead were produced by the fragmentation of a relativistic uranium beam at an energy of 1 GeV·A. The available energy and beam current, around 10^9 particles per second (pps), allowed to cope with the aforementioned mass separation issue and to have a sufficient production yield, despite the low cross sections. The reaction products were separated with the mass spectrometer FRagment Separator (FRS), which allows one to select the channels of interest and to identify, event by event, the

produced ions in mass and atomic number. The identified fragments were then slowed down in a degrader and implanted in double-sided silicon-strip detector, which allows one to measure the time and the position of the implantation. This array also detects the β decay of the implanted isotopes, by revealing the produced electrons. This implantation setup is surrounded by the high-efficiency γ array RISING, composed of 105 germanium crystals. Its purpose is to measure energy and time of the γ rays emitted in the isomer or β decay of the implanted ions.

Employing the described setup, new isomers in the even-even lead isotopes ^{212,214,216}Pb were identified. The excitation spectrum of such nuclei, observed for the first time, follows the seniority scheme as expected for semi-magic nuclei outside a double shell closure. From the measurement of the isomer lifetimes the electromagnetic transition matrix elements are deduced. They are a sensitive probe of the nuclear wave function and hence their comparison with theoretical predictions indicates to which extent the nuclear models employed are able to reproduce the nuclear structure. The observed significant experimental discrepancies with the shell-model calculations (derived from realistic nuclear hamiltonian with state-of-the-art shell-model codes) require the introduction of state-dependent effective charges. It is shown that this need is actually the result of neglecting of effective three-body forces. These forces appear when an interaction is adapted to a certain valence space, but are almost always not considered as they are thought to produce negligible effects. In the present thesis it is proved that, on the contrary, these forces can produce significant changes on the final results of the calculations.

Isomers were also observed in ^{217}Bi, ^{213}Pb, ^{211,213}Tl and ^{208,210}Hg. The assignment of spin and parity to the levels in ^{217}Bi and ^{208}Hg was straightforward, whereas in the other isotopes it was more challenging.

In conclusion, the present work reports results on several new isomers in the neutron-rich nuclei in the lead region. The technical difficulties of the experiment and the devices exploited to overcome them are also highlighted. The physical cases studied appear very interesting, as they point out previously neglected aspects of the nuclear structure. The future investigations that will be possible with the new accelerators and detection setups under construction will shed more light on these issues.

Riassunto

La presente tesi di dottorato descrive la preparazione ed i risultati di un esperimento svoltosi presso il laboratorio del GSI, Darmstadt, Germania nel settembre 2009. Nella parte introduttiva si descrivono brevemente le principali linee della moderna ricerca sulla struttura nucleare. Particolare risalto viene dato alla tematica dello studio dei nuclei esotici, cioè lontani dalla valle di stabilità. Essi costituiscono uno dei più importanti obbiettivi di ricerca della fisica nucleare, poiché il loro studio metterà in evidenza aspetti dell'interazione nucleare altrimenti difficili da comprendere. Inoltre, ci si aspettano significativi cambiamenti della struttura del nucleo, come la scomparsa degli usuali numeri magici e l'apparizione di nuovi. Lo studio dei nuclei ricchi di neutroni è anche fondamentale per comprendere quantitativamente la nucleosintesi degli elementi pesanti nel processo rapido, che si pensa accada nelle supernovae.
Lo studio dei nuclei esotici presenta tuttavia numerose difficoltà, legate sia alla loro produzione che alla loro misura. La regione dei nuclei di piombo ricchi di neutroni si è infatti rivelata particolarmente complicata da studiare poiché questi isotopi non possono essere popolati con reazioni di fusione-evaporazione o di trasferimento di nucleoni usando fasci stabili. Quindi devono essere sfruttati altri meccanismi di produzione, come le reazioni di frammentazione. Questo metodo ha però degli svantaggi, come le basse sezioni d'urto di produzione e la necessità di disporre di fasci di uranio ad alta energia ($\sim$1 GeV·A) al fine di agevolare la separazione in massa e in numero atomico. Conseguenza di ciò è il fatto che gli isotopi ricchi di neutroni nella zona del nucleo doppio magico ^{208}Pb, siano stati assai meno studiati rispetto a regioni di massa inferiore, come per esempio quelle attorno ai nuclei doppio magici ^{132}Sn e ^{78}Ni. Pur tuttavia questi isotopi sono estremamente interessanti. Da un lato essi sono fondamentali per valutare l'evoluzione della struttura a shell nucleare allontanandosi dal ^{208}Pb, cercando di capire se le chiusure di shell Z = 82 e N = 126 permangano tali. D'altra parte la misura della vita media per decadimento β di questi nuclei è di vitale importanza per parametrizzare meglio i modelli dai quali poi si devono estrapolare le vite medie degli isotopi direttamente coinvolti nel processo rapido di nucleosintesi stellare.
I nuclei esotici vicini al piombo sono stati prodotti mediante frammentazione di un fascio di uranio relativistico ad una energia di 1 GeV·A. L'energia e la corrente di fascio disponibili, circa 10^9 particelle per secondo, hanno permesso di affrontare i problemi appena menzionati riguardanti la separazione in massa e di avere una produzione sufficiente

dei nuclei di interesse, nonostante le basse sezioni d'urto. I prodotti di reazione sono stati separati con lo spettrometro di massa FRS, che permette di selezionare i canali di interesse e identificare gli ioni prodotti in massa e in numero atomico, evento per evento. I frammenti così identificati sono quindi stati rallentati in un degrader e poi impiantati in un rivelatore a strip di silicio, che permette di misurare tempo e posizione dell'impianto. Questo rivelatore permette inoltre di studiare il decadimento β degli isotopi in esso fermati, misurando gli elettroni prodotti. Questo rivelatore è circondato da un apparato ad alta efficienza per la misura di fotoni γ, RISING, composto da 105 cristalli di germanio. Il compito di RISING è quello di misurare energia e tempo dei raggi γ emessi nel decadimento degli isomeri o nel decadimento β degli ioni impiantati.
Utilizzando gli apparati descritti, si sono studiati gli isomeri negli isotopi pari-pari del piombo ^{212,214,216}Pb. Il loro spettro di eccitazione, studiato per la prima volta, segue molto bene lo schema di seniorità previsto in questi casi. La misura delle vite medie degli isomeri ha inoltre permesso di ricavare gli elementi di matrice di transizione elettromagnetica. Essi rappresentano una sonda molto accurata della funzione d'onda nucleare e quindi la loro comparazione con le stime teoriche consente di stabilire se i modelli nucleari impiegati sono veramente in grado di riprodurre la struttura del nucleo. Le discrepanze che si sono osservate rispetto calcoli di modello a shell (effettuati con hamiltoniani realistici e i più moderni codici di calcolo), richiederebbero l'introduzione di cariche efficaci dipendenti dallo stato per essere risolte. Si è dimostrato che questo è dovuto al fatto che le forze efficaci a tre corpi sono state trascurate. Queste forze, che compaiono ogniqualvolta un hamiltoniano è adattato ad uno spazio di valenza, sono quasi sempre ignorate perché si ritiene producano effetti molto piccoli. In questa tesi si dimostra invece che questa approssimazione può portare a importanti variazioni nei risultati finali dei calcoli.
Sono stati osservati isomeri anche negli isotopi ^{217}Bi, ^{213}Pb, ^{211,213}Tl e ^{208,210}Hg. Attribuire spin e parità ai livelli nel ^{217}Bi e nel ^{208}Hg si è rivelato semplice, mentre negli altri nuclei è stato più difficile.
In conclusione, la tesi riporta risultati su diversi nuovi isomeri nei nuclei ricchi di neutroni vicino al piombo. Si sono anche messe in luce le difficoltà tecniche legate all'esperimento e gli accorgimenti adottati per risolverle. I casi fisici trovati appaiono molto interessanti, poiché mettono in evidenza aspetti prima ignorati della struttura nucleare. Le future indagini che saranno possibili con gli acceleratori e gli apparati oggi in costruzione forniranno molte più informazioni su queste tematiche.

Universa Universis Patavina Libertas.[a]

Motto of the University of Padova

[a]The freedom of Padua is full and for all.

1 Introduction

A century ago Sir Ernest Rutherford discovered the presence of a very small, positive-charged nucleus at the centre of atoms [1]. In the elapsed one hundred years atomic nuclei have been subject to many experimental studies aimed at investigating their structure and at understanding the reaction mechanism among them. A similar effort has been put in place to build theoretical models to explain the nuclear realm. Until recent years, the investigation was limited to stable nuclei, or nuclei close to stability, since only stable targets and beams were available. Using a metaphor, the effort of describing the nuclear structure looking exclusively at stable nuclei was like trying to rebuild a puzzle knowing only a small part of the picture. The availability of exotic or radioactive beams have enabled to study nuclei far from the valley of stability, creating new challenges for theoretical models and shedding a light on a much larger region of the Segrè Chart.
The interest in investigating atomic nucleus stems from a lot of different issues. At the first place, the nucleus is one of the building blocks of nature and understanding how protons and neutrons are bound together, what is the exact form of their interaction, and how nuclei change their structure as a function of isospin is a main subject for fundamental physics. In this regard, one of the key questions is, for example, if the usual magic numbers in stable nuclei disappear in very neutron-rich isotopes as a result of the increased diffusiveness of the neutron wave function [2, 3]. At the second place, since the nucleus is a many-body quantum system, it has also proven itself to be an effective

quantum-physics laboratory, with a rich phenomenology. Among the most recent developments we recall the study of three-body interactions [4, 5, 6, 7], of the effects due to the coupling of a bound system to the continuum [8, 9], and the discovery of aligned condensates [10]. Finally, but not less important, the information on nuclear structure is crucial for other fields of physics. The understanding of stellar nucleosynthesis and of the astrophysical phenomena such as the Supernovae or the X-ray Bursts depends on the knowledge which can be achieved on very exotic nuclei, i.e. on nuclei with a large excess of protons or neutrons with respect to the stable ones. Another example is provided by the determination of neutrino mass from the $\beta\beta$ decay, that relies on precise theoretical calculations of nuclear matrix elements.
The work presented in this thesis, based on an experiment performed at the GSI laboratory in Darmstadt (Germany) with the use of a radioactive beam to study neutron-rich lead isotopes, perfectly fits in some of the just-mentioned subjects. The next sections will outline the physical motivations for the experiment and its relevance in the field of modern nuclear physics.

1.1 The atomic nucleus

The atomic nucleus is a many-body system of strongly-interacting fermions of two kinds: protons and neutrons. The many-body problem is common to various sectors of physics, and different methods have been developed to deal with it. In fact, it is well known that the equations of motion for more than two bodies do not have an analytical solution. For the microscopic world the use of quantum field theory and perturbation methods has proved successful in providing an effective description of many phenomena. Being a many-body system, the atomic nucleus should give origin to the same problems encountered in condensed-matter physics. This is, at least to a certain extent, true and in fact there has been a proficuous exchange of mathematical methods and theoretical models between the two fields. Nevertheless, there are fundamental differences which make the nucleus a much more difficult system to study. On the one hand, the nucleus is composed by two different fermions, which have also an internal structure. The interaction between nucleons is thus much more complicated than the electromagnetic force, and many-body forces do play an important role in nucleon-nucleon interactions. Anyway, modern nuclear interactions fit the nucleon-nucleon scattering data very well, with $\chi^2 \approx 1$, meaning that at least the two-body part is well under control. On the other hand, the energy gap between collective motion and single-particle excitations is small and the overlap between different energy scales makes things more difficult to disentangle. Nonetheless, a secular behaviour of the nucleus emerges and one of its main features is the appearance of a shell structure, similarly to the atomic electrons. Differently from them, the nucleons are not subject to a central field, since the nucleon-nucleon interaction is dominated by short-range components. However, the first experimental observations revealed a shell structure similar to the electrons in an atom, and it turned out that the structure

of nuclei could be described by a shell model with a central mean field and a residual interaction between nucleons.
Nowdays, the shell model offers a very comprehensive view of the nuclear structure [11, 12], but it still presents important shortcomings. One problem emerges with the calculations for light nuclei. In this case the dimensions of the hamiltonian matrix are small enough to allow a diagonalization in the full space. These calculations should thus in principle be correct, on the contrary they fall short in reproducing the experimental data [4, 5, 7]. This has been attributed to the lack of three-body forces in the nuclear hamiltonian: their introduction improves the agreement with spectroscopic data. A second, perhaps more subtle (but not less serious) problem, is evident when performing calculations in heavier nuclei using a closed core, a valence space and a renormalized interaction. If a standard renormalised interaction is used, the shell model is not able to reproduce many spectroscopic features. A paradigmatic example of a remarkable failure is the well-known doubly-magic nucleus ^{48}Ca, whose neutron shell closure (N = 28) cannot be predicted via shell-model calculations using a first-principle renormalized interaction. In order to reproduce that magic number it is necessary to fit the matrix elements of the interaction on the experimental data. It has been argued that almost all the problems related to the interactions come from the monopole part of the nuclear hamiltonian, i.e. from its central part [12]. On the contrary the multipole part is correct, and in fact it has been demonstrated to be very similar among different interactions [12]. The adjustments needed for the monopole part have been proved compatible with a three-body force origin [6, 13], thus paving the way for the creation of a universal nuclear hamiltonian. However, despite the mentioned important progresses, a comprehensive picture of the nuclear phenomenology is still lacking. In particular, the evolution of the nuclear structure as a function of isospin is one of the major experimental and theoretical challenges of modern nuclear physics. The present work aims at giving an experimental contribution in this regard, by presenting new spectroscopic information in a previously only minimally explored region of the chart of nuclides. The theoretical interpretation of the results will point out some problems of shell-model calculations which are related to the appearance of effective three-body forces when dealing with renormalized interactions.
In this section, the basics notions of nuclear shell structure are recalled, while a more detailed discussion, focussed on the case of interest, can be found in chapter 5.

1.1.1 Nuclear hamiltonian and the two-body interaction

The nuclear hamiltonian, being the atomic nucleus a many-body quantum system, can be written as:

$$H = \sum_{i=1}^{A} T_i + \sum_{i,j}^{A} V_{ij} \tag{1.1}$$

where A is the number of nucleons, T_i is the kinetic energy of every single nucleon, and V_{ij} is the two-body interaction potential (here possible contributions from a three body interaction are neglected). One can assume the existence of a single-particle potential V_i which absorbs most of the V_{ij} potential:

$$H = \sum_{i=1}^{A} T_i + \sum_{i=1}^{A} V_i + \sum_{i,j}^{A} V_{ij} - \sum_{i=1}^{A} V_i = \sum_{i=1}^{A} H_i^{s.p.} + \sum_{i,j}^{A} H_{i,j}^{residual} \tag{1.2}$$

where $H_i^{s.p.} = \sum_{i=1}^{A} T_i + \sum_{i=1}^{A} V_i$ is the single-particle Hamiltonian, while $H_{i,j}^{residual} = \sum_{i,j}^{A} V_{ij} - \sum_{i=1}^{A} V_i$ is the residual interaction, i.e. the fraction of the two-body interaction which is not absorbed by the single-particle potential V_i. The physical meaning of the V_i potential emerges in its determination: being the nuclear force a short range one, the potential shape can be deduced from the density distribution of nuclei. Moreover, the experimental evidences of the conservation of angular momentum, parity and energy restricts the choice of the potential shape. Finally, shell effects similar to the atomic case are observed in the nuclear excitation energies as well as in the separation energies of nucleons: the eigenstates of $H^{s.p.}$ should reproduce these phenomena. Usually two potentials are employed: the harmonic oscillator, which allows one to perform analytical calculations, and the more realistic Wood-Saxon potential.

Harmonic oscillator mean field As a first approximation, the mean-field potential can be represented by a 3D harmonic oscillator potential V_c, which is a central potential and it also allows analytical solution for the Schrödinger equation. The resulting Hamiltonians for the i^{th} nucleon is:

$$H_i^{s.p.} = \frac{1}{2} M_i v_i^2 + \frac{1}{2} M_i \omega^2 r_i^2 \tag{1.3}$$

where M_i is the nucleon mass, v_i its velocity, r_i its radial distance from the centre of the nucleus, ω a parameter which can be deduced from the dimensions of the nucleus. The eigenfunctions are calculated as:

$$\Psi_{n,\ell,m_\ell,s,m_s}(r,\theta,\varphi) = R_{n,\ell}(r) Y_\ell^{m_\ell}(\theta,\varphi) \chi_{1/2}^{m_s} \tag{1.4}$$

where ℓ is the quantum number associated to the orbital angular momentum, s is the spin quantum number ($s = 1/2$ for both protons and neutrons), m_ℓ and m_s their projection on the polar axis, and n an integer quantum number: n = 0, 1, 2,... . The polar coordinates used to define the position in the space are r, θ and φ. $Y_\ell^{m_\ell}(\theta,\varphi)$ are the usual spherical harmonics, and $\chi_{1/2}^{m_s}$ the spin wave functions. The radial part of eigenfunctions is represented by $R_{n,\ell}(r)$:

$$R_{n,\ell}(r) = \left[\frac{2^{\ell-n+2}(2\ell+2n+1)!!\alpha^{(2\ell+3)})}{\sqrt{\pi} n! \{(2\ell+1)!!\}^2} \right]^{\frac{1}{2}} e^{-\frac{1}{2}\alpha^2 r^2} r^\ell \sum_{k=0}^{n} \frac{(-1)^k 2^k n! (2\ell+1)!! (\alpha^2 r^2)^k}{k!(n-k)!(2\ell+2k+1)!!}$$

where $\alpha^2 = \frac{M\omega}{\hbar}$ and (2n+1)!!≡(2n+1)(2n-1)(2n-3)...1. The eigenvalues of this Hamiltonian are (similarly to the well-known 1D harmonic oscillator):

$$E_{n,l} = \left(2n + \ell + \frac{3}{2}\right)\hbar\omega = \left(N + \frac{3}{2}\right)\hbar\omega \qquad N = 2n + \ell \tag{1.5}$$

Since $E_{n,\ell}$ is not a function of m_ℓ, s, m_s, the energy level degeneration is $2(2\ell+1)$ for both protons and neutrons. The numbers of nucleons at which shell-closure effects become

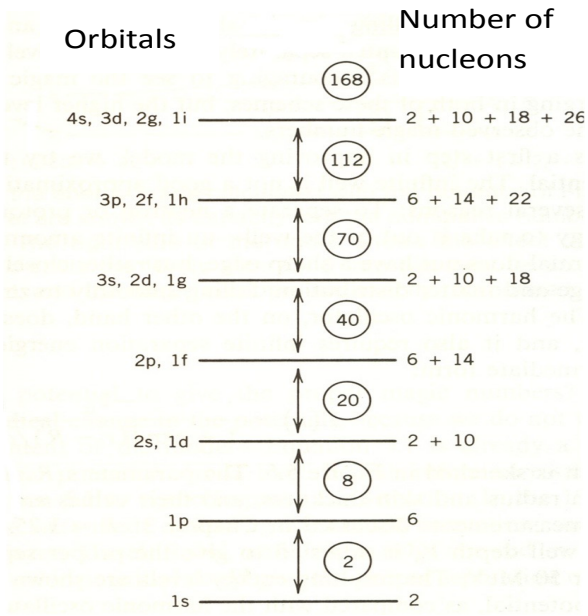

Figure 1.1: Single-particle levels for a tridimensional harmonic oscillator. The encircled numbers represent the magic numbers or shell closures.

evident are called magic numbers. The harmonic oscillator potential justifies only some of the observed magic numbers (2, 8, 20). The other magic numbers (28, 50, 82, 126) are not predicted by this model. Various modifications of the potential were attempted, but the most effective one was the insertion of the spin-orbit coupling. In atomic physics, this term stems from a relativistic correction, whereas in nuclear physics it has been derived by analogy with the atomic case. The expression of the spin-orbit interaction is:

$$V_{so} = V_{\ell s} \cdot \frac{\partial V_c}{\partial r} \cdot \vec{\ell} \cdot \vec{s} \tag{1.6}$$

where $V_{\ell s}$ is a phenomenological constant. This interaction splits levels with the same $\vec{\ell}$ but with different total angular momentum $\vec{j} = \vec{\ell} + \vec{s} \Rightarrow j = \ell \pm 1/2$. As a consequence, the separation between the two split levels is proportional to $(2\ell + 1)$, and m_ℓ and m_s are no longer good quantum numbers. Figure 1.2 shows that, introducing this potential, also the magic numbers 28, 50, 82, 126 are correctly reproduced.

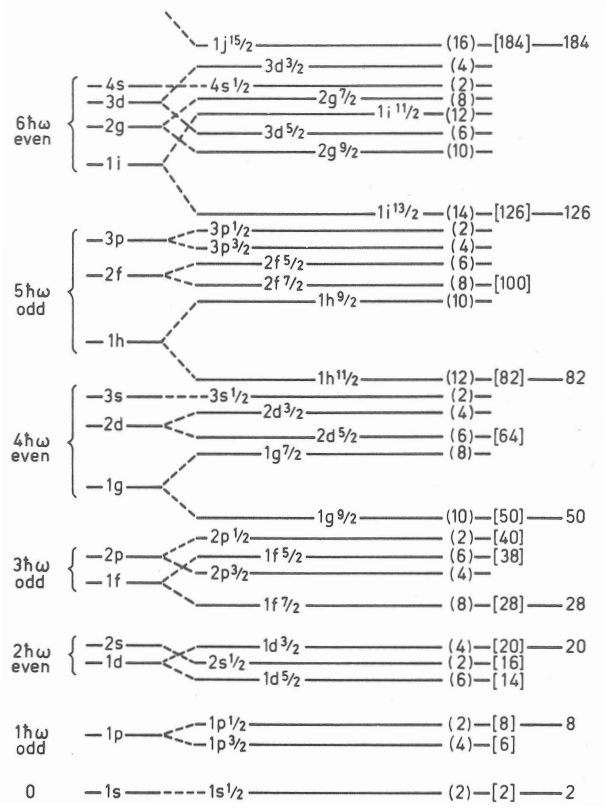

Figure 1.2: Single-particle levels when the spin-orbit term is added to the harmonic oscillator hamiltonian. Figure taken from Ref. [11, 14].

1.2 Electromagnetic decay

Gamma spectroscopy is a fundamental tool in nuclear physics, as it provides essential information on the structure of nuclei. In fact, the study of γ emission and of its competing process, internal conversion, allows one, for instance, to assign spin and parity to the nuclear levels or to probe the nuclear wave function through the measurement of the electromagnetic transition strengths. This is relevant for the experiment described in the present thesis, since the structure of the nuclei of interest is investigated through γ-ray spectroscopy of the isomeric decays.

1.2.1 Electromagnetic transition rates

One of the most common de-excitation modes of the atomic nucleus is via the emission of γ rays. The electromagnetic radiation produced by a nucleus can be described in terms of a multipole expansion. This is convenient because transitions between nuclear levels, which have a well defined spin and parity, carry away a precise amount of angular

momentum thus giving origin to selection rules that limit the number of possible multipolarities [15, 16, 17]. Moreover, as it will be shown soon, the highest multipolarities are much hindered with respect to the lower ones: therefore, in a γ decay, only one or two multipolarities are usually considered.
The total transition probability from an excited level i to a level f is determined as [15, 18]:

$$\lambda_{fi} = \frac{8\pi(L+1)}{\epsilon_0 \hbar L((2L+1)!!)^2}\left(\frac{E_\gamma}{\hbar c}\right)^{2L+1} B(\sigma L; I_i \to I_f) \tag{1.7}$$

where L is the angular momentum carried by the photon, E_γ its energy, I_f and I_i the spin of the final and initial states, σ represents the character of the transition, and $B(\sigma L; I_i \to I_f)$ a quantity called reduced transition probability. For electric transitions it is defined as [15]:

$$B(EL; I_i \to I_f) = \frac{1}{2I_i+1}|\langle f||\hat{Q}||i\rangle|^2 \tag{1.8}$$

while for a magnetic transition is:

$$B(ML; I_i \to I_f) = \frac{1}{2I_i+1}|\langle f||\hat{M}||i\rangle|^2 \tag{1.9}$$

where $\hat{Q}$ and $\hat{M}$ are the electric and magnetic operator, respectively. The relation between transition probabilities and reduced matrix elements is summarised in Table 1.1.

$T(E1) = 1.59 \cdot 10^{15}$ B(E1)E^3	$T(M1) = 1.76 \cdot 10^{13}$ B(M1)E^3
$T(E2) = 1.22 \cdot 10^{9}$ B(E2)E^5	$T(M2) = 1.35 \cdot 10^{7}$ B(M1)E^5
$T(E3) = 5.76 \cdot 10^{2}$ B(E3)E^7	$T(M3) = 6.28 \cdot 10^{0}$ B(M1)E^7
$T(E4) = 1.69 \cdot 10^{-4}$ B(E4)E^9	$T(M4) = 1.87 \cdot 10^{-6}$ B(M1)E^9

Table 1.1: Electromagnetic transition rates. The transition probabilities T are in s^{-1}, the energies E in MeV, B(EL) in e^{2}fm^{2L} and B(ML) in μ_N^2fm^{2L-2}.

Weisskopf Estimates If the transition is assumed to be due to a single nucleon moving from a spherical shell-model state to another one, then the calculation of the transition probabilities can be done analytically, yielding to the results shown in Table 1.2. These numbers are often used as a reference point when evaluating the hindrance or enhancement of a transition.

1.2.2 Internal conversion

The decay of the isomers we will deal with proceed through E2 γ-ray transitions of low energy where another electromagnetic process is important: the internal conversion. The internal conversion competes with γ decay and it occurs when the energy of the transition

$\mathrm{T(E1)} = 1.0 \cdot 10^{14}\ \mathrm{A}^{2/3}\ \mathrm{E}^3$	$\mathrm{T(M1)} = 5.6 \cdot 10^{13}\ \mathrm{E}^3$
$\mathrm{T(E2)} = 7.3 \cdot 10^{7}\ \mathrm{A}^{4/3}\ \mathrm{E}^5$	$\mathrm{T(M2)} = 3.5 \cdot 10^{7}\ \mathrm{A}^{2/3}\ \mathrm{E}^5$
$\mathrm{T(E3)} = 3.4 \cdot 10^{1}\ \mathrm{A}^{2}\ \mathrm{E}^7$	$\mathrm{T(M3)} = 1.6 \cdot 10^{1}\ \mathrm{A}^{4/3}\ \mathrm{E}^7$
$\mathrm{T(E4)} = 1.1 \cdot 10^{-5}\ \mathrm{A}^{8/3}\ \mathrm{E}^9$	$\mathrm{T(M4)} = 4.5 \cdot 10^{-6}\ \mathrm{A}^{2}\ \mathrm{E}^9$

Table 1.2: Single-particle Weisskopf estimates for electromagnetic transition rates. The transition probabilities T are in s^{-1}, the energies E in MeV, B(EL) in $\mathrm{e}^2\mathrm{fm}^{2L}$ and B(ML) in $\mu_N^2\mathrm{fm}^{2L-2}$.

is converted into the emission of an electron stripped from the inner atomic shells [18]. It is important to remember that this is not a two-step process, in which the emitted photon transfers it energy to the electron: this process has a too small probability to occur. The transition energy ΔE will thus appear as the kinetic energy T_e of the emitted electron, minus the binding energy of the electron itself:

$$T_e = \Delta E - B$$

The rearrangement of electronic shells following electron conversion leads to the emission of the X rays (or Auger electrons) characteristic of the shell occupied by the electron before expulsion. The internal conversion coefficient is defined as:

$$\alpha = \frac{\lambda_e}{\lambda_\gamma} \tag{1.10}$$

where λ_e and λ_γ are the decay probabilities for electron conversion and γ decay, respectively. The total internal conversion coefficient α_T is then the sum of the internal conversion coefficients for each atomic shell:

$$\alpha_T = \alpha_K + \alpha_L + \alpha_M + ...$$

Consequently, the total decay probability of the nucleus becomes:

$$\lambda_T = \lambda_\gamma(1 + \alpha_T) \tag{1.11}$$

The internal conversion coefficients for electric and magnetic multipoles in a non-relativistic calculation are [18]:

$$\alpha(EL) \cong \frac{Z^3}{n^3}\left(\frac{L}{L+1}\right)\left(\frac{e^2}{4\pi\epsilon_0\hbar c}\right)^4\left(\frac{2m_ec^2}{E}\right)^{L+5/2} \tag{1.12}$$

$$\alpha(ML) \cong \frac{Z^3}{n^3}\left(\frac{e^2}{4\pi\epsilon_0\hbar c}\right)^4\left(\frac{2m_ec^2}{E}\right)^{L+3/2} \tag{1.13}$$

where Z is the atomic number of the atom, n the principal quantum number of the bound electron wave function. More realistic calculations are provided by dedicated codes [19, 20]. As a final remark, we point out that the electron must exist for the internal conversion to take place: therefore, a fully-stripped ion cannot decay in this way.

1.3 Seniority scheme

It is useful to introduce at this stage the seniority concept since it will be exploited many times in the present work. In fact, the isomers studied in this thesis are strictly connected to it, being hence called seniority isomers. Seniority is defined as the number ν of unpaired nucleons, i.e. nucleons that are not coupled to angular momentum zero [21, 22]. This quantity is a good quantum number, at least in the first approximation, for semi magic nuclei. In these isotopes the n neutron or protons outside the doubly-magic core will mainly have a j^n configuration, where j is the lowest energy orbital outside the core. In the case of neutron-rich lead isotopes, the neutrons outside the Z = 82 and N = 126 ^{208}Pb core, will predominantly occupy the $2g_{9/2}$ shell. In a j^n configuration the conservation of the seniority quantum number provides a useful simplification in the description of the nuclear structure, called seniority scheme. In fact, it predicts that the low-spin excited energy levels should have energies independent on the number of nucleons outside the core. It also provides an analytical estimate of the electromagnetic transition strengths between these states, for which a parabolic behaviour is expected [22]. An example is given by the chain of tin nuclei approaching the ^{132}Sn Z = 50, N = 82 doubly-magic nucleus, where the neutrons are filling the $h_{11/2}$ shell: the 2^+ energy levels are constant within 100 keV [23, 24, 25, 26]. The B(E2;$12^+ \rightarrow 10^+$) of the Pb isotopes filling the $i_{13/2}$ shell towards the ^{208}Pb core show a regular parabolic behaviour, as expected: see Fig. 1.3, taken from Ref. [23].

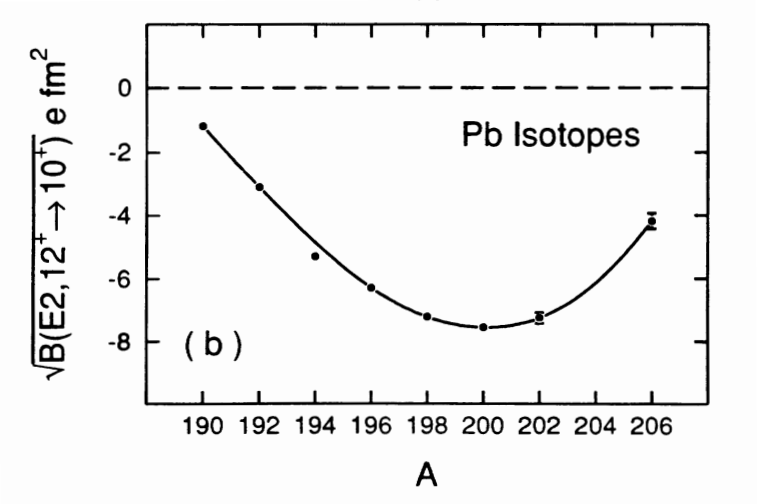

Figure 1.3: Regular parabolic behaviour of the Pb isotopes filling the $i_{13/2}$ shell towards the ^{208}Pb core. The E2 amplitudes from the 12^+ isomeric states are plotted against the mass number A: a solid line is added as a guidance for the eyes.Picture taken from Ref. [23].

The seniority scheme often gives rise to the so-called seniority isomers. In a j^n configuration the states at low energy are usually the ones with low seniority [27, 22], because breaking a pair of nucleons coupled to angular momentum zero has an energetic cost ("pairing energy"). As a result, the ground state of even-even semi-magic nuclei has $\nu = 0$, while the lowest levels (yrast) with J = 2,4,6,... almost always have $\nu = 2$ (only one broken pair of nucleons). Moreover, in a j^n configuration, due to the Pauli exclusion principle, not all angular momentum couplings of two identical nucleons are possible. The maximum angular momentum that can be created is given by [22]:

$$J^{max} = nj - \frac{n(n-1)}{2} \tag{1.14}$$

In the case of neutron-rich lead isotopes, above N = 126 , filling the $g_{9/2}$ shell, the maximum angular momentum is 8^+, while in the lead isotopes filling the $i_{13/2}$ shell towards the ^{208}Pb core shown in Fig. 1.3 the maximum momentum will be 12^+. These maximally-aligned states are usually, though not always, isomeric, i.e. their lifetimes are larger than 1 ns. This is due to a combination of a low transition rate to the underlying level and of a small transition energy. In fact, on the one hand the E2 strengths between levels with $\nu = 2$, as the low-spin yrast ones in semi-magic nuclei, are hindered, especially when the j shell is half-filled [28]. On the other hand, the energy differences between excited low-spin yrast levels become smaller going towards the maximally-aligned state [22]. Therefore, in the neutron-rich even-even lead isotopes the 8^+ yrast state is expected to be isomeric, with longer lifetime at midshell (^{212,214}Pb).

1.4 Physical motivation of the experiment

The motivation to study the neutron-rich nuclei beyond ^{208}Pb is twofold. The first reason is that this region is an effective testing ground for shell model, since it is just outside a double shell closure. As a consequence, neutron-rich lead nuclei can be interpreted, in first approximation, using only the valence space above the proton Z = 82 and neutron N = 126 cores, making a diagonalization of the hamiltonian possible in the full valence space. This allows one to perform a detailed test of the nuclear hamiltonian in this region. Moreover, isotopes with one proton particle (Bi) or one and two proton holes (Tl, Hg) with respect to lead can also shed a light on the proton-neutron interaction in this region.
The second reason is the study of the stellar nucleosynthesis of heavy elements, up to uranium. The synthesis of these isotopes is due to the rapid neutron-capture process (r process) thought to happen in supernovae [29]. The velocity and exact path depend crucially on the nuclear structure of the involved nuclei as well as on their β-decay lifetime. The r process involves very neutron rich nuclei in this region, and hence the study of how the β lifetimes evolve as a function of isospin provide important indications for the nucleosynthesis path.

1.4.1 Nuclear structure

As stated above, the interest in the structure of neutron-rich nuclei and surrounding isotopes originates from the fact that they involve few particles or few holes with respect to the doubly-magic nucleus ^{208}Pb, and are thus a good probe of the evolution of shell structure as well as of the theoretical models for this region of nuclides. The information becomes even more valuable if the scarce knowledge of this region is compared to the large number of studies available for lighter neutron-rich nuclei. For instance, it has been established that the shell closures N = 20 and N = 28 fade away in neutron-rich nuclei [30, 31]. Also for heavier isotopes there are hints that the N = 50 and N = 82 shell closures disappear when going away from the valley of stability, see Ref. [32] which provides a good summary of the present status. The wealth of information on these light- to medium-mass regions has also enabled to start to disentangle the effects of the different components of the nuclear force. For example, the importance of the monopole part of the tensor interaction has been pointed out [33, 34, 35], and the fundamental role played by three-body forces in shaping the neutron dripline in the oxygen region explained [7, 36, 37]. The aim of the study of neutron-rich lead isotopes and nearby nuclei is the measurement of level energies and transition strengths. The comparison of these experimental observables with theoretical models will provide an insight into the structure of these nuclei. The existence of significant disagreements between theory and experiment would imply the need to consider, for instance, three-body forces, core-breaking excitations or to correct the matrix elements of the hamiltonian. This is in particular true for the transition strengths from the isomeric states, which are very sensitive to the actual nuclear wave function.

In neutron-rich lead nuclei fairly schematic behaviour is expected on the basis of seniority scheme [21, 22]. In fact, the valence neutrons outside the N = 126 core predominantly occupy the $2\nu g_{9/2}$ shell, determining a wave function configuration mainly of the type $(\nu g_{9/2})^n$ where n is the number of valence neutrons: 2 for ^{210}Pb, 4 for ^{212}Pb and so on. This is predicted to give origin to the seniority isomer 8^+, obtained from the maximum possible alignment of two fermions in $g_{9/2}$, which is expected to have a lifetime in the μs range. In fact, the only two known nuclei, ^{210}Pb and ^{212}Pb have already been proved to have such isomeric state [38, 39] in the μs lifetime range, as a combination of a low transition energy (below 100 keV) from the 8^+ level to the 6^+ level and of a B(E2) from the isomer compatible with such lifetimes ($<$50 e^{2}fm^4). The detailed study of the isomeric B(E2) values will help to highlight important issues related to shell-model calculations. The presence of an isomeric state offers the opportunity to study the levels populated by the decay of the isomer. This makes such nuclei very suitable to be investigated with the decay spectroscopy technique, which was the main aim of the RISING stopped beam campaign at GSI.

1.4.2 Nucleosynthesis of heavy elements

The need to measure the β-decay half lives of neutron-rich nuclei in the region beyond ^{208}Pb originates from the necessity of having a reliable extrapolation of such nuclei lifetimes up to the r-process path. In fact, the nucleosynthesis of heavy elements is the result of a delicate balance between the neutron capture rate which tends to generate neutron-rich species and the β decay which shifts the atomic number Z by one unit upward. Figure 1.4, taken from Ref. [40], shows the predicted β-decay lifetimes for neutron-rich lead isotopes according to different models. The discrepancy among the predictions is very large, orders of magnitude; this is also due to the fact that high-energy first-forbidden (parity-violating) β decays give an important contribution in this region. Therefore, the data for $^{216-218}$Pb are much needed to compare the models with experimental values. Beta lifetimes will not be presented in this thesis, which concentrates mainly on the nuclear structure of neutron-rich Pb, Tl, Hg, Bi isotopes.

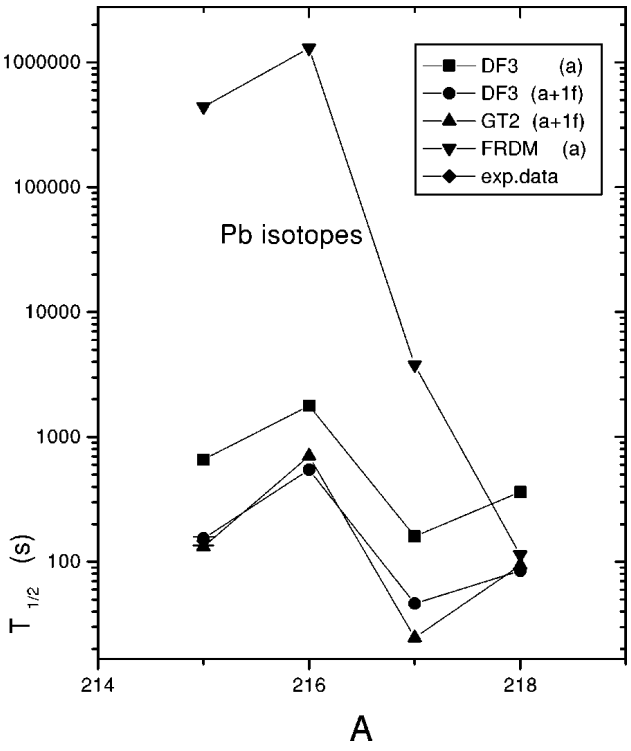

Figure 1.4: Theoretical predictions for the β-decay lifetimes of neutron-rich lead isotopes. Figure taken from Ref. [40].

1.5 Experimental method and challenges

The region of very neutron-rich nuclei beyond ^{208}Pb has been scarcely explored until now. In fact, while the neutron-rich region from tin (Z$\sim$50) down to nickel (Z$\sim$28) and calcium Z$\sim$20) have been studied via fusion-evaporation, deep-inelastic and fission reactions, and fragmentation of stable beams, the lead isotopes beyond N = 126 are much more difficult to populate. In fact, neutron-rich lead nuclei are impossible to reach with fusion-evaporation reactions. Multi-nucleon transfer reactions from ^{208}Pb targets were attempted, but managed to populate only up to ^{211}Pb, due to their tendency to equilibrate the N/Z ratio after the nucleon transfer. An alternative and effective approach is to populate these nuclei from the fragmentation of a uranium beam. It is then possible to perform decay spectroscopy of the isomeric states or β-decay studies. This method was successfully used to populate the seniority isomer in ^{212}Pb, see Ref. [39]. The idea, for the lead nuclei, is to take advantage of the predicted presence of 8^+ isomeric states and exploit them to observe the levels below, hence investigating the low-spin structure of these isotopes. The RISING stopped beam campaign at GSI has offered us a unique opportunity to perform this experiment.
However, with this technique there are two main difficulties to be overcome. The first one is the low production cross sections with respect to fusion-evaporation or deep-inelastic reactions. Table 1.3 shows some estimates of the cross sections with the codes COFRA [41] and EPAX2 [42], where the former appears more reliable for these exotic nuclei (see Fig. 2 in Ref. [39]). To overcome this problem, it is necessary to obtain a quite high uranium beam current to accumulate a reasonable statistics in the few days of beam time usually allocated for an experiment. The low yields anyhow do not allow to perform secondary reactions using the radioactive beam selected by the mass spectrometer. This limits to perform isomer- or β-decay spectroscopy, excluding at the moment the possibility of prompt γ-ray spectroscopy for isomers more exotic than ^{211}Pb.
A second important obstacle is represented by the large mass and atomic number of such heavy isotopes. They oblige to have a beam at an energy high enough ($\sim$1GeV$\cdot$A) so that the fragments are mostly fully stripped, to simplify mass reconstruction and have a good efficiency at the fragment separator. The most serious problem in fragmentation reactions in the lead region comes anyway from the fact that the uranium hydrogen- and helium-like charge states have an A/q ratio (q is the charge of the uranium ion) which is very similar to the one of fully-stripped $^{212-214}$Pb. Although the primary beam is fully stripped, the interaction with the target creates charge states which are transported through the fragment separator when the magnetic fields are set for the lead isotopes. This would lead to an unacceptable high counting rate on the detectors in the spectrometer. The solutions found to cope with the problem will be illustrated in detail in the next chapters describing the experimental setup.

	COFRA (mb)	EPAX2 (mb)
^{212}Pb	9×10^{-4}	7×10^{-3}
^{214}Pb	2×10^{-4}	2×10^{-3}
^{216}Pb	3×10^{-5}	5×10^{-4}
^{218}Pb	4×10^{-6}	1×10^{-4}
^{220}Pb	3×10^{-7}	1×10^{-5}

Table 1.3: COFRA and EPAX2 cross sections for Pb nuclei resulting from fragmentation of a ^{238}U beam on a Be target.

1.5.1 Relativistic fragmentation reactions

In this section a short description of the reaction mechanism employed to populate the nuclei of interest will be given. In general, fragmentation reactions populate broad areas of the table of nuclei. The fragmentation process can be understood in terms of two phases: abrasion and ablasion [43]. In the former step, abrasion, the collision of the beam (^{238}U) with the target (^{9}Be) takes place. Since the beam is relativistic (in the present case $\beta_{^{238}U} = 0.876$) [44], the interaction time between beam and target nucleons is about 10^{-23}s, considering a range of 1.2 fm for the strong nuclear interaction. This first part of the reaction is thus very fast and the average nucleon motion during it is only 0.1 fm. As a consequence, the nucleons can be regarded as static during the process, allowing one to describe it with Glauber-type models. In this approximation, only the nucleons in the geometrically overlapping region interact and are called the "participants", while the nucleons outside this region are called "spectators" and their motion is almost unperturbed [45]. The relative proportion of spectators and participants depends on the impact parameter, while the average excitation energy of the spectator nucleons, about 27 MeV [46], is mainly determined by the particle-hole excitations of the nucleons removed by the abrasion.
The second stage of the reaction is the evaporation of particles, or ablasion. In fact, the spectator nucleons may be excited to levels above the separation threshold, especially if the abrasion process has removed well bound nucleons from the interior core of the projectile. The ensuing deexcitation can be described by a statistical model assuming thermal pre-equilibrium in the excited pre-ablasion fragment. Therefore, the fragmentation reactions leading to the most neutron-rich nuclei are the ones involving mainly proton removal, with the resulting fragments cold enough that they will not evaporate too many neutrons: hence the name cold fragmentation. After the ablasion period (around 10^{-23}-10^{-16}s depending on the energies involved and on the binding of the reaction product), the excited fragment will cool down by γ emission, and a large number of high-spin levels will be populated. If in the decay chain of an excited state there is an isomeric state, the γ-decay process will stop for a while and the nucleus may survive during the flight path through a suitable spectrometer, necessary for its identification.

1.5.2 What is known around ^{208}Pb

As anticipated, ^{210}Pb and ^{211}Pb have been studied to quite high spins exploiting deep-inelastic reactions. The seniority-isomer 8^+ has been measured in ^{210}Pb [47] and the high-spin structure of this nucleus is known. Also ^{211}Pb was studied in detail [48], and its seniority isomer observed (see chapter 4 for more details).
The investigation of ^{212}Pb via fragmentation of a uranium beam, in Ref. [39], was limited by the low efficiency of the γ-detection setup, which was only 1% at 1 MeV. The spectrum obtained is shown in Fig. 1.5: even though it was not possible to establish the level scheme due to the low statistics, the observed isomer was tentatively identified as the 8^+, with a configuration $(\nu g_{9/2})^4$.

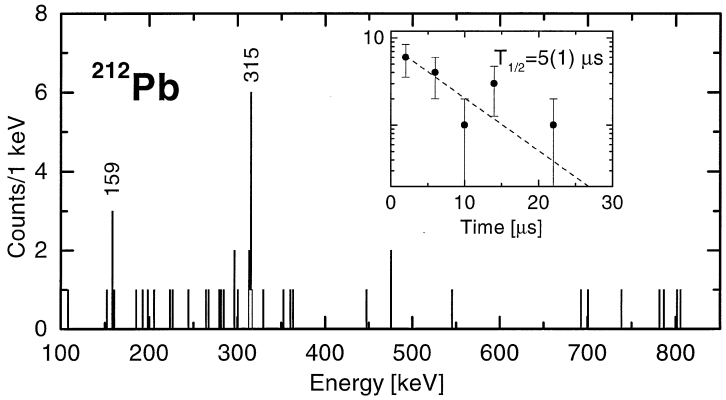

Figure 1.5: The ^{212}Pb spectrum obtained in the isomer decay studied in Ref. [39].

In this region also other isotopes have been studied. The bismuth isotopes are quite well known up to ^{215}Bi [49], from experiments with deep-inelastic reactions and proton-induced spallation of uranium. Their structure results from the coupling of the unpaired proton outside the Z = 82 core (mainly in $\pi h_{9/2}$) with the neutron levels of lead isotopes, and thus they have isomers originating from the configuration $\pi h_{9/2} \otimes \nu 8^+$.
Thallium and mercury isotopes beyond N = 126 have also been studied recently, again using the fragmentation of a uranium beam [50] and decay spectroscopy. The most neutron-rich nuclei in which isomers were found were $^{209}\mathrm{Tl}_{128}$ and $^{208}\mathrm{Hg}_{128}$. In both nuclei the isomeric states were interpreted as arising from the coupling of the one or two proton holes with respect to the ^{208}Pb core with the neutron particles in the even-even lead isotopes. These experimental findings also offer a guidance for what could be expect in more exotic thallium and mercury fragments.

1.5.3 The experiment

The main goal of the experiment was to populate neutron-rich nuclei in the lead region via the fragmentation of a primary uranium beam, and to study them via isomer or β-decay spectroscopy. The experimental setup is very similar to the one exploited in Ref. [50], but the spectrometer was set for the lead isomers. Since the mass spectrometer and the primary beam energy are the identical to those in Ref. [39], the same problems with charge states were expected. In the next chapters the two methods, studied before the experiment, to remove the charge states of the uranium beam from the acceptance of the spectrometer are described. The chosen one, a thick degrader along the beam line, has demonstrated to give an effective rejection of the primary beam charge states. Another important improvement is in the γ detection through the high-efficiency RISING array [51, 52], that has an efficiency ten times higher than the one available in the previous ^{212}Pb experiment. The experiment was performed at the laboratory of GSI (Helmholtzzentrum für Schwerionenforschung), see Fig. 1.6, close to Darmstadt, Germany and it lasted five days in September 2009. The average uranium beam current was around $1.5{\cdot}10^9$ particle per second (pps), or $\sim 1/4$ pnA.

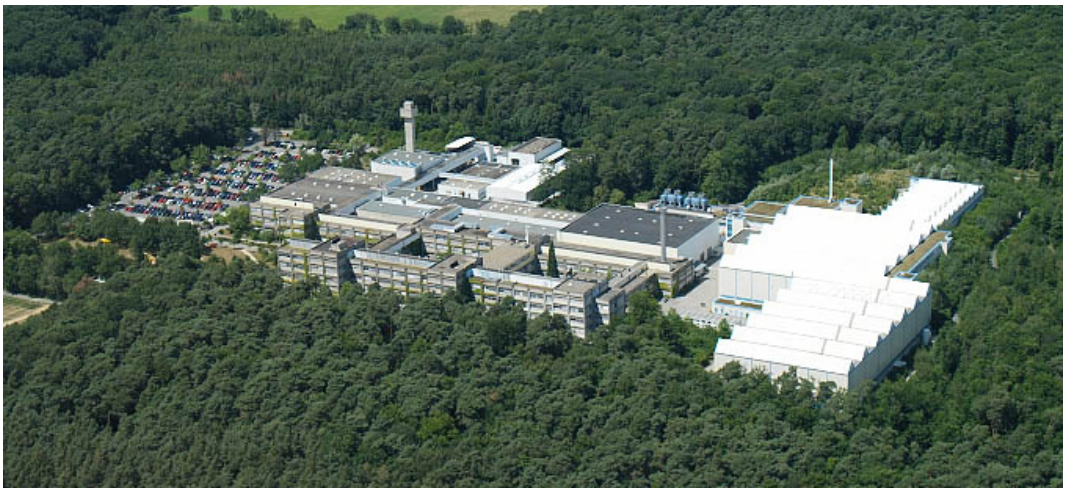

Figure 1.6: Aerial view of the GSI laboratory before the start of work for the FAIR facility. Picture taken from Ref. [53].

1.6 Outline of the thesis

After the short introduction given in the present chapter, the thesis is organized as follows:

- Chapter 2: A detailed description of the experimental setup, regarding both the mass spectrometer and the β and γ detection arrays.
- Chapter 3: The experimental challenges are described in detail with the employed solutions. The analysis procedure for isomer decay spectroscopy is also illustrated.
- Chapter 4: The results of isomer-decay spectroscopy are presented and discussed, in terms of expectations from systematics.
- Chapter 5: Modern shell-model calculations are presented and compared to all the experimental results. In particular, the issue of B(E2) values in lead isotopes is investigated in detail, leading to interesting considerations on the role of effective three-body forces.
- To conclude, a brief summary of all the results is given together with a short description of the future perspectives in this field with the new exotic beam facilities becoming available.

L'essentiel est invisible pour les yeux.

Le Petit Prince - Antoine de Saint-Exupéry

2 Experimental setup

In this chapter the main experimental setups used are described. In the first part, the accelerators employed to produce the uranium beam at 1 GeV·A are presented. Afterwards, the mass separator and its working principle are discussed. Finally, we provide a detailed description of the implantation detectors: the silicon active stopper and the RISING γ-ray array.

2.1 Primary beam

The primary beam requested to populate the exotic nuclei of interest was ^{238}U with an energy of 1 GeV·A, which is the maximum energy achievable at GSI. The energy was chosen to maximise the efficiency of the fragment separator, as well as to enable the atomic number identification, as it will be pointed out in the next sections. The beam structure consisted of a series of three-second periods: 2 s of beam (the "spill" period) and 1 second with beam off. The timing of the cycle was selected as a compromise between the necessity of having a high intensity and the technical limits of beam extraction from the accelerator. The intensity of the beam was roughly around $1.5 \cdot 10^9$ particles per second.

2.2 Acceleration complex

The GSI laboratory is the main European laboratory dedicated to nuclear physics and it is placed in the outskirts of Darmstadt. It can provide stable beams of different species up to uranium with energies up to 1 GeV·A. Therefore, a large number of scientific activities can be performed, ranging from nuclear to hadronic physics, see Fig. 2.1.

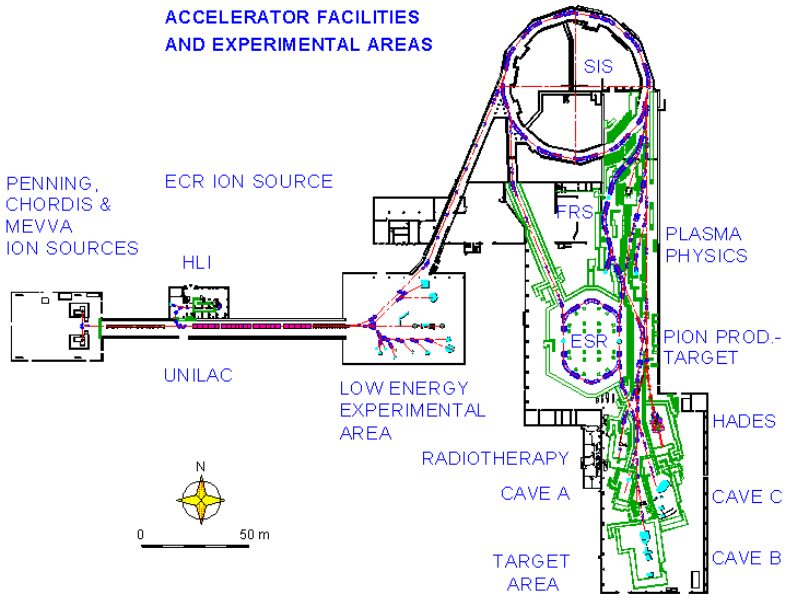

Figure 2.1: The map of the main GSI facilities. The accelerators UNILAC and SIS are pointed out, showing also the position of the FRS.

2.2.1 Ion sources and UNILAC accelerator

The ion source is of crucial importance to provide the desired high beam current. The production of an uranium beam is complicated due to radioprotection issues and by the chemical properties of the element. At GSI two ion sources are available: the PIG (PennInG) and MEVVA (Metal Vapour Vacuum Arc) sources. In the present experiment the MEVVA source was employed, being able to provide higher beam current. The ions are then accelerated through a 36 MHz RFQ (Radio Frequency Accelerator) pre-accelerator up to an energy of about 1.4 MeV·A, and then partially stripped by a jet of nitrogen gas. The second acceleration step occurs in the Alvarez linear accelerator UNILAC, capable of delivering a beam of around 11 MeV·A: see Fig. 2.2.

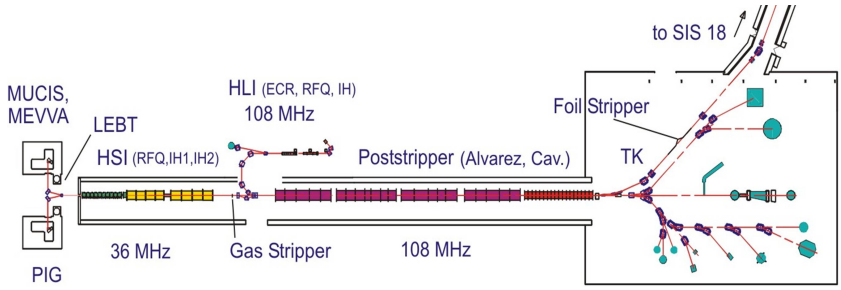

Figure 2.2: The ion sources (PIG, MEVVA), the RFQ pre-accelerator and the UNILAC accelerator at GSI before the low-energy experimental hall. Picture taken from Ref. [54].

2.2.2 The SIS-18 syncrotron

The pre-accelerated beam from the UNILAC is then injected in the SIS-18 synchrotron, shown in Fig. 2.3. This accelerator has a radius of 34.5 m and its 24 dipoles can provide a maximal bending power of 18 Tm. The accelerating potential is achieved through two radiofrequency cavities at 16 kV. The SIS-18 energy output for $^{238}U^{92+}$ ions was set to 1 GeV·A for this experiment.

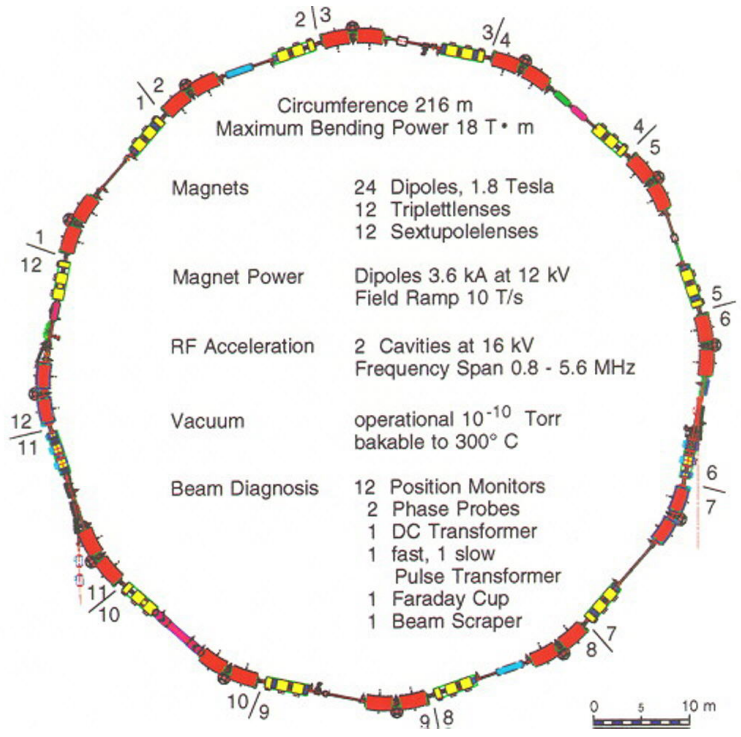

Figure 2.3: The SIS-18 synchrotron at GSI. Picture taken from Ref. [55].

2.3 The FRagment Separator (FRS)

After the SIS the beam is sent to the FRagment Separator (FRS). The FRagment Separator FRS is a double-stage magnetic mass spectrometer exploited to perform studies on exotic nuclei at the energies typical of GSI accelerators (several hundreds MeV·A) [56]. Figure 2.4 shows an axonometric view of the instrument, which is about 70 m long. The main elements are the four bending dipoles, which define four focal planes along the spectrometer. Figure 2.5 shows another scheme of the FRS, pointing out the detector positions for a full ion identification in the second and fourth focal planes. In the next paragraphs the characteristics and working principles of the spectrometer and its detectors will be illustrated, since they are the crucial elements for the experiment described in this thesis.

2.3.1 The target station

The beam from the accelerator complex is delivered on a production target. For the case of interest, the 1 GeV·A $^{238}U^{92+}$ beam impinged on a 2473 mg/cm^2 ^{9}Be target. Figure 2.6 shows a picture of the target ladder: various targets of different thicknesses are arranged on two of such ladders which are then controlled remotely, because of radiation protection issues.

The choice of the Be thickness is a very delicate one. On the one hand, a larger thickness would imply an increased reaction rate, while on the other hand the possibility of an interaction between the target atoms and the fragments of interest already produced would decrease the overall fragment yield. However, the selection of the thickness is not only determined by the necessary compromise among these two effects, since the target has also to be evaluated as an optically active part of the FRS, in particular regarding the energy of the exiting fragments [57]. This problem will be discussed in more detail later. The target had a 223 mg/cm^2 Nb stripper mounted directly after it. The stripper helps to keep the vast majority of the ions fully stripped after the primary target and this is important for the identification on the FRS. Moreover, the isomers which are the main aim of the present experiment are de-excited by low-energy transitions, which are fully converted, thus making effectively larger their lifetime. Therefore, they are hindered in a fully-stripped nucleus and they will not decay during the approximate 300 ns flight path through the FRS, enabling their effective detection at the final focal plane. In the case of short-lived isomers, this feature is essential for their measurement: the shortest half life measured with this setup is $t_{1/2} = 10.3(24)$ ns in ^{200}Pt [58].

2.3.2 Magnetic elements and slits of the FRS

The spectrometer is divided in four sections, each of them equipped with a dipole and a series of quadrupoles and hexapoles.

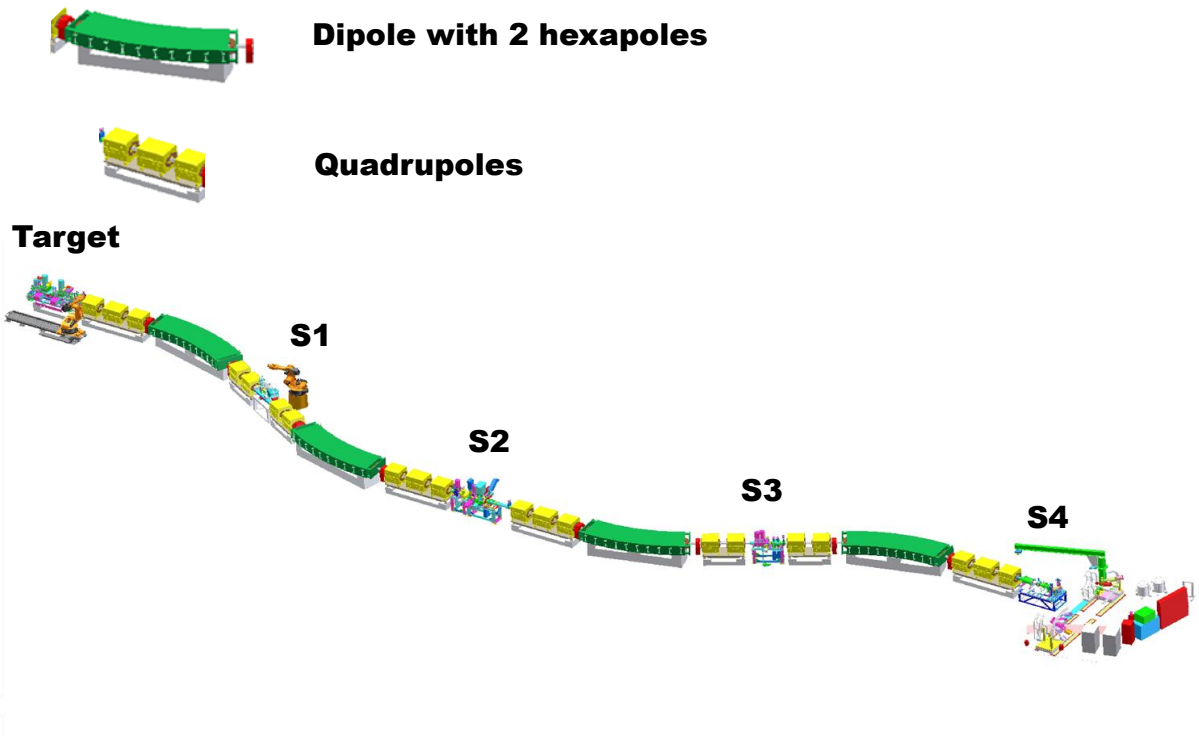

Figure 2.4: The Double-stage magnetic spectrometer FRagment Separator (FRS) at GSI. The green elements are the four dipoles, while the yellow ones are the quadrupoles used to focus the beam. Hexadecapoles are also present to correct the optic abberations of the spectrometer: they are indicated in red, before and after the dipoles. The four focal planes (S1, S2, S3, S4) are also pointed out.

Dipoles The dipoles bend the ions according to their magnetic rigidity. Their nominal radius is 11.5 m (deflection angle of 30°) and the maximum possible magnetic rigidity of the beam is 18.5 Tm. The particle dispersion is along the horizontal plane, and the aperture of the dipole in this direction is 200 mm. The motion of a particle inside the dipoles is determined by the Lorentz force:

$$B\rho = \beta\gamma\frac{A}{q} \tag{2.1}$$

where B is the magnetic field (up to 1.65 T in the FRS), ρ is the radius of the ion trajectory, β and γ are the usual relativistic kinematic parametrs, A is the mass number

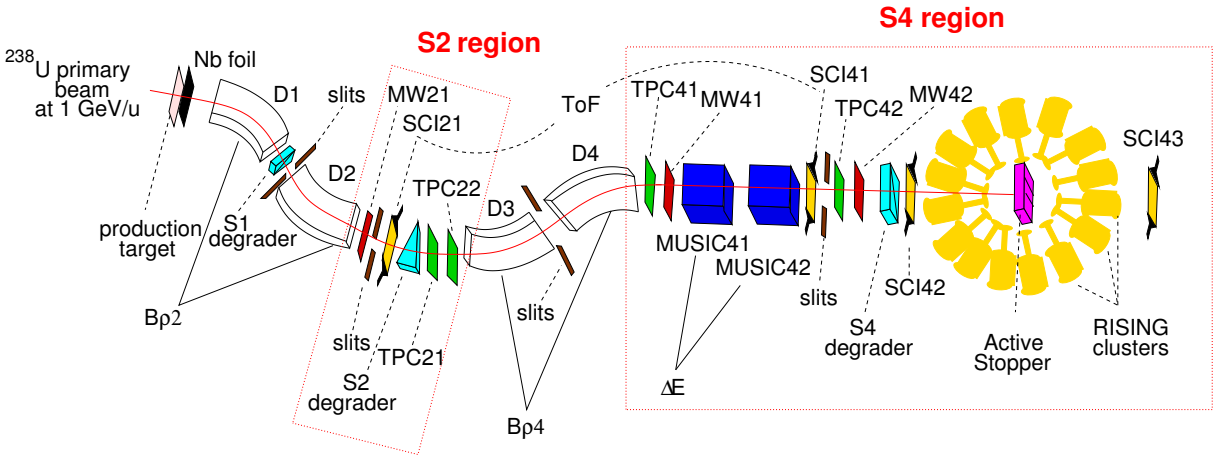

Figure 2.5: Schematic view of the FRagment Separator (FRS) setup showing the positions of the detectors along the beam line that provide an unambiguous identification of the ions event by event. Picture courtesy of A. Morales.

Figure 2.6: Picture of one of the two target ladders. Some of the holes are holding the Be targets of different thicknesses.

and q is the charge of the ion ($q = Z$ for fully stripped ions).

Quadrupoles Groups of quadrupoles are placed along the beam line before and after the bending dipoles. A magnetic quadrupole defocusses along one axis and focusses on the one perpendicular every charged particle in motion [59]. An appropriate combination of adjacent quadrupoles can have an overall focussing effect on both vertical (Y) and horizontal (X) directions. Actually, the role of the quadrupoles in the FRS is indeed to correct the dispersion of the beam due to interaction with matter in the beam line

before entering a dipole, and to counterbalance the variances of the bending field after the dipoles.

Hexapoles Before and after each dipole an hexapole magnetic element is placed in order to correct second order aberrations of the beam optics.

Slits Along the FRS beam line there are five sets of slits (see Fig. 2.7 and Fig. 2.5), made of thick copper blocks one after the target and one in each focal plane. The slits after the target are to cut in both the X and Y direction, like the slits of the first three focal planes. On the contrary, the slits of the last focal plane can only reduce the acceptance in the horizontal direction. The function of the slits is to cut the acceptance of the spectrometer in order to eliminate the ions with a certain magnetic rigidity, for example to prevent a too high counting rate on some detectors or to improve the selectiveness of the FRS. In the present experiment, the slits positioned after the target were symmetrically closed leaving a gap of 40 mm in the horizontal direction and of 36 mm in the vertical direction to cut the undesired fission products, which are less forward focussed with respect to the fragmentation products.

Figure 2.7: Photograph of one of the target slits to cut the acceptance in the vertical (Y) direction.

2.3.3 Detectors along the FRS

The requirement to identify the ions in mass and atomic number on an event-by-event basis leads to the necessity of having different detectors to measure the position of the

ion, its time of flight and its atomic number. A measurement of the primary uranium beam intensity is also provided.

MultiWire Proportional Counters MWPC The multiwire proportional counters are placed along the FRS beam line to measure the x and y positions of the ions [60]. Since they are used for both calibration and real measurement purposes, they can be inserted or extract remotely from the beam line.The working principle is the same of a usual multiwire chamber, and is illustrated in Fig. 2.8, where the pre-gap is used only for light ions ($Z > 6$), and hence not employed in the present experiment. The filling gas is a mixture of CO_2, Ar and alcohol. An incident particle ionises the atoms of the filling gas and the resulting electrons are accelerated by an electric field of around 2 kV towards the anode. The consequent avalanche leads to amplification of the signal by a factor 1000. As the electrons hit the anode, a positive signal is induced on the horizontal and vertical cathode wires. The difference in charge magnitude at the extremities of the cathode wires gives the desired position information. The spacial resolution is 0.5 mm in both directions. The MWPC are the reference position detectors in the FRS, and they are placed at each of the four focal planes. In the second and fourth focal planes two MWPC are placed, in order to provide also a measurement of the angle of the ion trajectory.

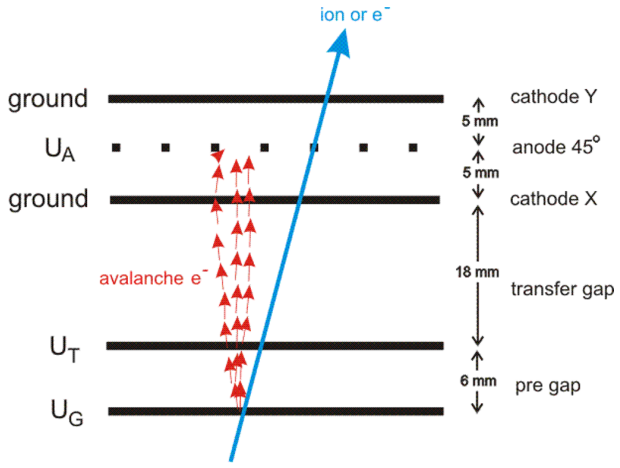

Figure 2.8: Schematic view of a multiwire proportional counter (MWPC) of the FRagment Separator. Picture taken from Ref. [61].

Time-Projection Chambers (TPC) A new, alternative way to measure the position along the beam line is offered by the time-projection chambers [62]. Figure 2.9 provides a schematic view of the device used at GSI. The volume of the detector is filled with a mixture of methane and argon. The chamber has a vertical drift direction. The drift

electric field is obtained by applying a high voltage to a cathode, while the sensitive (proportional) part of the detector is made of four anodes wires, placed into C-shaped cathodes. The y coordinate is obtained from the drift time, while the x coordinate is determined from the signals of two delay lines connected to the cathodes. Two TPCs are placed at both the second and fourth (last) focal planes, to measure both position and angle of the ion trajectory. The position resolution is about 0.1 mm in the x coordinate and 0.05 mm in the y coordinate. The detection efficiency for the heavy ions of interest is 95% at a 100 kHz counting rate. In the present experiment, the TPCs were used as position detectors, due to the high efficiency and excellent space resolution, whereas the MWPCs were only used during the initial calibration.

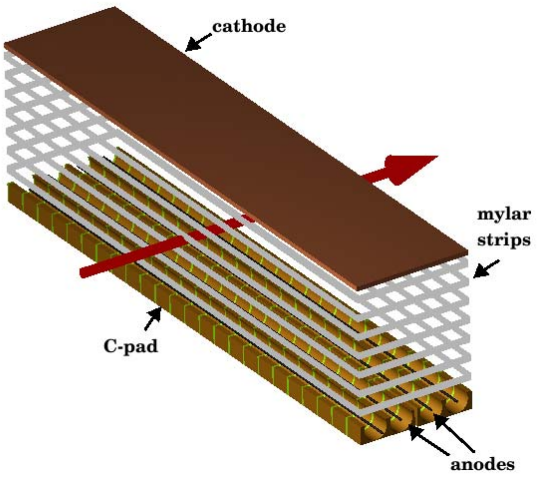

Figure 2.9: Schematic view of a time projection chamber (TPC) in the FRagment Separator.

Scintillators The time-of-flight is measured through scintillators placed in the focal planes S2 and S4 of the FRS. In the fourth focal plane (S4) there are two scintillators, serving different purposes, which will be explained in more detail later. The plastic scintillation material is BC420, which has a fast time response (the decay constant is 1.5 ns). The light output is detected by two photomultipliers (PMT) at each side of the scintillator, in the horizontal direction, called left and right PMT. There are thus two time readings, and their difference is proportional to the position where the ion passes through the detector. Moreover, the intensity of the registered signal is proportional to the energy released by the ion. Therefore, the scintillators can provide both time and position information, plus the energy loss measurement. The time resolution is 40 ps, while the space resolution is 4 mm, quite poor if compared to the TPCs, and consequently the space information is not used if not for calibrations.

Ionization chambers At the fourth focal plane the atomic number of the ions is measured by means of two multi-sample ionization chambers, called MUSICs [63], shown in Fig. 2.10. According to the Bethe-Block formula, the energy loss is proportional to Z^2, and thus from its measurement one can determine the atomic number. The filling gas is CF_4 at atmospheric pressure. Each detector is divided in eight sections, each with an anode to collect the charge resulting from the ionization of the gas. The applied voltage to the cathode is around -8 kV.

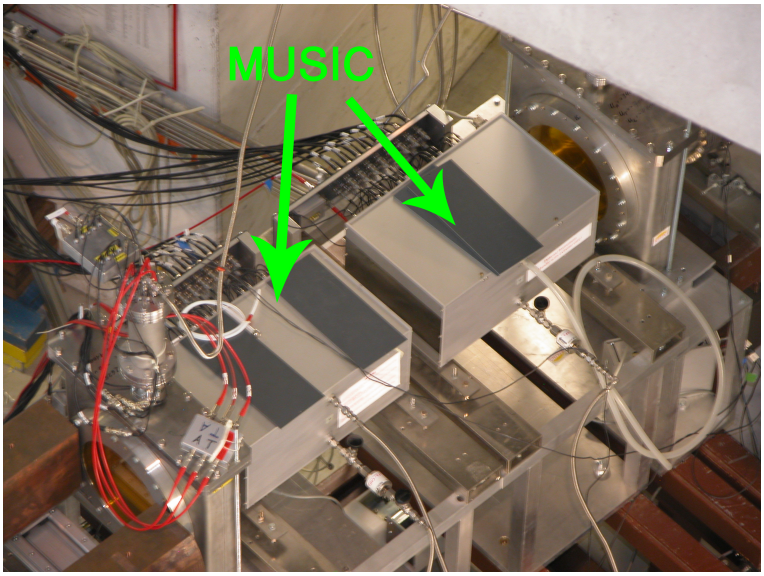

Figure 2.10: Photograph of the two MUSIC chambers at the fourth focal plane, taken from Ref. [64].

2.3.4 The FRS optics setup

The FRagment Separator is a double-stage double-achromatic magnetic spectrometer, conceived to separate relativistic ions produced by the SIS beams. It combines the usual concept of mass spectroscopy via a magnetic field with the use of shaped degraders to cut the acceptance also in the ion atomic number: this is the $B\rho - \Delta E - B\rho$ method for the separation of a selected fragment. In fact, due to the relativistic velocities of the reaction products ($\gamma \sim 1.9$), a separation by A and Z is not possible using only magnetic or electric sector fields. Nevertheless, a good separation can still be achieved combining the magnetic rigidity analysis with the atomic energy loss of the fragments in matter.
The principle of magnetic mass spectrometry is based on the effect of the Lorentz force on a charged particle in a magnetic field B: see Eq. 2.1 The variable $B\rho$ is called magnetic rigidity, and it determines the trajectory of the ions inside the spectrometer.

The characteristics of the bending dipoles are determined by the magnetic rigidities of the reaction products, ranging from 5 to 18 Tm. The first two dipoles (the first stage of the FRS) separates the ions according to their A/Z ratio (fully stripped ions), so that the fragments with the same magnetic rigidity are focussed at the same point at the second focal plane S2. The last two dipoles also separate in A/Z, but counterbalancing the momentum dispersion of the first stage: the FRS is thus overall achromatic, i.e. the position in the S4 plane does not depend on the initial fragment momentum, but only on its A/Z ratio. Figure 2.11 provides a scheme of the achromatic operation of a mass spectrometer like FRS. The two stages a and b represents the first and second two dipoles of the FRS, respectively. In order to achieve an effective separation of relativistic

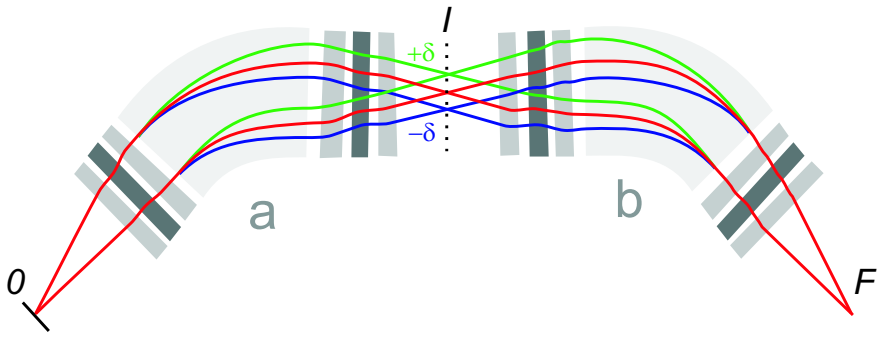

Figure 2.11: Schematic view showing the selection mechanism of fragments when the separator is operated in achromatic mode. O is the object, I the intermediate focal plane and F the final focal plane. The momentum dispersions in the two stages a and b compensate each other, and thus fragments with the same A/Z ratio are all focussed at the same position in the final focal plane. Picture taken from Ref. [65].

ions, a dispersion in magnetic rigidity is not sufficient. To further cut the phase-space of the fragment beam, a degrader is placed at the S2. The different atomic energy loss, proportional to Z^2 according to the Bethe-Block formula, leads to a change in the $B\rho$ of the fragments. The second stage of the FRS (third and fourth dipoles) subsequently separates the ions again according to their new $B\rho$, transporting them to the final focal plane. This second separation in magnetic rigidity is thus not only a separation in A/Z, but also in Z, as the final $B\rho$ also depends on the atomic number of the fragment. Figure 2.12 shows the different selections performed by the FRS stages on the fragment beam when a wedge-shaped degrader is used. The first stage selects mainly in A/Z (the initial momentum spread being quite small in a fragmentation reaction) and thus, in the proton-neutron space, it identifies the regions divided by the full lines. The second stage, after the degrader, also selects according to the proton number Z due to the degrader in the middle focal plane (S2), and its action is shown by the dotted lines. The overall effect

is a well-defined cut in the desired region of the proton-neutron space. In Fig. 2.13 a scheme of the FRS with the wedge is provided: it shows how, after the wedge (degrader), the selection in $B\rho$ is actually also a selection in Z.

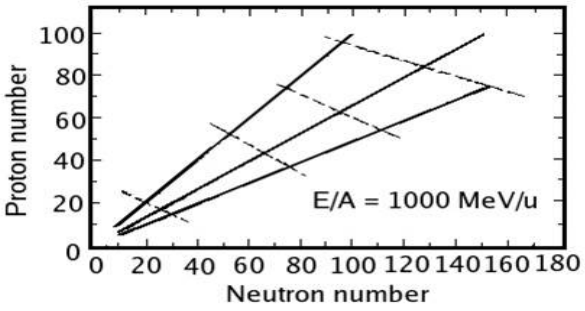

Figure 2.12: Figure showing the selection mechanism of fragments using the $B\rho - \Delta E - B\rho$ method; see text for details. Picture taken from Ref. [56].

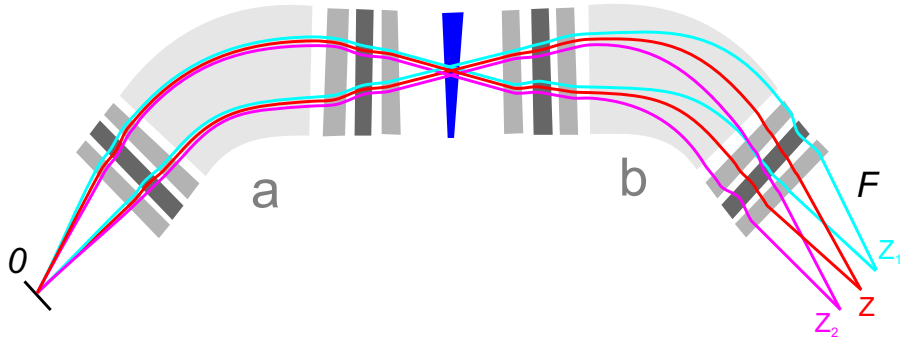

Figure 2.13: Schematic view showing the selection mechanism of fragments with the $B\rho - \Delta E - B\rho$ method. O is the object, I the intermediate focal plane and F the final focal plane. The wedge (profile-shaped) degrader in the intermediate focal plane enables to separate fragments with same A/Z ratio according to their atomic number Z. Picture taken from Ref. [65].

From the point of view of the magnetic optics, the most important quantity is the dispersion parameter of the spectrometer, which is defined as:

$$D = \frac{\Delta x}{\Delta B\rho / B\rho} \tag{2.2}$$

where Δx is the space difference in the dispersion coordinate (horizontal direction). Therefore, the dispersion D is measured in mm, and a typical value for the FRS is 6

mm, i.e. fragments differing 1% in $B\rho$ are spread 6 mm apart in the final focal plane. The dispersion parameter completely determines the optics in the first stage of the FRS: if $(B\rho_0)_2$ is the magnetic rigidity of the central trajectory (a value known from the magnets settings) then the $B\rho$ of a fragment at a position x_2 in the second focal plane is:

$$B\rho_2 = (B\rho_0)_2\left(1 + \frac{x_2}{D_2}\right) \tag{2.3}$$

Similarly, the position in the final focal plane is a measurement of the magnetic rigidity in the second stage of the FRS, once its dispersion D_4 and the magnification[1] M parameters are known:

$$B\rho_4 = (B\rho_0)_4\left(1 + \frac{x_4 - Mx_2}{D_4}\right) \tag{2.4}$$

The combination of the magnetic settings and of the shape of the degrader enables one to perform transformations in the phase space of the fragment beam, obtaining the desired final optical characteristics. Although many different combinations are possible, two main setups are usually adopted for FRS: achromatic and monochromatic.

The achromatic setting The achromatic setting is chosen to preserve the achromaticity of the spectrometer: fragments with the same A/Z ratio are focussed at the same point in the final focal plane, whatever their initial energy (or linear momentum p_0) after the target was. For a given A/Z ratio, $\Delta B\rho/B\rho = \Delta p/p_0$ and the dispersion on the focal plane induced by the momentum spread is:

$$\Delta x = D\Delta p/p_0$$

Combining Eq. 2.3 and 2.4 is then straightforward to see that the achromaticity condition without materials inside the FRS is given by $D_4 = -D_2M_4$. When the degrader at the middle focal plane (S2) is inserted, it is possible to preserve the achromaticity of the FRS by using a shaped degrader. With this kind of degraders, the energy loss of the fragments depends on the position at S2, which is in turn dependent on the ion energy after the target: $\Delta x_2 = D_2(\Delta p/p_0)$. If p_1 and p_2 are the momenta of two different fragments, the preservation of the achromaticity is achieved when the profile is set in order to satisfy the condition $\Delta p_1/p_1 = \Delta p_2/p_2$. The achromatic setting improves the A/Z separation, since fragments with the same A/Z are focussed in the same point at the final focal plane, and thus it is straightforward to identify different nuclei according to their position on the final focal plane (S4).

Monochromatic setting There are cases in which a monochromatic secondary beam is required in the FRS. This is the case, for example, of the experiment described in the

[1]The magnification is defined as the ratio between the dimensions of the image and of the object, similarly to optical lenses.

present thesis, where the aim is to implant the fragments in an active stopper at S4. In order to implant all the fragments of interest at the same depth in the stopper (at its centre, to increase detection efficiency) it is desirable that all the fragments of a certain isotope have the same energy, which can then be tuned to reach the needed implantation depth. To fulfill this purpose, the degrader has to be shaped in such a way that the energy loss of the ions compensates their initial momentum spread. This is possible because, for a given A/Z, the position at S2 is determined by the fragment velocity. Figure 2.14 presents the schematic degrader setup in the case of a monochromatic setting.

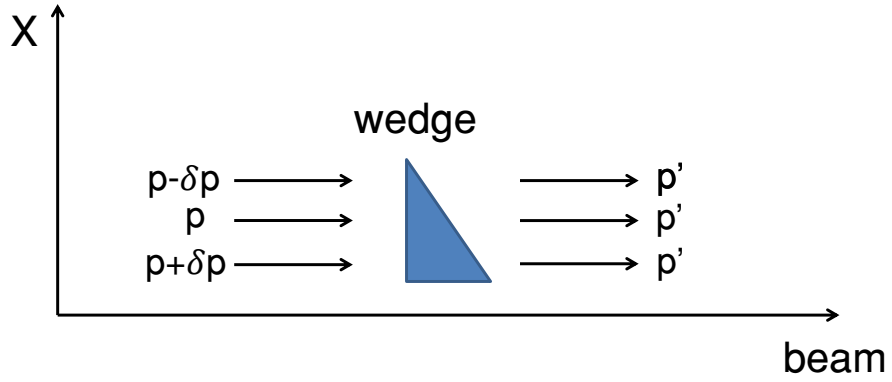

Figure 2.14: The wedge degrader in the intermediate focal plane S2 is shaped so that the initial momentum differences between the ions are compensated by the energy loss in the degrader.

2.4 The implantation setup

After the final focal plane of the FRS, the ions are slowed down by a degrader and they are implanted in the active stopper, an array of double-sided silicon detectors (DSSSDs). The stopper is at the centre of the RISING γ-ray array. Before and after the stopper, along the beam line, two scintillators are placed. The next section describes these detectors and their role.

2.4.1 The variable degrader and the scintillators

The initial energy of the reaction products in the present experiment is around 1 GeV·A and, after the energy loss in all the materials along the beam line in the FRS it is still several hundreds of MeV·A. In order to implant the ions in the final stopper it is necessary to reduce their energy to a few tens of MeV·A, and this is achieved with a variable degrader placed before the implantation detectors, see Fig. 2.15. The degrader

has an homogenous profile. Its thickness can be changed so that the residual energy of the fragments is tuned for the implantation at the centre of the silicon detector. The energy interval allowed is actually quite strict: once the thickness is tuned for a certain atomic number only several other species around the chosen one are stopped in the silicon detector. In fact, much heavier fragments are stopped in the degrader or in the following scintillators, whereas much lighter ions fly through the implantation detector.

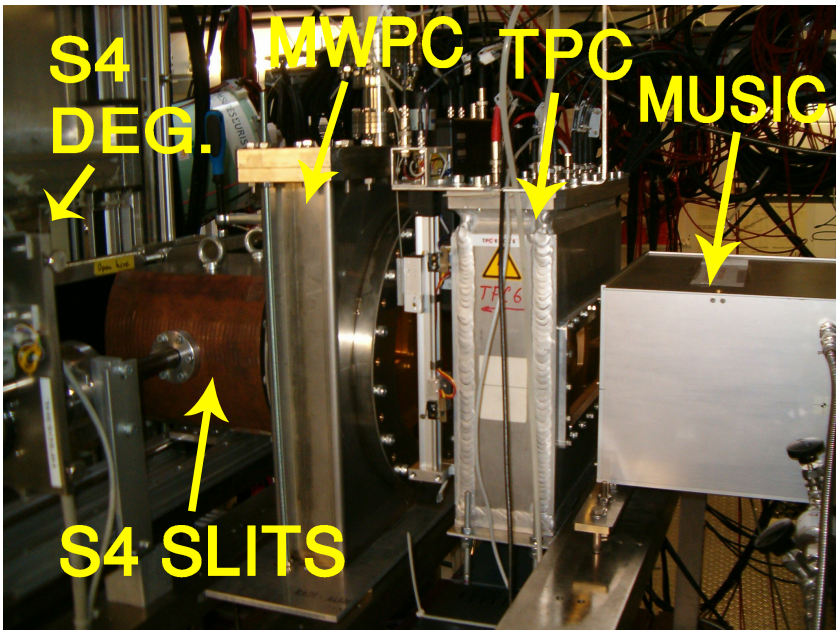

Figure 2.15: The S4 focal plane setup immediately before the RISING array, with the massive S4 slits, the position detectors TPC and MWPC and the S4 degrader. The SCI42 is not visible. Picture taken from Ref. [64].

In order to control the implantation of the ions, two scintillators are provided, one before and one after the silicon detector. The first scintillator (SCI42), see Fig. 2.5, is placed immediately after the degrader, before the DSSSD, and it provides the trigger for the implantation. The measured energy loss is also exploited to exclude from the analysis the ions which are the products of reactions in the degrader.
The second scintillator (SCI43), being positioned after the silicon detector, detects the ions not implanted and can thus be employed as a veto to the trigger signal provided by SCI42. However, since every implantation produces a cascade of high energy electrons which hit SCI43 similarly to an ion flying through, the effectiveness of the veto is limited and it is in fact employed only in the offline analysis.

2.4.2 The Double-Sided Silicon Strip Detectors (DSSSD)

The Double-Sided Silicon Strip Detectors (DSSSDs) are used as a position and energy-sensitive active stopper for decay spectroscopy [66, 67]. It is made of three layers each composed of three pads, see Fig. 2.16. Every pad is a DSSSD provided by Micron Semiconductor Ltd. It has a dimension of roughly 5 × 5 cm and a thickness of 1 mm. Each of the nine pads has 16 strips (3 mm wide) on both x and y coordinates. The thickness of the detector is sufficient for the implantation of heavy ions, while the detection of β particles is more delicate. Simulations with Geant4 have proven that it is essential to implant at the centre of the silicon detector to improve the detection efficiency [66]. As a consequence, a monochromatic setting of the FRS is often preferred. The aim of the pixellation of the silicon is to enable implantation-decay correlations. In fact, the DSSSD has to be able to detect an implantation event in a pixel, and its subsequent β decay (α or proton decays can also be detected) in the same pixel or in the adjacent pixels. The detector are not kept under vacuum but are inside a box with the entrance and exit windows made of black Pocalon C foil and of an Al foil. The detectors are biased with 200 V to achieve full depletion. Figure 2.17 shows the detector placed at the centre of the RISING array. The energy range of the detected particles in the

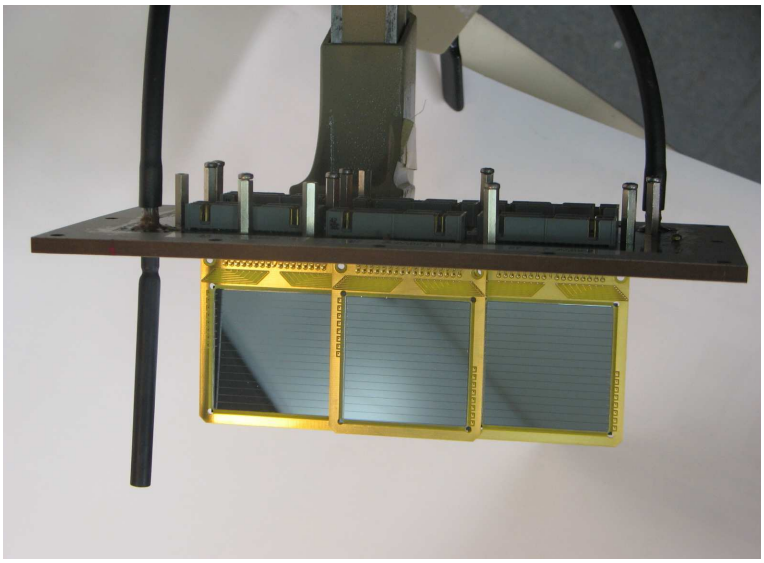

Figure 2.16: One of the three layers of the active stopper. The three DSSSD pads are visible.

silicon detector is very wide: from the β-decay electrons which deposit in the DSSSD as low as 100 keV, to the implantation of an heavy ion that releases an energy of more than 1 GeV. Therefore, the preamplifiers have to be able to handle this full range in order to discriminate both implantation and decay events. The Mesytec MPR-32 multi-channel preamplifiers are used for this purpose, being operated in logarithmic mode. This mode

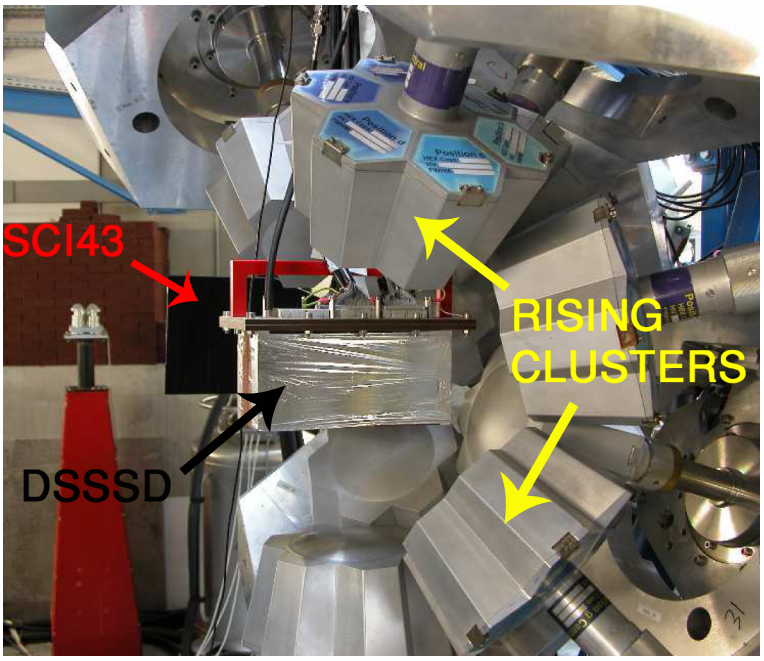

Figure 2.17: The DSSSD detector placed in its protecting box at the centre of the RISING array. SCI43 is partially visible behind the detector.

has a linear range up to 2.5 or 10 MeV and a logarithmic range from 10 MeV to 3 GeV. The minimum energy deposited by electrons is 100 keV if the implantation occurs at the centre of the silicon [66], and the threshold is consequently kept as low as permitted by background noise, usually around 150 keV, depending on the specific strip considered.

2.5 The RISING γ-ray array

The RISING γ-ray array [51, 52] surrounds the active stopper and measures the γ rays originating from the isomeric decays or from the de-excitation of the β-daughter nuclei. The array is composed of 105 high-purity germanium (HPGe) crystals belonging previously to the Euroball spectrometer [68]. The crystals are housed, in groups of seven into 15 clusters. The crystals are kept at a temperature of 77° K by liquid nitrogen to reduce the electronic noise from electrons being thermally excited to the semiconductor conduction band. The interaction between electromagnetic radiation and matter at the energies of interest ($\sim$ 10-3000 keV) is dominated by the photoelectric effect, the Compton scattering and pair-production. While the first two interactions are important in the energy domain of interest, only the photoelectric effect transfer to the semi-conductor all the energy of the photon, hence enabling its correct measurement. Figure 2.18 shows the position of the crystals inside the cluster. The clusters are geometrically arranged

around the central active stopper as in Fig. 2.19, as close as possible to increase the efficiency, which is around 15% at 662 keV.

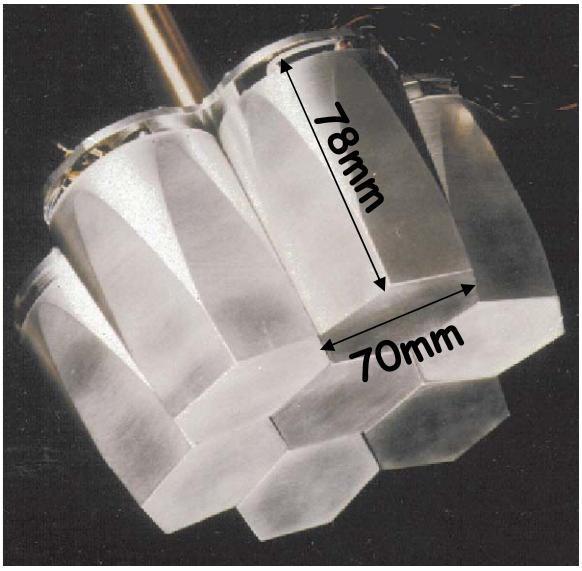

Figure 2.18: Photograph of the seven HPGe crystals composing a cluster of RISING (previously of Euroball).

The electronic signals to record the energy and time released in the γ detectors are processed with the XIA Digital Gamma Finder (DGF) [69]. Each DGF module handle the complete signal processing needed after the preamplification. The timing of the signals is recorded by three different circuits. One of them is the DGF module, which measure the timing with a resolution of 25 ns and a range of 100 μs. The other two time branches are traditional Time to Digital Converters (TDC): in this analog electronic chain the signals form the germanium detectors are processed by a Timing Filter Amplifier and a Constant Fraction Discriminator and then sent to the two types of TDCs. One of the circuits is called Long Range (LR), with a resolution of 0.7629 ns and a range of 100 μs, while the other TDC branch is called Short Range (SR) and it has a resolution 0.293 ns and a range of only 850 ns.

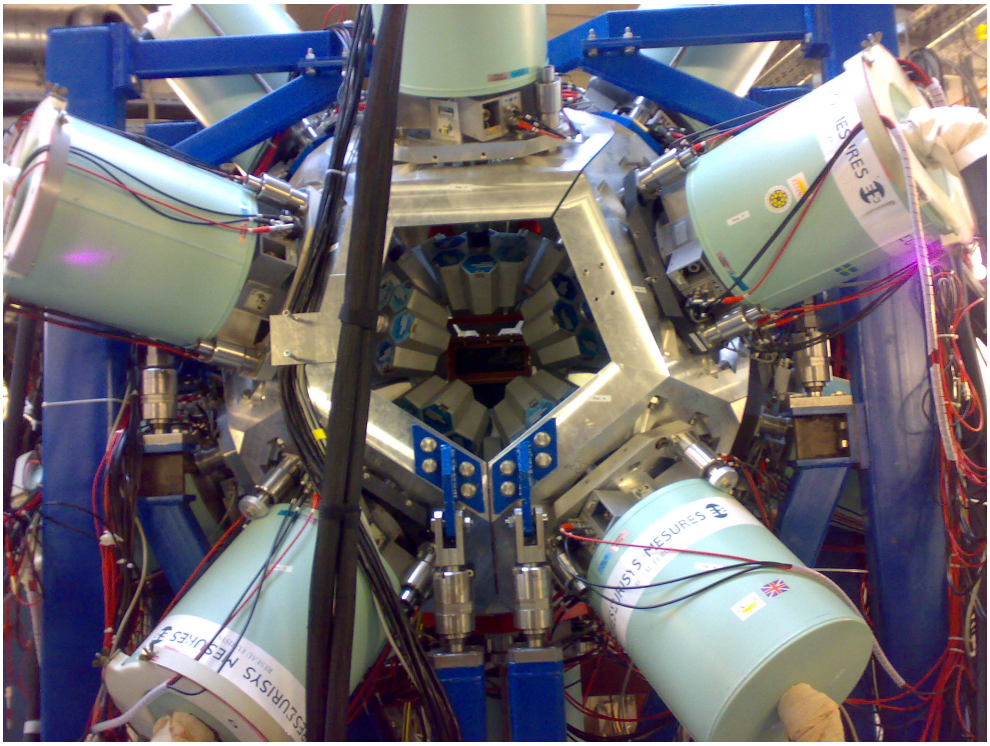

Figure 2.19: Photograph of the stopper at the centre of the RISING array. The close geometry of RISING is to maximize the γ-ray detection efficiency. Picture taken from Ref. [64].

Eventually one must do everything oneself in order to know something; which means that one has much to do!

Beyond Good and Evil - Friedrich Nietzsche

3 Experimental analysis

The present chapter describes the settings of the experimental setup used to perform the measurement as well as the the analysis methods exploited to obtain the results presented in Chapter 4.

3.1 Experimental settings

In order to study the nuclei of interest, several technical issues had to be overcome. The solution found for the aforementioned charge-state problem is described in detailed.

3.1.1 The primary-beam charge-state problem

The yield of nuclei with mass and atomic number not far from the primary beam is very large in relativistic fragmentation reactions. Considering that the required primary beam intensity is around 10^9pps, the production rate of ions which are only 1% of the total cross section is still very high compared to the detector capabilities. The first detector to interact with the secondary beam in the FRS is the scintillator at S2 (SC21), since the multiwire chamber is not used during the measurement, see Fig. 2.5. The maximum counting rate that SC21 can sustain is about 100 kHz: above this value pile-up starts to occur. Therefore, it is necessary to exclude from the acceptance of the spectrometer

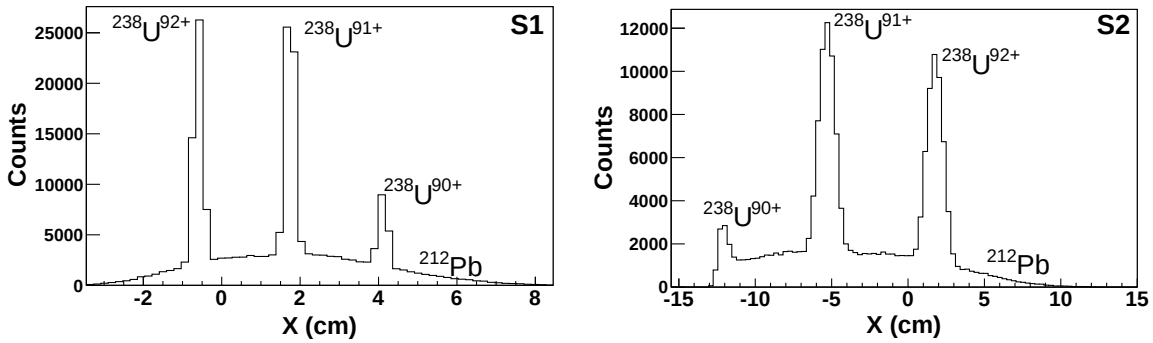

Figure 3.1: Spacial distribution of the charge states of the primary beam compared with the sum of the ones of ^{212}Pb. The intensity ratio between uranium and lead have been scaled down by five orders of magnitude for viewing purpose.

the unreacted primary beam and the most produced fragments before the S2 detectors. The two dipoles of the first stage in the FRS perform this task, provided the magnetic rigidity chosen for the central trajectory is different enough from the one of the primary beam and its neighbouring nuclei (and their charge states). This is not the case of the present experiment, where the A/Z of $^{212-214}$Pb is 2.585-2.610, while the uranium charge states 92+ and 91+ have an A/q of 2.587-2.615, respectively, thus almost identical to that of the lead isotopes of interest. The fully stripped, hydrogen-like and helium-like primary beam charge states have intensities $\sim 10^8$ pps, and thus their transportation to the detectors in S2 is not acceptable. Figure 3.1 shows the spacial distribution of uranium charge states in the horizontal direction at the S1 and S2 focal planes, compared to the distribution of ^{212}Pb (all its charge states are summed in the plotted distribution), which is the fragment most affected by this contamination. The calculations were performed with the code MOCADI [70]. The lead isotopes, and in general all the fragmentation ejectiles, have a wider spacial spread, while the primary beam distribution is peaked in space for kinematic reasons.

From Fig. 3.1 is evident that it is impossible to eliminate the primary beam charge states with the S1 or S2 slits without also reducing the yield of ^{212}Pb. In Ref. [39] the slits were used to cut the ^{238}U charge states and thus the yields were quite limited. In principle it would be possible to take advantage of the fact that the spacial distribution of the uranium charge states is much narrower than that of the fragmentation products by using a finger-shaped slit. This kind of slit is a few centimeters large piece of metal, of sufficient thickness, which can be moved along the dispersion direction of the spectrometer. It would then remove a uranium charge state if placed at the correct position, without absorbing too many fragments. However, even if this device was built and put in place, for this experiment it was decided to put a degrader at the first focal plane S1. The reason for this decision is twofold. On the one hand, there are at least two uranium charge states, ^{238}U^{92+} and ^{238}U^{91+}, to be eliminated with such device (^{238}U^{90+} can be eliminated

through a conventional slit), thus leading to the necessity of installing two finger slits. On the other hand, there are other fragments that are transmitted with a too high yield. These are reaction products close to the beam, as $^{235-236-237}$Pa, $^{232-233-234-235-236}$Th and $^{231-232-233}$Ac which all have a yield of the order 10^4-10^5 pps at S2. Their total rate would thus be well above the maximum counting rate allowed for the S2 scintillator. The most feasible way to eliminate these contaminants is to put a degrader at S1, in order to provide a selection in atomic number already in the first stage: the thickness has to be tuned so that these high-Z fragments are separated in $B\rho$ from lead isotopes enough to be eliminated with the S2 slits without cutting too much the lead nuclei. A homogenous aluminum degrader 2 g/cm^2 thick was placed at the S1 focal plane: its action is shown in Fig. 3.2, which presents the distribution of the most produced fragments before the S2 slits, compared to ^{212}Pb. Figure 3.3 shows the same distribution, but without degrader. The calculation have been performed using the LISE++ code [71]. The difference is evident: with the degrader the primary beam and the most populated fragments are much reduced in yield. However, the choice of placing a thick degrader

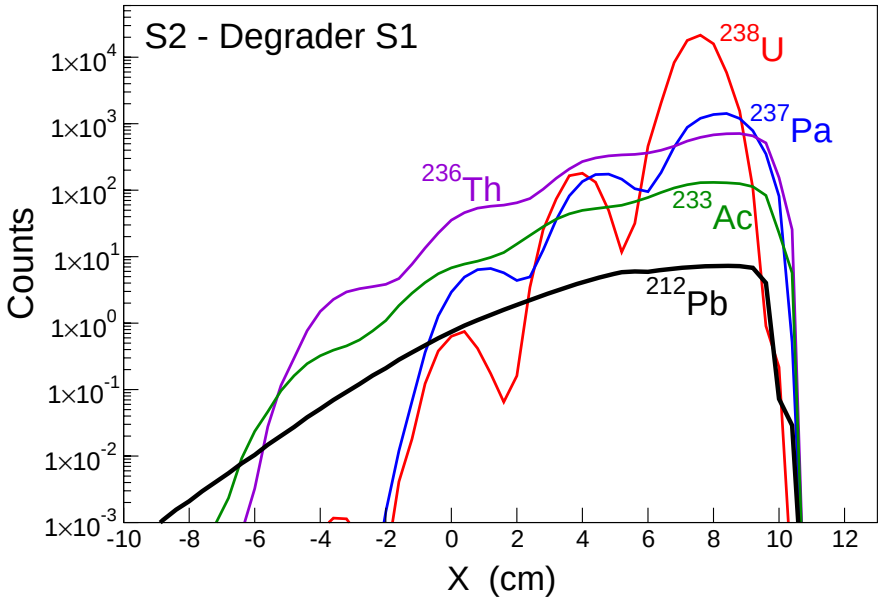

Figure 3.2: Spacial distribution at S2 of the primary beam and of the most populated fragments compared with the one of ^{212}Pb. All the charge states are summed. Situation with a 2 g/cm^2 degrader at S1.

requires to evaluate how many of the fragments change their charge state while passing through it. This is important because it means that a certain percentage of the ions will not arrive fully stripped at the S2 degrader, and this may create some ambiguity in the mass reconstruction, as the setup is only sensitive to changes in charge states

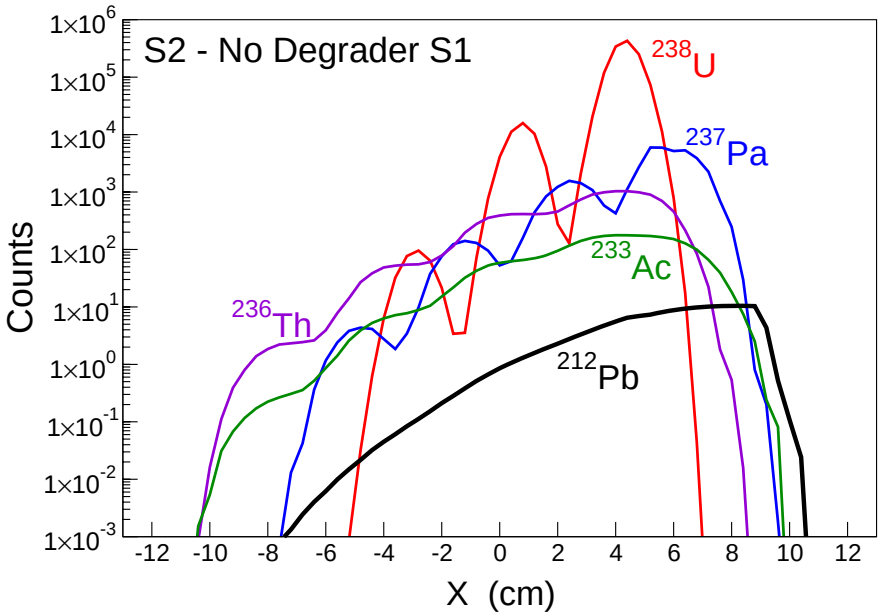

Figure 3.3: Spacial distribution at S2 of the primary beam and of the most populated fragments compared with the one of ^{212}Pb. All the charge states are summed. Situation without a 2 g/cm^2 degrader at S1.

	After target and stripper	After S1 degrader
^{212}Pb^{82+}	91.2 %	81.3 %
^{212}Pb^{81+}	8.7 %	18.3 %
^{212}Pb^{80+}	0.1 %	0.4 %

Table 3.1: Charge state population for the two stages of the FRS, before and after the S1 degrader of the FRS (see text for details).

through the S2 degrader. The calculation performed with the GLOBAL code [71, 72] gives the charge-state population (here shown for ^{212}Pb as an example) after the target and stripper to be compared with the one after the thick S1 degrader: the results are shown in Tab. 3.1. From the calculations it is evident that the charge state distribution is altered while passing through the S1 degrader, but the large majority of the ions remains fully stripped. Therefore, the main drawback of this thick degrader is only the loss in transmission, which, from LISE++ calculations, is about 20 %. The need to have this thick degrader at S1 had to be combined with the necessity of preserving, for heavy fragments, an energy sufficient to reach a good resolution in atomic number with the MUSIC detectors. For the very heavy fragments observed in this experiment the energy has to be 500 MeV·A or above at the entrance of the MUSICs, as shown in Ref. [73]. On the other hand, the thickness of the Be target is also fixed by optical and production

yields constraints, and was set at 2473 mg/cm^2. Considering all these restrictions, the thickness of the S2 degrader had to be as low as possible (compatibly with the optical function of the degrader in the FRS) to keep the ions at an acceptable energy. It was finally set at 731 mg/cm^2, with a profile shape to obtain a monochromatic beam.

3.1.2 The implantation degrader

The energy of the fragments arriving at S4 is around 500 MeV·A. In order to be implanted in the active stopper, the ion energy has to be about 100 MeV·A. This reduction in energy is achieved through a thick Al degrader placed at S4 before SCI42 and the active stopper, see Fig. 2.5. The thickness of the degrader was calibrated using the primary beam transported to the end of the FRS at different energies and by checking the number of implantation events in each of the three active stopper layers. The thickness was then scaled to lead isotopes, knowing the stopping power, to implant them in the middle layer.

3.1.3 Settings of the FRS

During the experiment two settings were used to populated the nuclei of interest: one centred on ^{215}Pb, for fragments around $^{212-216}$Pb, and one on ^{217}Pb to select more exotic nuclei.

^{215}Pb setting This setting was conceived to populate and implant nuclei from ^{212}Pb to ^{216}Pb, and nearby isotopes (bismuth, thallium and mercury). Since the lightest nuclei are also those more exposed to the contamination from primary beam as well as heavy fragments, it was necessary to close the slits at S1 and S2 to the positions (-35, 9.9) and (-19.1, 50) respectively, thus cutting the normal 200 mm x-space to about 70 mm, which resulted in very low rate of ^{212}Pb. At the end of the beam time a variation of this setting was attempted, to increase the transmission of ^{212}Pb. The slits were opened bringing the detectors at S2 and S4 at the limit of their counting rates, achieving a higher yield for lighter isotopes. Unfortunately, after few hours of working with this improved configuration the thickness of the degrader at S4 was changed by mistake and thus in the remaining hours of the beam time the lead fragments were not implanted in the DSSSD stopper. Table 3.2 shows the number of nuclei of interest implanted in the two ^{215}Pb settings. Figure 3.4 shows the identification plot for the implanted ions in the first ^{215}Pb setting, while Fig. 3.5 is for the second and shorter setting. Both plots refer only to fully-stripped ions.

^{217}Pb setting With this setting the goal was to select more exotic neutron-rich nuclei, possibly up to ^{218}Pb. At the beginning of this setting it was realized that the thickness of the degrader at the S1 focal plane was not set properly, being about 10% thinner than the desired value. This fact implied that, in the previous ^{215}Pb setting, the lead ions

	First ^{215}Pb setting	Second ^{215}Pb setting
^{217}Bi	5001	2245
^{212}Pb	111	360
^{213}Pb	954	1135
^{214}Pb	2385	1073
^{215}Pb	1933	784
^{216}Pb	927	283
^{217}Pb	402	100
^{218}Pb	130	53
^{211}Tl	1704	662
^{213}Tl	618	182
^{208}Hg	1228	434
^{210}Hg	363	97

Table 3.2: Number of ions implanted in the two ^{215}Pb settings. Only the most relevant isotopes are reported.

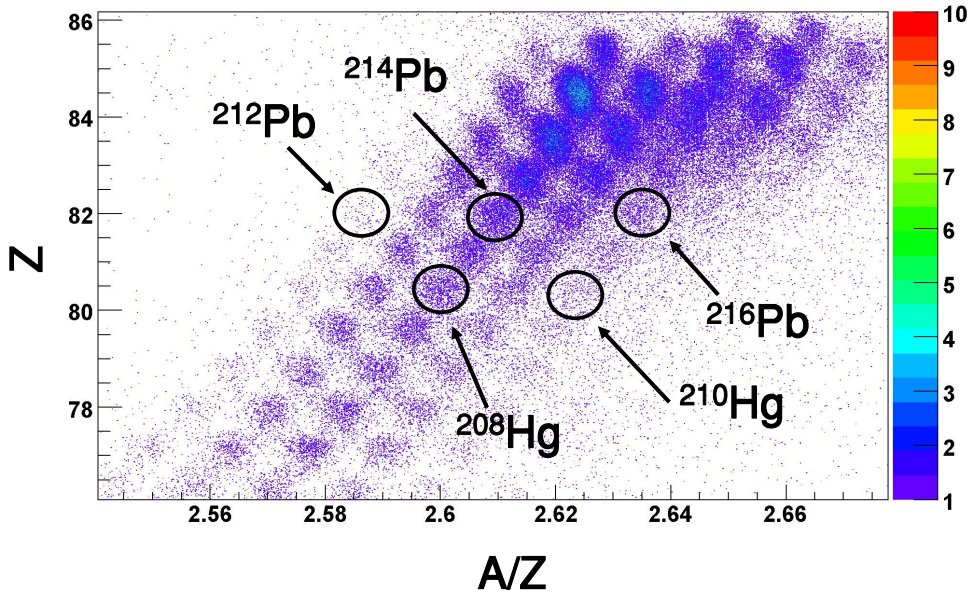

Figure 3.4: Identification plot for the first ^{215}Pb setting. In the ordinate the atomic number Z of the ion, in the abscissa its mass number A divided by the atomic number. Some nuclei are pointed out to provide a reference.

were not perfectly centered in the focal plane. Table 3.3 shows the number of nuclei of interest implanted in the two ^{217}Pb settings: the first one is with the wrong degrader thickness, and it is very short (few hours of beam time), the second one is the one with

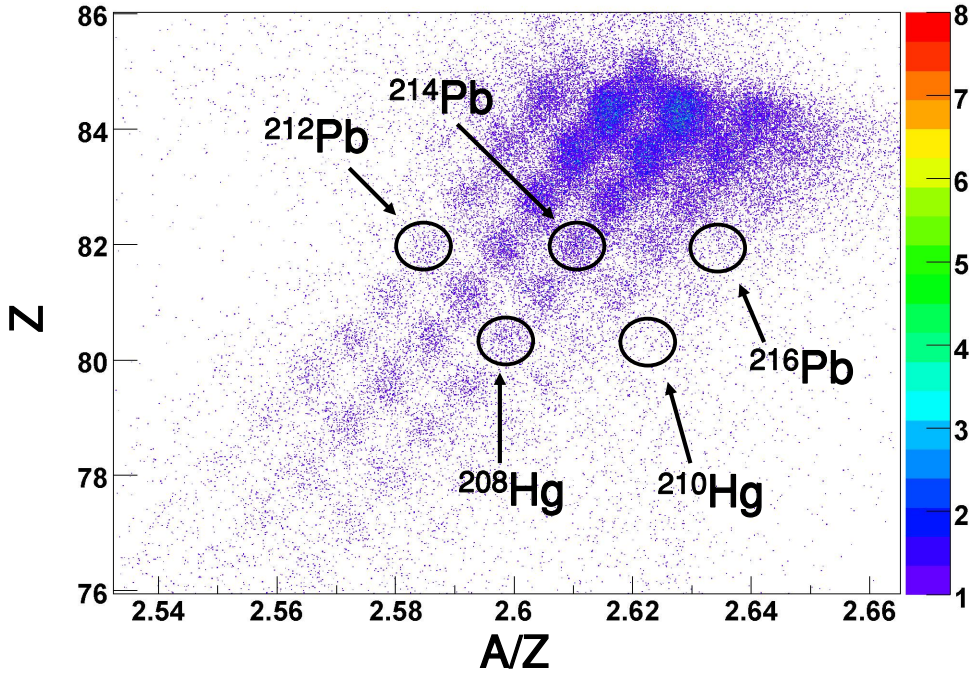

Figure 3.5: Identification plot for the second ^{215}Pb setting. In the ordinate the atomic number Z of the ion, in the abscissa its mass number A divided by the atomic number. Some nuclei are pointed out to provide a reference.

the correct degrader setting. Figure 3.6 shows the identification plot for the implanted ions in the first ^{217}Pb setting, while Fig. 3.7 is for the second and longer setting.

3.2 Analysis technique

The data have been analysed by using the software package GO4-Spy-Cracow [74, 75], specific for data handling at GSI, and the more general-purpose Root code from CERN [76]. The analysis method has been derived from previous PhD thesis [77, 78] and papers [50, 79, 25, 80] on experiments performed with a similar setup. Comparisons with existing data will be provided in this and in the following chapter: it will be shown that the results from the present work agree well with known data, where available, confirming the validity of the analysis technique employed.

3.2.1 Atomic number measurement

The measurement of the Z atomic number with a resolution sufficient to achieve a satisfactory resolution is one of the key challenges of the experiment. As shown in Ref. [73],

	First ^{217}Pb setting	Second ^{217}Pb setting
^{217}Bi	233	8160
^{212}Pb	2	63
^{213}Pb	9	837
^{214}Pb	90	2874
^{215}Pb	234	3356
^{216}Pb	251	2265
^{217}Pb	108	1136
^{218}Pb	40	620
^{211}Tl	32	464
^{213}Tl	108	1284
^{208}Hg	27	683
^{210}Hg	69	604

Table 3.3: Number of ions implanted in the two ^{217}Pb settings. Only the most relevant isotopes are reported.

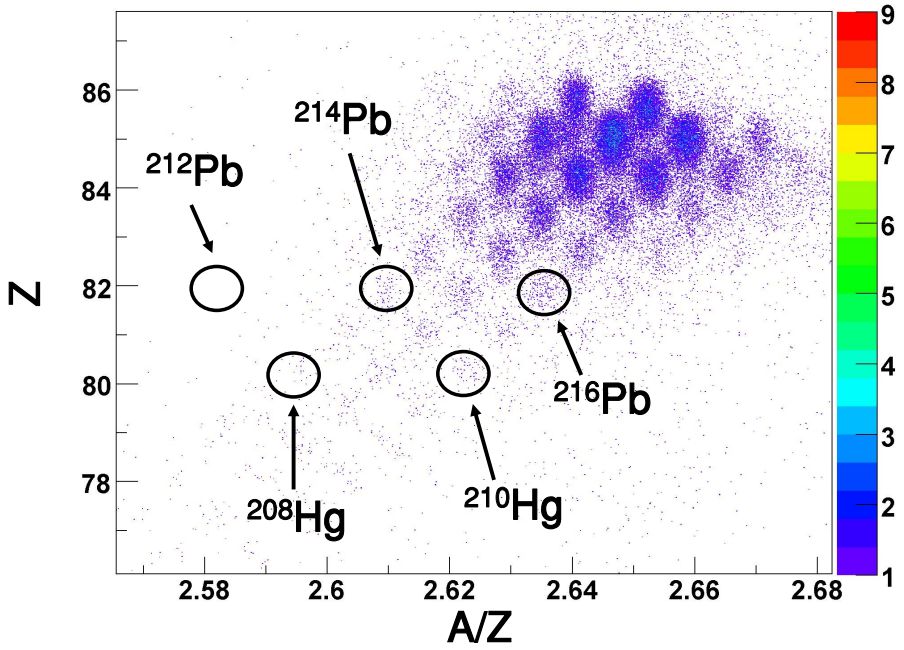

Figure 3.6: Identification plot for the first ^{217}Pb setting. In the ordinate the atomic number Z of the ion, in the abscissa its mass number A divided by the atomic number. Some nuclei are pointed out to provide a reference. The run only lasted a few hours: hence the scarcity of statistics.

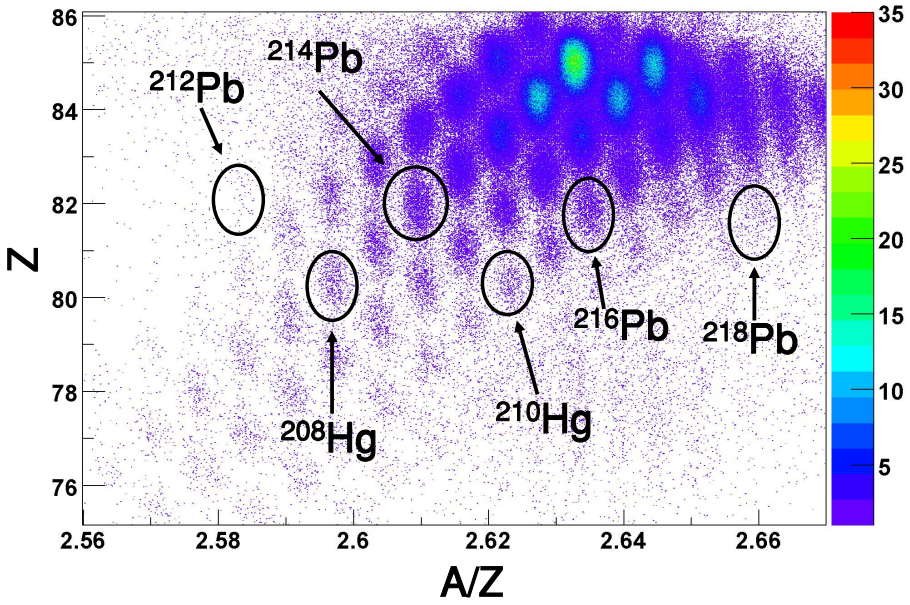

Figure 3.7: Identification plot for the second ^{217}Pb setting. In the ordinate the atomic number Z of the ion, in the abscissa its mass number A divided by the atomic number. Some nuclei are pointed out to provide a reference.

the crucial aspect is to have ions of sufficient energy (around 500 MeV·A) arriving in the ionisation chamber. This is accomplished by the FRS setup described above. Another important point is obviously the calibration of the two ionisation chambers. The energy deposited depends not only on the atomic number Z, but also on the velocity of the ions, according to the Bethe-Block formula, and on the path length inside the chamber. The calibration is performed with a primary beam of ^{238}U of very well-defined magnetic rigidity, transported through the FRS. Three different velocities of the ions were used, obtained by inserting matter layers along the beam line. For each velocity a calibration point was set for every one of the sixteen sections of the two MUSIC chambers. The energy loss was then derived as the mean value of the eight anodes. This procedure enables to calibrate at the same time in atomic number with an absolute reference point (the Z of the primary beam) and to correct the velocity dependence of the Bethe-Block formula. The three points are a compromise between the time required by setting the FRS to the desired magnetic rigidity (about an hour) and a sufficiently effective Z calibration. However, since the Z measurement depends on the on the ion path length inside the detectors, it has to be corrected to achieve the desired resolution. In fact, the energy deposit inside the gas varies according to the trajectory of the ion, and thus on the x and y positions along the beam line. This effect, shown in Fig. 3.8, can be corrected by recalibrating the energy loss with a fifth order polynomial to eliminate the spacial

dependence. The final atomic number estimation is obtained by averaging the values from the two MUSICs available.

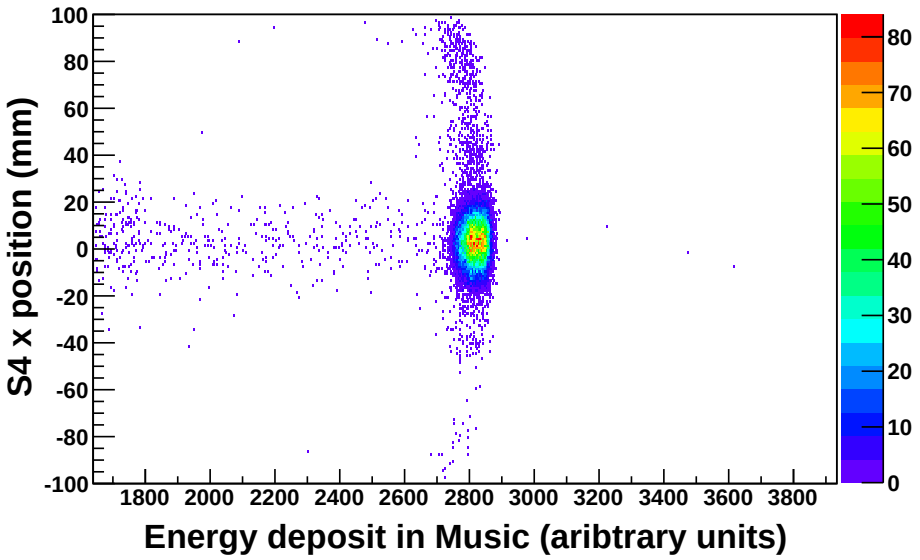

Figure 3.8: Dependence of energy loss in one MUSIC detector with respect to the x position at S4.

3.2.2 Magnetic rigidity: A/q determination

The A/Z ratio for an ion is determined by measuring the Time Of Flight (TOF) and the position in the x coordinate at S2 and S4. The TOF measurement is performed by using the time signals from SCI21 and SCI41 and it is calibrated using the three FRS settings for the primary beam also exploited for the Z calibration. Since in each of these settings the primary beam has a well-defined magnetic rigidity and hence velocity (the A/Z of the primary beam is obviously known), it is possible to calibrate the velocity as a function of the measured TOF. The magnetic rigidity $B\rho$ of a known ion is then calculated from the position measurements in S2 and S4 according to the formula:

$$B\rho_4 = (B\rho_0)_4\left(1 + \frac{x_4 - Mx_2}{D_4}\right) \tag{3.1}$$

where $B\rho_4$ and $B\rho_0$ are the magnetic rigidities in the second stage of the FRS and in the central trajectory, respectively; M is the magnification of the second stage of the spectrometer and D is the dispersion of the second stage of the spectrometer. Therefore,

the A/Z of the ion, once the velocity is obtained from TOF, is:

$$\frac{A}{q} = \frac{B\rho}{\beta\gamma} \tag{3.2}$$

The resolution in the A/Z ratio is affected by various factors: mainly the TOF resolution and the position resolution at the focal planes. However, also other abberations are present, and one of the most important is the chromatic abberation, i.e. the velocity of the ion measurement actually depends on the specific trajectory of the ions. Figure 3.9 shows the dependence of the velocity on the entrance angle of ions at S2 (the figure is gated on ^{214}Pb). The two lines corresponds to the main two charge states of ^{214}Pb: the fully-stripped ions are in the most populated region, while the hydrogen-like ions are in the other line.

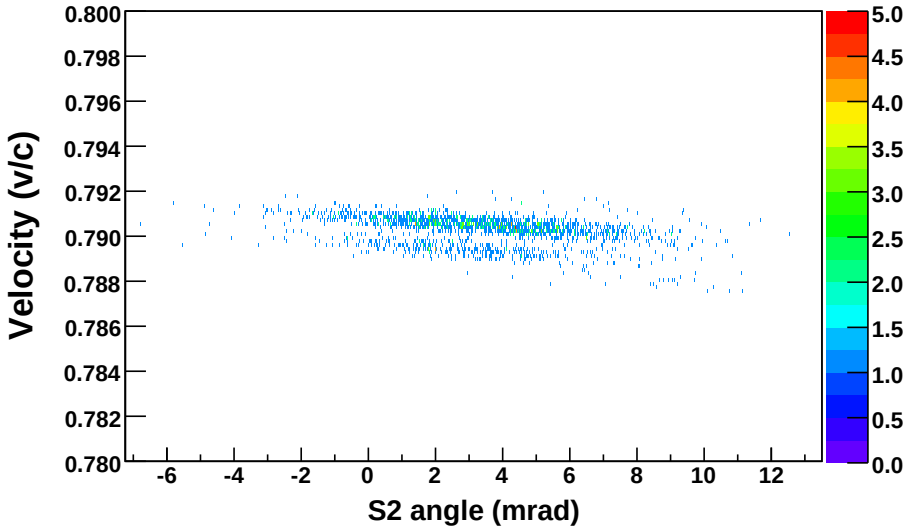

Figure 3.9: The velocity (β) of the ^{214}Pb fragments plotted versus their entrance angle in the second section of the FRS.

This effect is corrected by a recalibration of the velocity as a function of the entrance angle. Another important distortion of the A/Z ratio is its possible dependence from the x coordinate at S2 and S4: this was corrected by changing the focal planes positions when calculating the ion path and by recalibrating the A/Z versus the x position. The resolution achieved was satisfactory for all the settings, as it demonstreated in Fig. 3.4, Fig. 3.5, Fig. 3.6 and Fig. 3.7.

3.2.3 Definition of an implantation event

The trigger of the FRS-RISING system for an implantation event is provided by the scintillator SCI42. However, not all the events that are accepted by the trigger threshold are good events, even if correctly identified in Z and A/Z by the FRS. In fact, some ions may have an energy low enough to be stopped inside the SCI42 (and thus outside the RISING array), while some may have an energy too high to be stopped in the three DSSSD layers. It is also possible that the event detected by SCI42 is the result of a fragmentation reaction in the S4 degrader, placed just before SCI42. Figure 3.10 shows the atomic number plotted versus the energy loss spectrum for SCI42. The parabolic-shaped region (encircled) is the one selected for the analysis because it corresponds to ions passing through the scintillator: the energy deposit is, in fact, a function of Z^2. The smaller, less populated, parabolic region at higher energy is actually constituted by the non fully-stripped fragments. The other region with lower energy deposit at large Z corresponds to ions fragmented in the degrader and thus it is excluded from the analysis. For heavy ions, Z>85, the spectrum shows a continuum structure with a peak at low energy. This peak can be justified considering that a lot of heavy fragments are stopped in the S4 degrader, and thus only electrons from their implantation or light fragments from secondary reactions reach the scintillator SCI42, releasing a small amount of energy. The continuous structure around Z = 86 can possibly be due to the heavy fragments passing the degrader but implanting in SCI42.

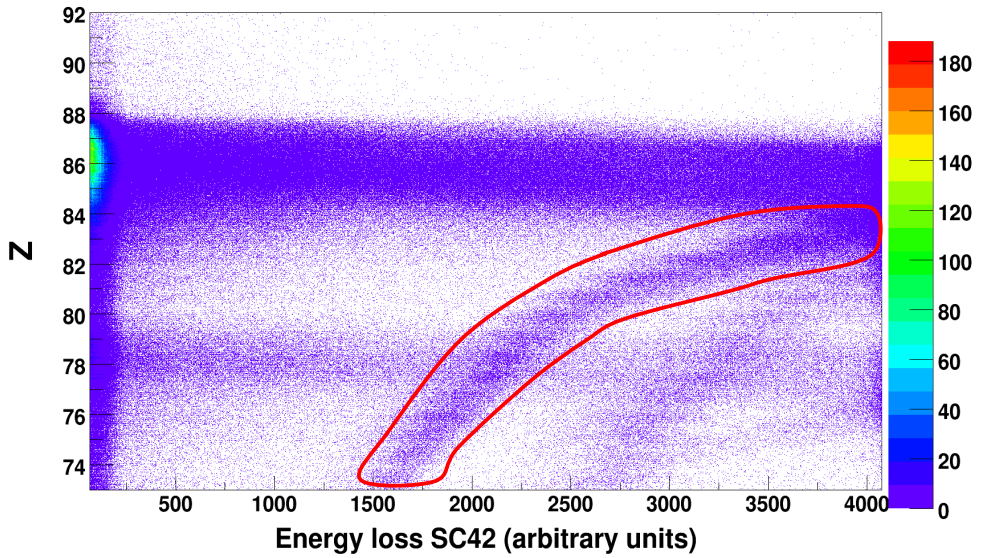

Figure 3.10: Atomic number plotted versus the energy loss in SCI42. The events corresponding to a real implantation are encircled.

The ions not implanted in the DSSSD layers because too energetic are detected in

SCI43. This scintillator detects also the electrons and light particles produced by every implantation event. Figure 3.11 shows the atomic number plotted versus the energy loss spectrum for SCI43. The region selected contains the electrons and light particles from implantations, but also from every ion simply passing through the stopper, as it will be discussed later when commenting on the effect of the different gates.

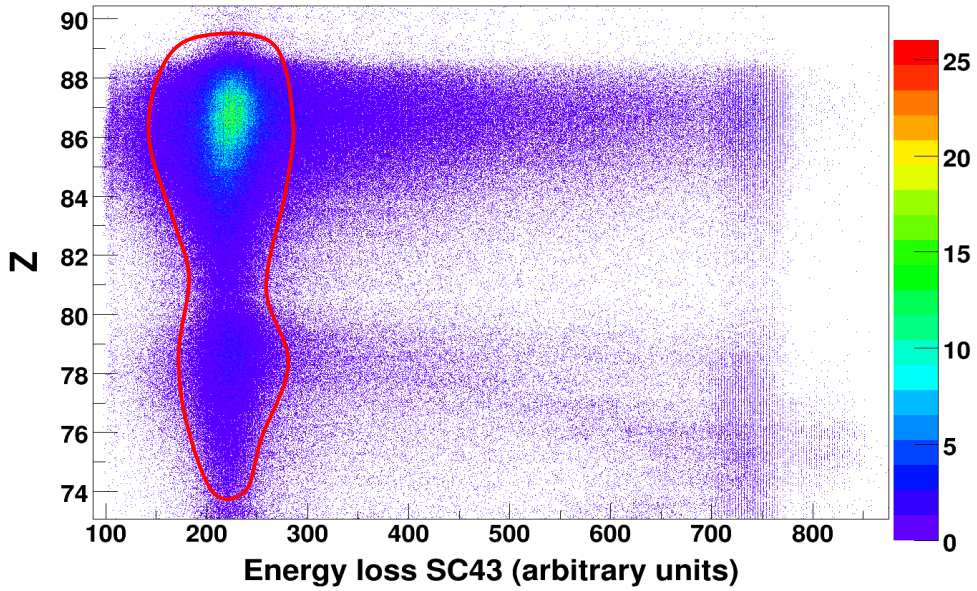

Figure 3.11: Atomic number plotted versus the energy loss in SCI43. The selected events are electrons coming from the DSSSD after an implantation of an heavy ion.

3.2.4 Isomer spectroscopy

Once the ion identification in the FRS is achieved, it is possible to search for the presence of isomers by measuring their γ decay. Extensive results will be presented in the next chapter: in this section only the general analysis method is illustrated. Figure 3.12 shows the energy of the detected γ rays plotted against the time measured by the DGF for ^{214}Pb. The structure in the time range below 1 μs is the prompt or flash peak, and it corresponds to the bremsstrahlung from the stopping processes in the materials close to the γ detector. Also light ions coming from beam-matter interaction in the FRS give an important contribution to this process. Figure 3.13 presents a more detailed view of this region. It can be observed that the flash peak extends in time at low energy. This is due to the "walk effect": low energy γ rays tend to deposit their energy in small regions on the surface of Ge crystal, as their absorption coefficient is high. For this reason the time resolution at low energies is worse, hence the broader flash peak. This peak actually

defines the zero point of a relative time scale respect to which the isomer lifetime is then measured. The gate condition, see Fig. 3.12, in the peak excludes the prompt region and select a zone where the time distributions of three γ rays are clearly visible: at low energies the gate is adapted to the broader shape of the flash peak, see Fig. 3.13. The projection of this region of the matrix on the energy axis is displayed in Fig. 3.14, which clearly points out the three γ transitions occurring after an isomeric-state decay.

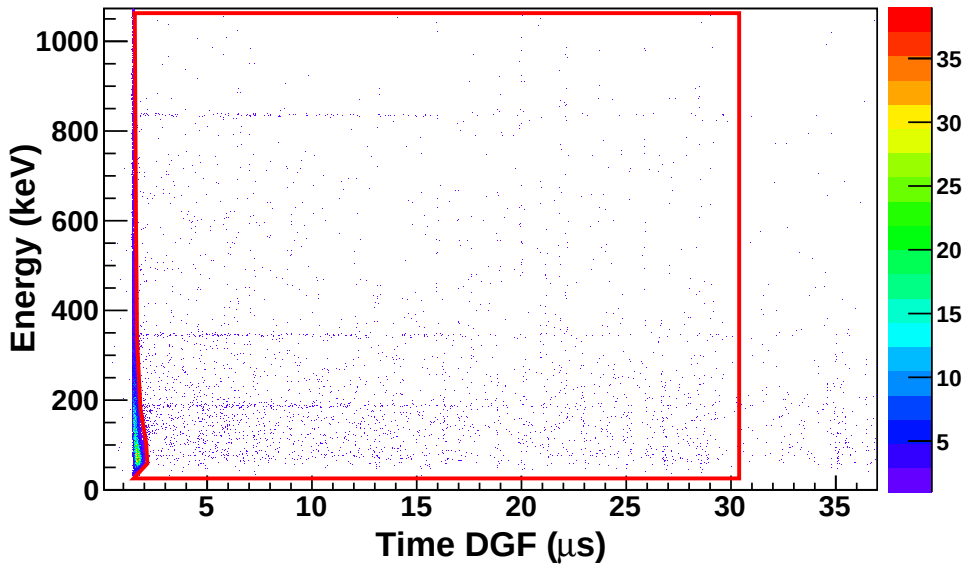

Figure 3.12: Time-γ energy matrix for the isotope ^{214}Pb. The time is provided by the DGF electronics.

3.2.5 Selection of the charge state

In some of the previous figures (Fig. 3.9 and 3.10) at least another charge state besides the one of fully-stripped ions was present. In addition to the ions that are not produced initially fully stripped, the creation of charge states may also occur along the whole FRS, whenever the beam is passing through a layer of matter (detectors, degraders). The probability of an electron stripping or picking up is greater for the thicker layers, for example for the degraders in S1 and S2. It is possible to detect a change in the charge state when passing through the S2 wedge by measuring the $B\rho$ before and after the wedge. The magnetic rigidity after the dispersive focal plane is calculated as described above, while the one in the first section of the spectrometer is obtained by assuming that the beam is centered on the target, and thus the position S0 is known:

$$B\rho_2 = (B\rho_0)_2\left(1 + \frac{x_2 - Mx_0}{D_2}\right) \tag{3.3}$$

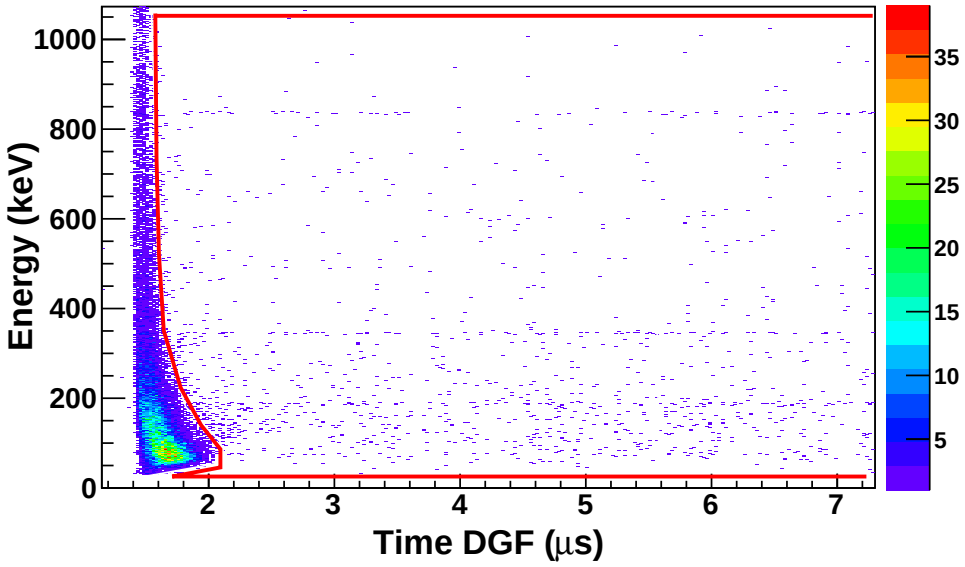

Figure 3.13: Time-γ energy matrix for the isotope ^{214}Pb. The time is provided by the DGF electronics. This figure is an expansion of the low-time region of Fig. 3.12.

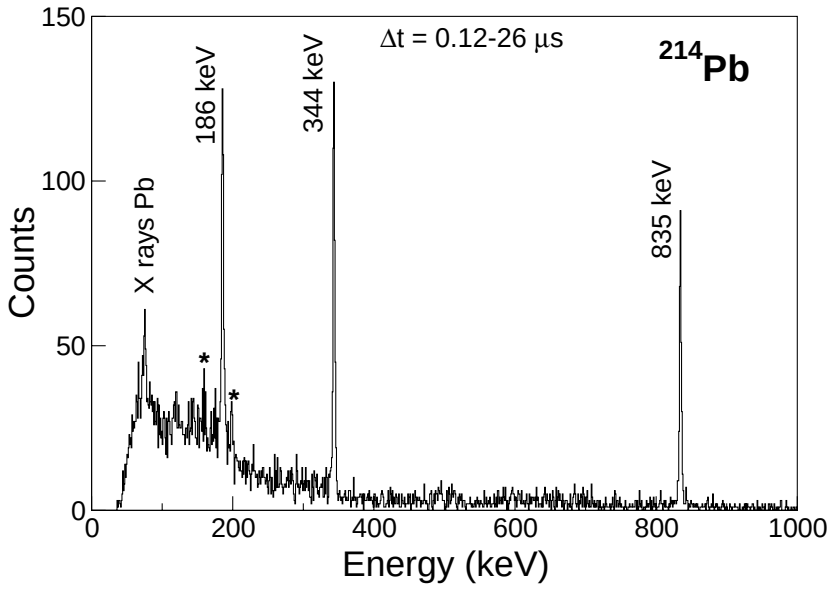

Figure 3.14: The γ spectrum of ^{214}Pb obtained from the time gate in the time-γ matrix shown in Fig. 3.12. The time gate indicated in the picture is referred to a time scale starting from the implantation instant.

where $B\rho_2$ and $B\rho_0$ are the magnetic rigidities in the first stage of the FRS and in the central trajectory, respectively; M and D are, respectively, the magnification and the dispersion of the first stage of the spectrometer. The change in magnetic rigidity is related to the energy loss in the degrader, and hence the different charge states changes can be seen by plotting the atomic number versus the energy loss through the degrader. Figure 3.15 shows the charge state discrimination for the first ^{215}Pb setting. The most intense region is the one where the ions do not change their charge state through the S2 wedge. Above it, two other zones are distinguishable, corresponding to the ions picking up one or two electrons from the matter they pass through. Below the region of $\Delta q = 0$, the (not fully-stripped) ions that have lost one electrons while passing the matter at S2 are in the gate $\Delta q = +1$. The different charge states have different A/q ratio, but

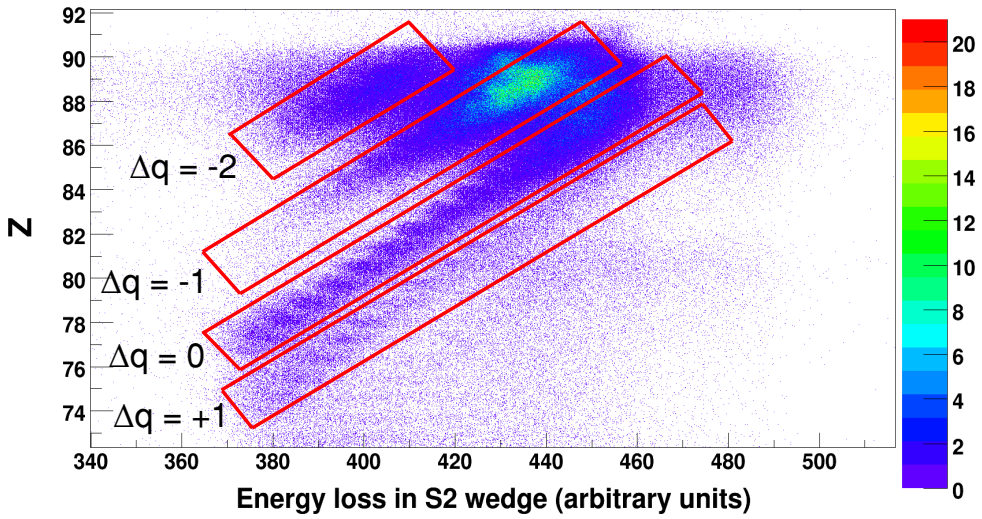

Figure 3.15: Atomic number plotted versus the energy loss in the wedge at the second focal plane of the FRS (S2), determined through the change in magnetic rigidity. The different charge-state changes through the wedge at S2 are clearly visible.

they can be included in the analysis by taking into account this shift. In particular, the $\Delta q = +1$ and $\Delta q = -1$ ions have a quite large statistics with respect to the fully-stripped case. From Global [71, 72] calculation the probability of a charge-state change for a lead ion is in fact around 20-25%. However, it is also necessary to take into account that the FRS transmission can vary for different charge-states. For example, the hydrogen-like fragments of an ion in a central trajectory will have a larger A/q with respect to their fully-stripped counterparts, and they will thus have more peripheral trajectories. From this point of view, the larger gain in statistics by the inclusion of the $\Delta q = -1$ charge state will be achieved for ejectiles such as ^{212}Pb, which have one of the smallest A/q transmitted by the FRS and whose fully-stripped ions are partially cut by the FRS

slits. Figure 3.16 shows the comparison between the isomeric spectrum of ^{212}Pb with a gate on the fully-stripped fragments and with a gate on all charge states. The increase in statistic is evident: the area of the 805 keV peak goes from 14(4) to 39(7) counts. Although the improvement is significant, it has to be considered that for other nuclei it will be much smaller or almost absent for the very exotic (large A/q) species. It is important to remember that the inclusion of charge states can lead to contamination from other isotopes. This is evident in Fig. 3.16, where three peaks, marked by an asterisk, appear when Δq = $\pm$1 are included. Their origin is not clear, but they probably come from heavier fragments whose ratio A/q is equal to 212/81. Nevertheless, the gain in statistics can prove essential to obtain lifetime estimates with smaller errors or to perform $\gamma - \gamma$ coincidences.

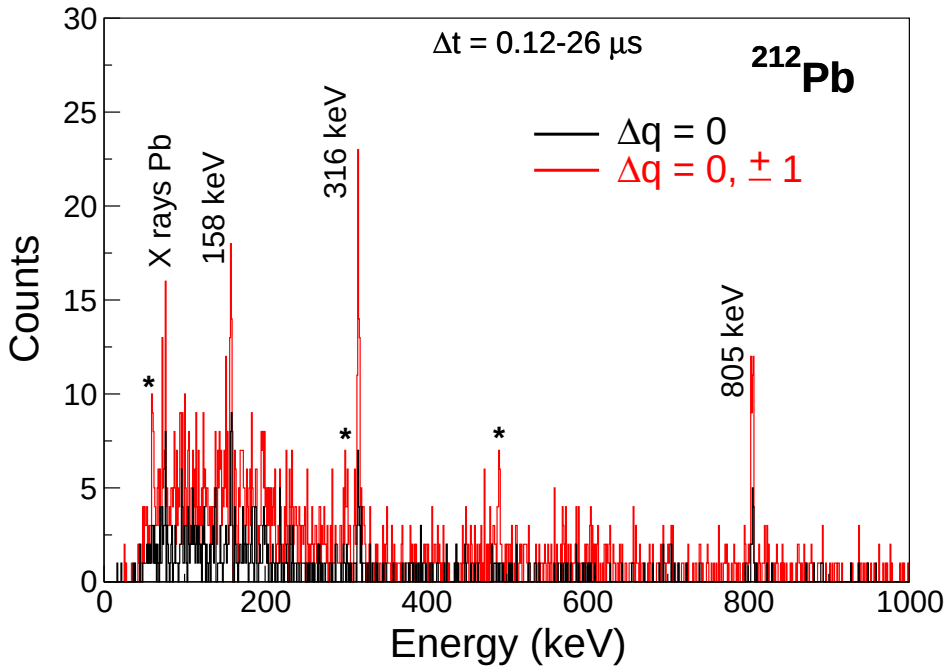

Figure 3.16: Comparison between the γ-ray spectra for ^{212}Pb when the charge state has not changed ($\Delta q = 0$) and when it changes up to one unit ($\Delta q = 0, \pm 1$).

3.2.6 Multiplicity gate

An important issue in the RISING Stopped beam campaign at GSI has been represented by the atomic background coming from the beam, and originating by its interactions with the layers of materials along the FRS [81]. This background is actually the sum of various contributions:

- Bremsstrahlung from the incoming ions
- K and L shell X rays from the ionised DSSSD (silicon) atoms
- Radiative internal conversion of the DSSSD (silicon) electrons into the projectile K and/or L shells
- Primary bremsstrahlung from the DSSSD (silicon) electrons produced by the collisions of the fragments
- Secondary bremsstrahlung from energetic knock out electrons re-scattering in the stopper and/or surrounding material

These processes determine the presence of high multiplicity events at low energies, mainly concentrated in the prompt flash that can be excluded using a time gate to cut off the prompt events and observe isomeric decays. However, due to the internal structure of the spill from the accelerator, and to the high ($\sim$ 2 kHz) implantation rate in the stopper detector, this beam-related background actually also contributes as a noise in the γ-spectra. In order to eliminate this background and improve the Peak-To-Total ratio (P/T) of the γ spectra, a multiplicity gate on RISING detectors has been exploited. The gate has been decided under the assumption that the background will produce a high multiplicity event in a single cluster. This hypothesis is justified by the fact that the atomic background is focussed in a certain direction, due to the kinematic boost from the relativistic beam (β $\sim$0.9 %). As a consequence, the flash of radiation will hit mainly neighbouring crystals. Therefore, the condition of having only one event per cluster (i.e. seven adjacent crystals) is applied. It may be argued that the condition also erases almost all the Compton scattering background, which could be recovered by performing the addback procedures. However, in the nuclei of interest the γ rays of interest are well below 1 MeV, and thus the addback procedure brings negligible statistics due to the lower cross section for Compton scattering. Figure 3.17 shows the effect of such a gate on the isomeric spectrum of ^{214}Pb. The reduction of the peak areas is small compared to the decrease of the background, especially at low energy. In the following we will quantify the effect of the various gates which have been discussed in this chapter: see Table 3.4. The ^{214}Pb isomer measured in the second ^{217}Pb setting has been chosen for an exemplification. The numbers reported on the table show that the selection of the charge state $\Delta q = 0$ removes about half of the background with a decrease of the peak areas of about 20-25%. Thus, as noted above, the inclusion of other charge states increases the statistics of the desired isotope but also introduce contaminations. The effect of the multiplicity gate is also important, as it removes about half of the background, at the cost of only a small decrease of the peak areas of interest (which are actually compatible, within errors, with the areas in the absence of the gate). The gate on the energy loss in SCI42 is also effective, as it decreases the background by more than 10%, while the areas of the transitions are unaffected. On the contrary, the gate

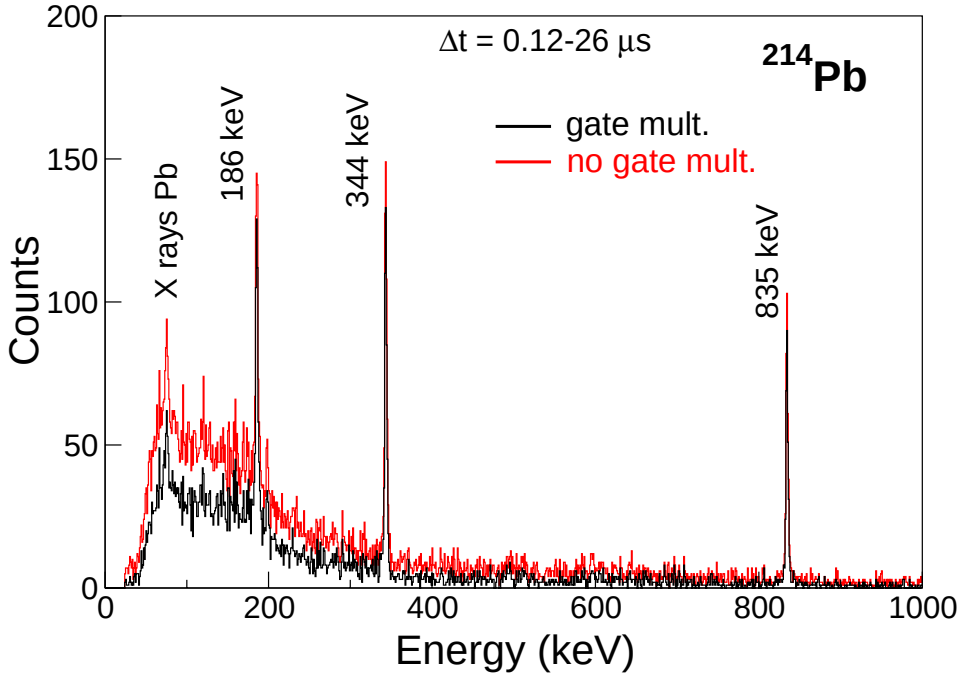

Figure 3.17: Comparison between the γ-ray spectra associated to ^{214}Pb with and without the gate on multiplicity in RISING to improve the P/T ratio.

^{214}Pb	Area (counts)			
Gates applied	Total	186 keV	344 keV	835 keV
No gate	9800	171 (19)	193 (35)	149 (23)
RISING multiplicity (mult.)	5191	149 (18)	170 (24)	120 (20)
SCI42	8859	170 (17)	195 (35)	150 (23)
dq0	5697	142 (17)	141 (33)	109 (18)
SCI43	9450	170 (19)	191 (36)	148 (21)
mult. & SCI42 & SCI43	2834	128 (21)	122 (22)	102 (10)

Table 3.4: Effect of different gates on the number of counts of the γ peaks. Data coming from the second ^{217}Pb setting, for the nucleus ^{214}Pb. Total refers to the number of ions implanted, the 186-, 344- and 835-keV transitions are those related to the decay of the isomer in ^{214}Pb.

in SCI43 is not particularly useful, because all the ions, implanted or not, are producing the electrons which are inside the gate shown in Fig. 3.11.

3.2.7 Isomer lifetimes

The lifetime of the observed isomers has been determined by performing an exponential fit to the decay curves of the γ transitions following the isomers. For all the γ lines observed, even if supposed to belong to the same cascade, the time distribution was analysed. A time spectrum was obtained by gating on each transition in the time-γ energy matrix shown in Fig. 3.12. The subtraction of the background is a delicate matter, as the decay curve of the background is dominated by components shorter than the lifetimes usually measured ($\sim$ μs). This may be due to the atomic background surviving all the gates for very short-lived isomers, to the activity created in the silicon stopper by the incoming fragments or to the internal structure of the spill from the accelerator. This problem is particularly evident in the low-energy region ($\sim$ below 250 keV), where the background is higher. Background subtraction is performed by gating on the time-γ energy matrix on wide energy regions ($\sim$ 20 keV) below and above the transition energy and by subtracting the obtained time spectrum from the one in coincidence with the transition. The spectrum from the background is normalized to the one from the peak. The errors on each bin are taken following the Poisson statistics ($\Delta N = \sqrt{N}$) and are then combined in quadrature to obtain the errors on the final time spectrum. Figure 3.18 shows a typical exponential decay fit for ^{214}Pb. The fit function is

$$f(t) = ce^{-\frac{t}{\tau}}$$

where t is the time (25 ns steps from DGF), τ the lifetime and c a multiplicative constant. The fit is performed with the minimization of the χ^2 function. The errors of the fitted parameters c and τ are obtained from the inverse of the Hessian matrix of the χ^2 function ("parabolic errors"). As stated above, the presence of a background in the time-γ energy spectra may interfere with the lifetime determination, especially at low energies where it is higher, if it is not subtracted properly. The alteration of the measurement will consist in a reduction of the estimated $t_{1/2}$ value, as the background decays faster than the μs isomers observed. These considerations are indeed proved in Tab. 3.5, which presents the lifetime results for ^{214}Pb. The three transitions belong to the same cascade (see next chapter) and should thus have half lives compatible within errors. The low-energy transition gives a shorter half life than the other two when the multiplicity gate is not present, but when it is reintroduced $t_{1/2}$ increases and becomes compatible with that derived from the other two transitions. It seems reasonable to extract the lifetime of the isomer from the sum of the two higher energy transitions, with the multiplicity gate applied when the statistics allows it, as done in Fig. 3.18.

The timing spectra The DGF and LR TAC circuits, which both have a range of 100 μs, were verified to give consistent results. The SR TAC was employed for short isomers of the order of 100 ns, as the one in ^{208}Hg described in the next chapter. Also the SR TAC gives an estimate compatible with the DGF. The SR and LR TAC were

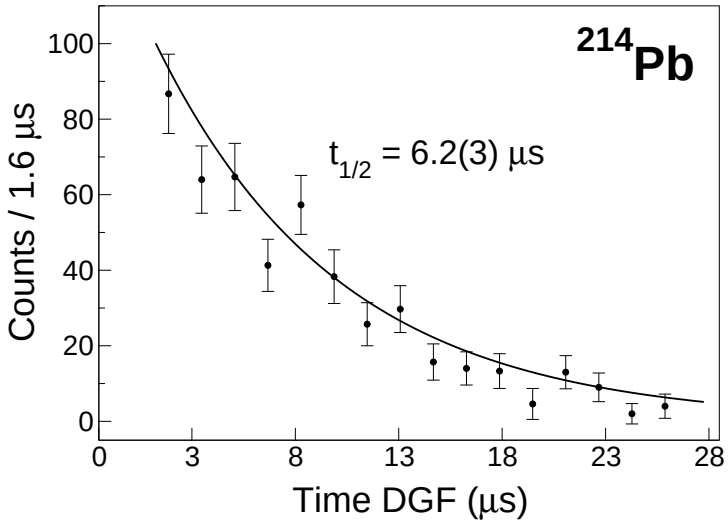

Figure 3.18: Exponential fit to the summed time distribution of the 344 keV and 835 keV decay curves.

Transition energy (keV)	$t_{1/2}$ without mult. gate (μs)	$t_{1/2}$ with mult. gate (μs)
186	5.1 ± 0.5	5.7 ± 0.7
344	6.2 ± 0.4	6.0 ± 0.5
835	6.0 ± 0.5	6.4 ± 0.5
186 & 344 & 835	5.8 ± 0.3	6.2 ± 0.3
344 & 835	6.3 ± 0.3	6.2 ± 0.3

Table 3.5: Half lives derived from the time distributions of the γ lines of ^{214}Pb, applying or not the multiplicity gate in RISING. Without the multiplicity gate, the half life deduced from the time distribution of the 186-keV line is smaller than that obtained from the 344- and 835-keV lines. When the gate is applied, the deduced half lives are compatible within errors.

not calibrated, but only aligned in time. In fact, given the bad timing resolution of a Ge detector (∼20 ns), the channel/ns conversion given in the technical specifications of the modules is accurate enough.

Gamma efficiency In order to compare the intensities for the γ-ray transitions, the areas of the peaks have to be corrected by the efficiency ε of RISING, which is not constant as a function of the γ-ray energy. The relative efficiency calibration was obtained by using ^{152}Eu and ^{133}Ba sources, the same also used to calibrate in energy RISING. The γ emission of these isotopes is known, and their γ rays are in an energy interval from

about 100 keV to about 1.4 MeV. The measured areas of the γ lines were fitted with the software RADWARE [82]. This software uses a seven-parameter formula to fit the measured intensities:

$$\varepsilon = e^{[(A+Bx+Bx^2)^{-G}+(D+Ey+Fy^2)^{-G}]^{-\frac{1}{G}}} \tag{3.4}$$

where A, B, C, D, E, F, G are the fit parameters (C set to 0 [82]), $x = \log(E_\gamma/100)$, $y = \log(E_\gamma/1000)$ and E_γ is in keV. The obtained relative efficiency curve, shown in Fig. 3.19, was then scaled to absolute efficiency using data from a ^{60}Co source. In fact, the decay of this nucleus has two γ rays in coincidence at 1173 keV and 1332 keV. From the comparison of their areas it is possible to extract the absolute efficiency at one of the two energies: the relative efficiency curve is then scaled to absolute values. In principle, it is also possible to derive the absolute efficiency from a measurement of the number of counts in a specified period of time, knowing the activity to the employed γ source. However, the calibration source data were not taken with a trigger given by the OR of the Ge crystals. On the contrary, the trigger for γ calibration was provided by a clock of 1 kHz opening at each pulse an acquisition window of 100 μs. In this way, the acquisition time was only about 10% of the real time, making it impossible to use the activity of the source as a precise reference.

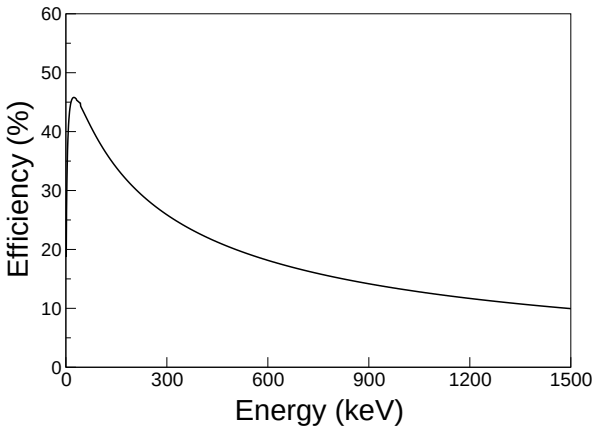

Figure 3.19: The relative efficiency curve for the RISING array deduced from the calibrations for the present experiment.

3.2.8 Comparison with known isomer lifetimes

In order to provide a calibration point for mass and atomic number, the FRS was set to implant ^{205}Pb and neighbouring isotopes at the beginning of the experiment for a few hours. In fact, the region of ^{205}Pb is well known, it is close to the nuclei of interest and here several isomeric states in the μs have been measured in the past. Table 3.6

shows the comparison among the half lives measured with our setup and those known from literature: the overall agreement is very good. Other two isomers populated in this experiment, in ^{212}Pb and in ^{208}Hg, are known and can be used for a consistency check: in the next chapter it will be shown that our half lives are well compatible with those reported in literature.

	$t_{1/2}$ (μs)		
	^{203}Tl	^{206}Pb	
Isomer I^{π}	$(25/2,29/2)^{-}$	7^{-}	12^{+}
Present measurement	7.9(2)	119(26)	0.208(11)
Data from literature	7.7(5)	125(2)	0.203(3)

Table 3.6: Half lives for some of the two isomers observed in the ^{205}Pb run. Half lives for ^{206}Pb are reported in Ref. [83, 84, 85], and for ^{203}Tl in Ref.[39].

Horatio: O day and night, but this is wondrous strange!
Hamlet: And therefore as a stranger give it welcome.
There are more things in heaven and earth, Horatio,
Than are dreamt of in your philosophy.

Hamlet – William Shakespeare

4 Results from Isomer-Decay Spectroscopy

In the present chapter the new results obtained from isomeric-decay γ spectroscopy are reported. For all the observed isomers, most of them seen for the first time (see Fig. 4.1), the γ spectra and the isomer decay curve are shown. The error on all the γ-ray energies is 1 keV. The information is complemented by the coincidence $\gamma\gamma$ matrix and by the measurement of the transition intensities, to understand the decay path of the isomeric states and to reconstruct the level scheme. The calculation of electron conversion coefficients is essential for this task, and is performed using the program BRICC [19, 20]. A tentative level scheme is drawn, but the comparison with shell-model calculations and the related theoretical discussion will be presented in Chapter 5. For the nuclei in which no isomer was observed although expected, the time-γ energy matrix is provided as an evidence of the absence of long-lived states.

4.1 Even-even lead isotopes

The even-even lead isotopes, from ^{212}Pb to ^{218}Pb, were the main aim of the experiment. A first interpretation of the isomers observed is provided by the systematics and by the seniority scheme (see next chapter). The nucleus ^{210}Pb, which has two neutrons more

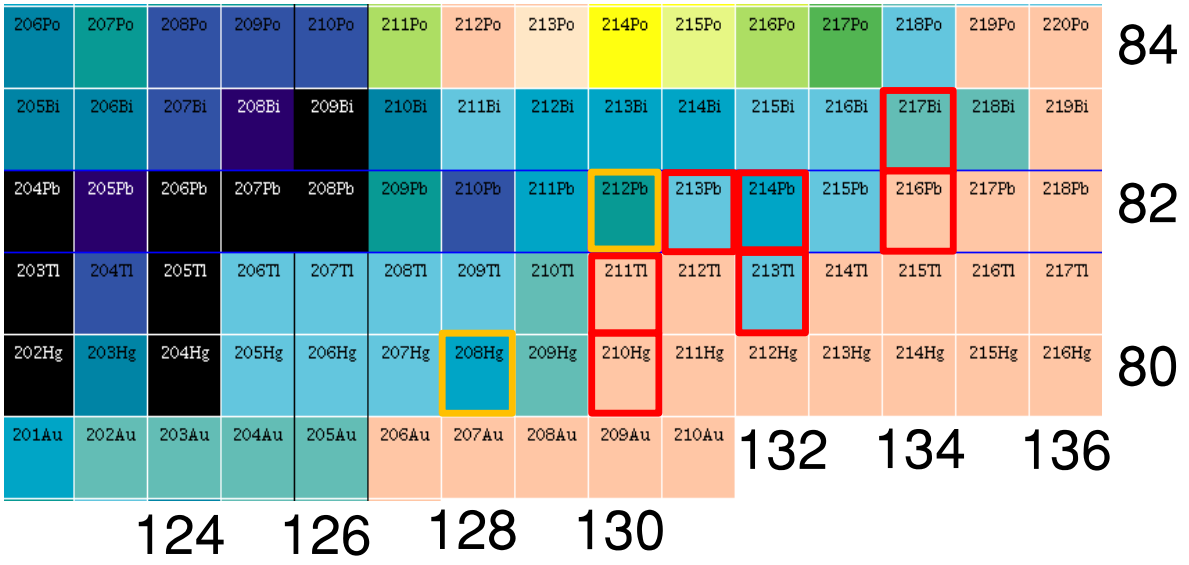

Figure 4.1: Region of interest of the Segré chart. The newly-discovered isomers are indicated in red, while those already observed in orange. The numbers below indicate the number of neutrons, while the number on the right is the atomic number.

than ^{208}Pb, could not be observed in this experiment, since the acceptance of the FRS was set for heavier species. However, this isotope, easier to reach experimentally, has been widely studied in the past [47], and the predicted 8^+ isomer has been observed and measured. Figure 4.2 shows the relevant part of its known level scheme. The half life of the 8^+ isomer is 201 $\pm$ 17 ns [86, 38], the B(E2$\downarrow$) is 47 $\pm$ 4 e^{2}fm^4. As pointed out in Chapter 1, this isomer is a seniority isomer originating from a $(\nu g_{9/2})^2$ configuration. If this scheme is valid, similar 8^+ isomers should be observed in heavier Pb isotopes while filling the $\nu g_{9/2}$ shell.

4.1.1 The nucleus ^{212}Pb

The four valence neutron ^{212}Pb isotope is the less neutron-rich lead ion among the observed ones. As stated in the introduction, the production cross section roughly decreases by an order of magnitude every two neutrons added [42], and thus one would expect that ^{212}Pb is the most populated. However, the mentioned problem regarding the primary beam charge states obliged to reduce the acceptance of the FRS so that the transmission of ^{212}Pb was poor, leading to a final statistics much lower than in $^{214-216}$Pb, and comparable with the one of ^{218}Pb. The resulting γ spectrum from the isomeric decay is shown in Fig. 4.3, obtained with a gate on fully-stripped ions: $\Delta q = 0$. It has to be compared with the previous one reported in Ref. [39], where only two transitions were observed.

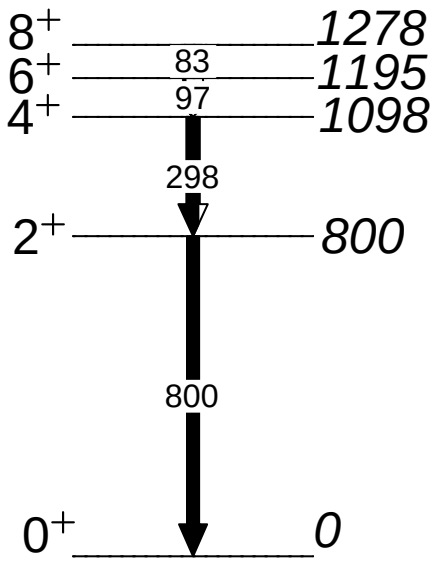

Figure 4.2: Partial level scheme of ^{210}Pb relevant for this work, from Ref. [47]. The arrows represent the observed γ rays. The white part of the arrow is the internal conversion percentage of the transitions. However, the ratio between γ decay and internal conversion has been changed for viewing purposes.

In that experiment the same spectrometer FRS and the same primary beam condition were used. The major improvements with respect to the previous experiment are the higher efficiency of the γ detection array (in that case it was only 1%) and the use of a very thick degrader in S1, to exclude from the acceptance of the FRS the primary beam charge states, which were the main problem in Ref. [39]. In the present case, using a time gate from 120 ns to 26 μs, three transitions are observed to depopulate the isomeric state . Table 4.1 shows their relative intensities corrected for efficiency and electron conversion. They are well compatible within errors, suggesting that they are in coincidence. A $\gamma\gamma$ coincidence matrix has been built and the results of the coincidence analysis are shown in Fig. 4.4: despite the low statistics, the three γ rays detected appear to be in coincidence with each other. For the analysis of coincidences and of intensities the gates $\Delta q = 0, \pm 1$ where used, to increase the statistics. It has been checked that consistent results are obtained with a gate on $\Delta q = 0$: this is also the case for all the following nuclei. These experimental evidences strongly suggest that the observed lines are in coincidence, and, following systematics, the γ lines are attributed to the $6^+ \rightarrow 4^+ \rightarrow 2^+ \rightarrow 0^+$ yrast cascade. The $8^+ \rightarrow 6^+$ transition is not observed. This is due to the low energy of this E2 transition which presents a significant electron conversion branch competing with the γ-ray decay: for lead isotopes the electron conversion coefficient for E2 transitions is

γ energy (keV)	Area	Area corrected
805	48 (8)	316 (53)
316	80 (16)	316 (63)
158	73 (10)	438 (65)

Table 4.1: ^{212}Pb γ-ray intensities corrected for efficiency and electron conversion.

1 already at $\sim$ 150 keV. The transition is assumed to have an energy between 20 and 90 keV, considering that the characteristic K_α X rays from lead at 75 keV are observed with quite low intensity, compatible with its origin only from the $6^+ \rightarrow 4^+$ transition. The upper limit is decided on the basis that the binding energy of K electrons in lead is 88 keV. If the energy of the $8^+ \rightarrow 6^+$ were larger than 90 keV, it would be converted with an internal conversion coefficient $\alpha_K = 10$: as a result, the amount of observed K_α X rays would increase significantly. The lower limit of 20 keV is set considering the lower limit of validity of conversion coefficient tables. However, the exact value of the limits is not very relevant, since below 100 keV, in lead isotopes, the γ transitions are almost all converted and thus their strength is quite insensitive to the precise value of the γ energy, as the energy scaling of the internal conversion coefficient almost counterbalances the scaling E^5 of the B(E2) (see Table 1.1). Actually, for ^{212}Pb, a rough measurement of the energy $8^+ \rightarrow 6^+$ is available from reaction studies [87]: 56$\pm$10 keV, compatible with the present estimate. The deduced level scheme is in Fig. 4.5, and in the next chapter it will be compared to shell-model calculations, which will support the spin-parity assignments made here. The presence of other isomers is excluded within the experimental limits. Figure 4.6 shows the exponential fit to the decay curve of the sum of the 805- and 316-keV transitions, with the resulting half life of 6.0 $\pm$ 0.8 μs. The error has been calculated with the method illustrated in the previous chapter. Considering the conversion coefficient, and the energy of Ref. [87] for the $8^+ \rightarrow 6^+$ transition, the calculated B(E2$\downarrow$) is 1.8 $\pm$ 0.3 e^2fm^4. The error is obtained propagating the errors on lifetime and transition energy.

4.1.2 The nucleus ^{214}Pb

The six valence neutron ^{214}Pb is the most populated even-even neutron-rich lead ion in our experiment. Prior to this experiment no information for its structure was available, except for an α-decay study in Ref. [88], which suggested the existence of an excited level (probably 2^+) at 836 $\pm$ 2 keV. Figure 4.7 shows the γ spectrum resulting from our experiment with time gate of 0.12-26 μs and $\Delta q = 0$: three lines are evident. As in ^{210,212}Pb, according to the seniority scheme, they can be assigned with a great confidence to the cascade $6^+ \rightarrow 4^+ \rightarrow 2^+ \rightarrow 0^+$ from the isomeric 8^+ state. The condition $\Delta q = 0, \pm 1$ was then applied to extract their intensities and to analyse the $\gamma\gamma$ coincidences data. It has been checked that consistent results are obtained with a gate on $\Delta q = 0$.

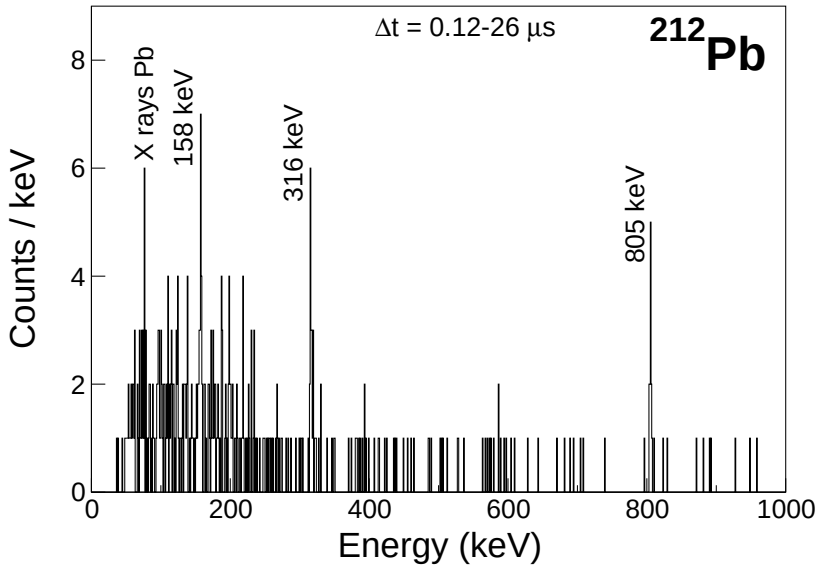

Figure 4.3: Gamma-ray spectrum from the decay of the isomeric state in ^{212}Pb. The spectrum has been obtained by gating on the time window 0.12 - 26 μs.

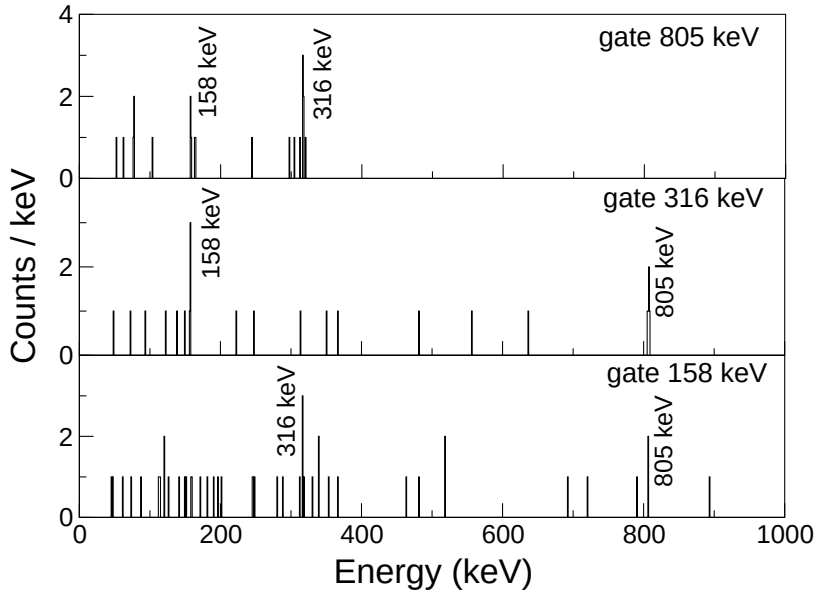

Figure 4.4: Gamma-ray prompt coincidence spectra, with gates on the three transitions following the isomer in ^{212}Pb.

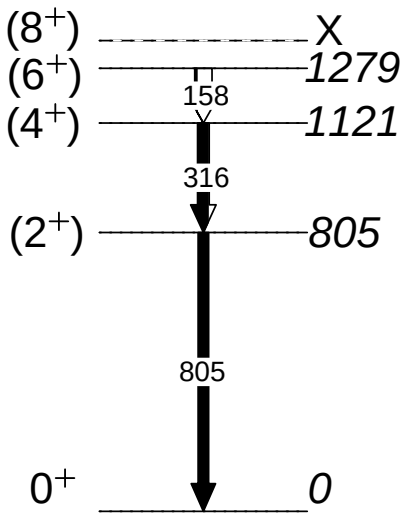

Figure 4.5: Level scheme deduced for ^{212}Pb deduced from this work. The arrows represent the observed γ rays. The white part of the arrow is the internal conversion percentage of the transitions. However, the ratio between γ decay and internal conversion has been changed for viewing purposes.

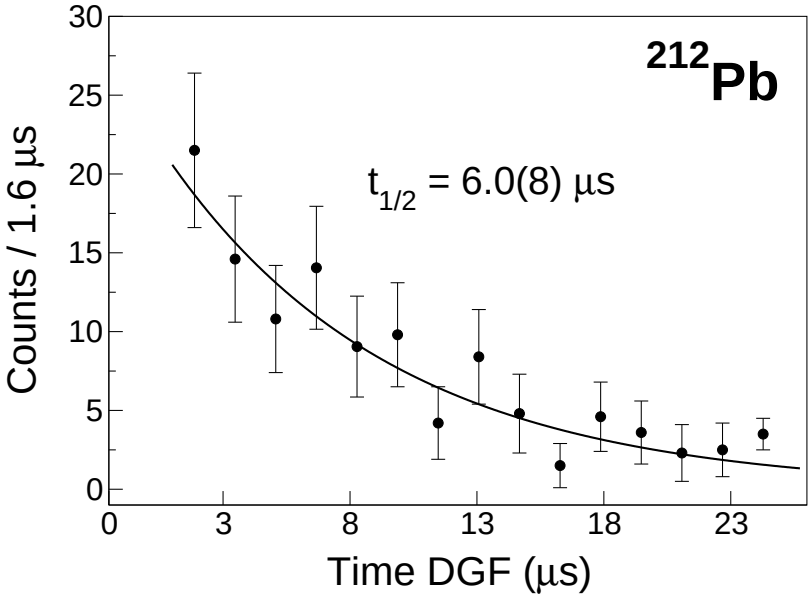

Figure 4.6: Decay curve of the sum of the 316- and 805-keV transitions of ^{212}Pb.

Table 4.2 shows that the transitions have all compatible intensity within the errors, while in Fig. 4.8 the $\gamma\gamma$ coincidences point out that the three lines are clearly in coincidence. The $8^+ \rightarrow 6^+$ transition is not detected, as in ^{212}Pb. Also in this case, this is due to the low energy of this E2 transition. Following the same considerations as in ^{212}Pb, the transition is thus assumed to have an energy between 20 and 80 keV. The upper limit is now set at 80 keV because at this energy, even if K_α X rays are not produced, the intensity of the the $8^+ \rightarrow 6^+$ transition should be above observational limit (> 10 counts)[1]. Figure 4.9 shows the deduced level scheme: a full discussion will be provided in the next chapter. The half life is obtained from an exponential fit to the decay curve of the 835 keV and 344 keV transitions, shown in Fig. 3.18: the value is 6.2 ± 0.3 μs. The B(E2) of the transition strength is calculated considering the limits of the $8^+ \rightarrow 6^+$ energy and the electron conversion coefficient. The B(E2$\downarrow$) ranges from 1.9 ± 0.1 e^{2}fm^4 for $E_\gamma = 20$ keV to 1.6 ± 0.1 e^{2}fm^4 for $E_\gamma = 80$ keV.

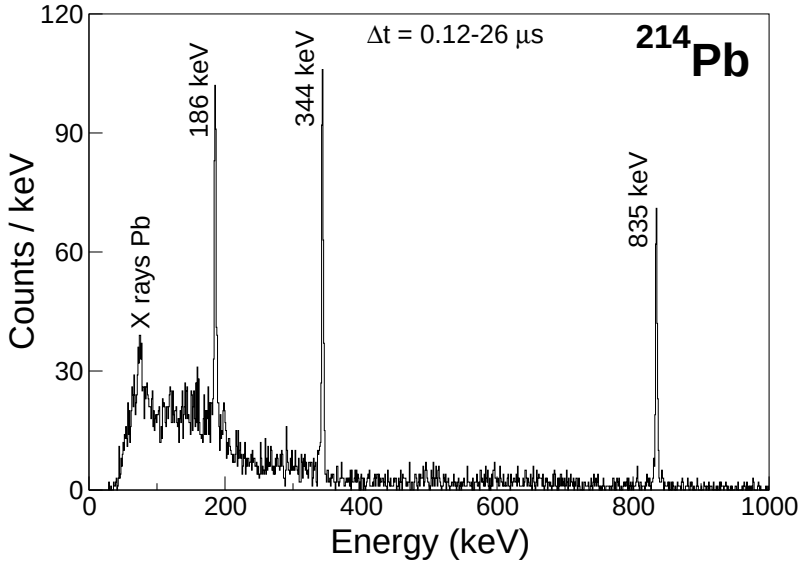

Figure 4.7: Gamma-ray spectrum from the decay of the isomeric state in ^{214}Pb. The spectrum has been obtained by gating on the time window 0.12-26 μs.

[1]The result was obtained considering the electron conversion coefficient and the RISING efficiency at 80 keV

γ energy (keV)	Area	Area corrected
835	244 (28)	1641 (188)
344	394 (51)	1621 (123)
186	340 (44)	1729 (224)

Table 4.2: ^{214}Pb γ-ray intensities corrected for efficiency and electron conversion.

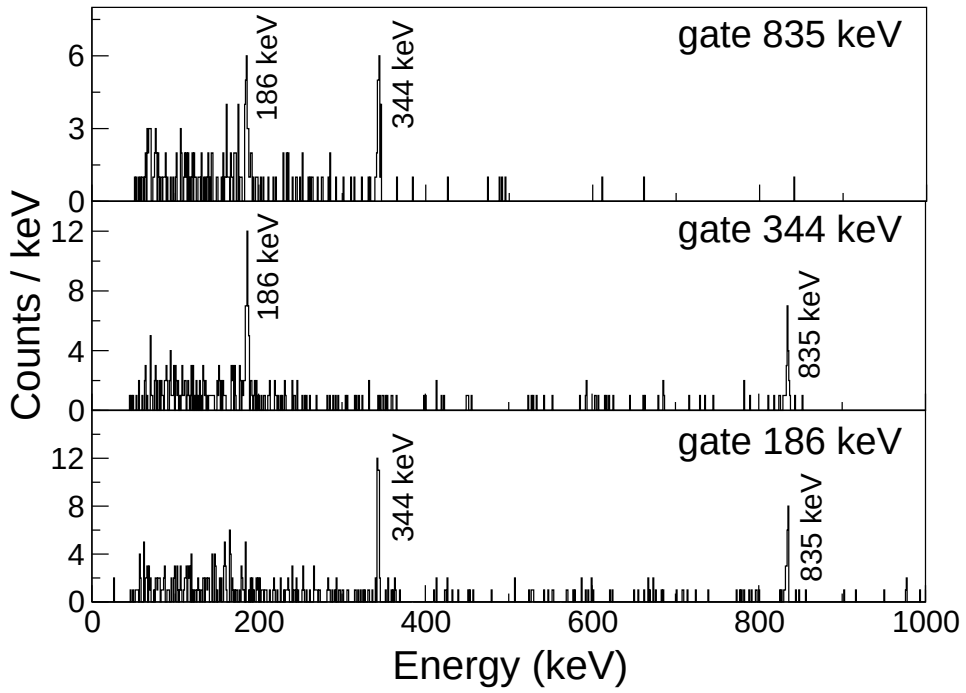

Figure 4.8: Gamma-ray prompt coincidence spectra for the decay from the isomeric state in ^{214}Pb, with gates on the three transitions following the isomer.

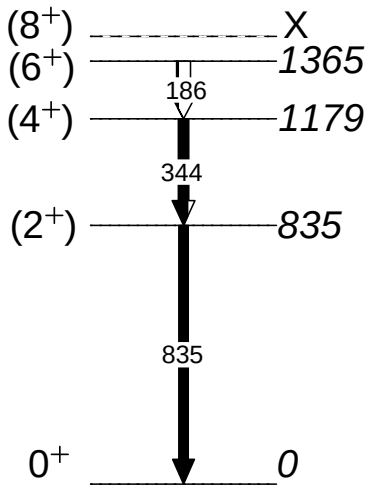

Figure 4.9: Level scheme deduced for ^{214}Pb. The arrows represent the observed γ rays. The white part of the arrow is the internal conversion percentage of the transitions. However, the ratio between γ decay and internal conversion has been changed for viewing purposes.

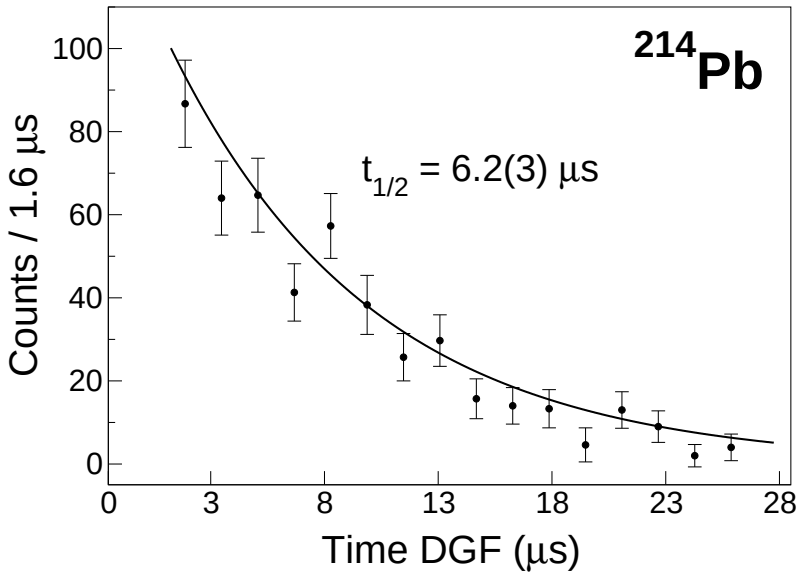

Figure 4.10: Decay curve of the summed time distributions of the 344- and 835-keV transitions in ^{214}Pb.

4.1.3 The nucleus ^{216}Pb

Figure 4.11 shows the γ spectrum obtained by gating on a time window of 0.12 - 3.4 μs after implantation of ^{216}Pb and considering only fully-stripped ions. The three observed transitions are assigned, following the seniority scheme, as in ^{212,214}Pb, to the cascade $6^+ \rightarrow 4^+ \rightarrow 2^+ \rightarrow 0^+$. The $8^+ \rightarrow 6^+$ transition is not detected, as in ^{212,214}Pb, due to its low energy. The $\gamma\gamma$ coincidences shown in Fig. 4.12 and the analysis of transition intensities in Table 4.3 are obtained with a $\Delta q = 0, \pm 1$ gate. It has been checked that consistent results are obtained with a gate on $\Delta q = 0$. They prove that the three γ lines are, respectively, in mutual coincidence and of the same intensity, as expected. The deduced level scheme is presented in Fig. 4.13. The half life is determined using an exponential fit to the decay curve of the sum of the 402- and 887-keV γ rays, see Fig. 4.14, and it is 0.40 $\pm$ 0.04 μs. The B(E2$\downarrow$) for the isomeric $8^+ \rightarrow 6^+$ transition is calculated considering the conversion coefficient and the limits 20-80 keV for the energy, as in ^{214}Pb. The B(E2$\downarrow$) ranges from 30 $\pm$ 3 e^{2}fm^4 for E$_\gamma$ = 20 keV to 24 $\pm$ 2 e^{2}fm^4 for E$_\gamma$ = 80 keV.

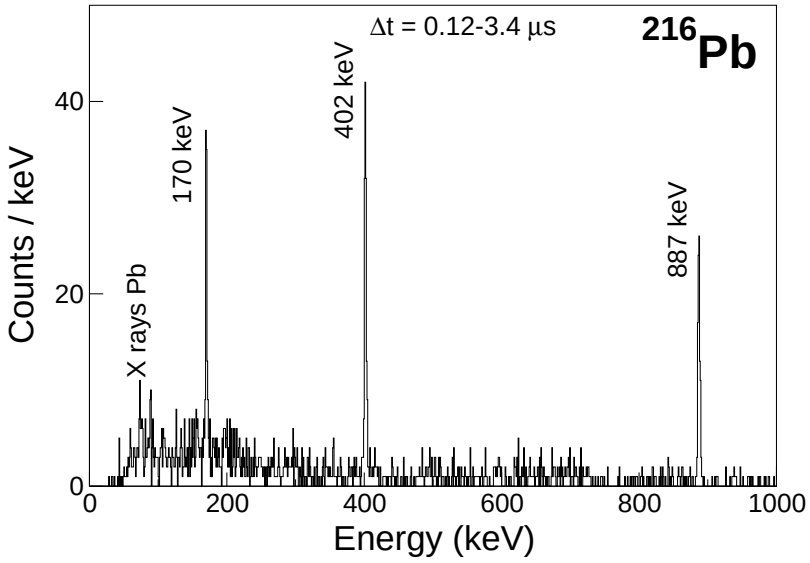

Figure 4.11: Gamma-ray spectrum from the decay of the isomeric state on ^{216}Pb. The spectrum has been obtained by gating on the time window 0.12 - 3.4 μs.

γ energy (keV)	Area	Area corrected
887	86 (11)	601 (77)
402	119 (19)	528 (84)
170	101 (14)	560 (78)

Table 4.3: ^{216}Pb γ-ray intensities corrected for efficiency and electron conversion.

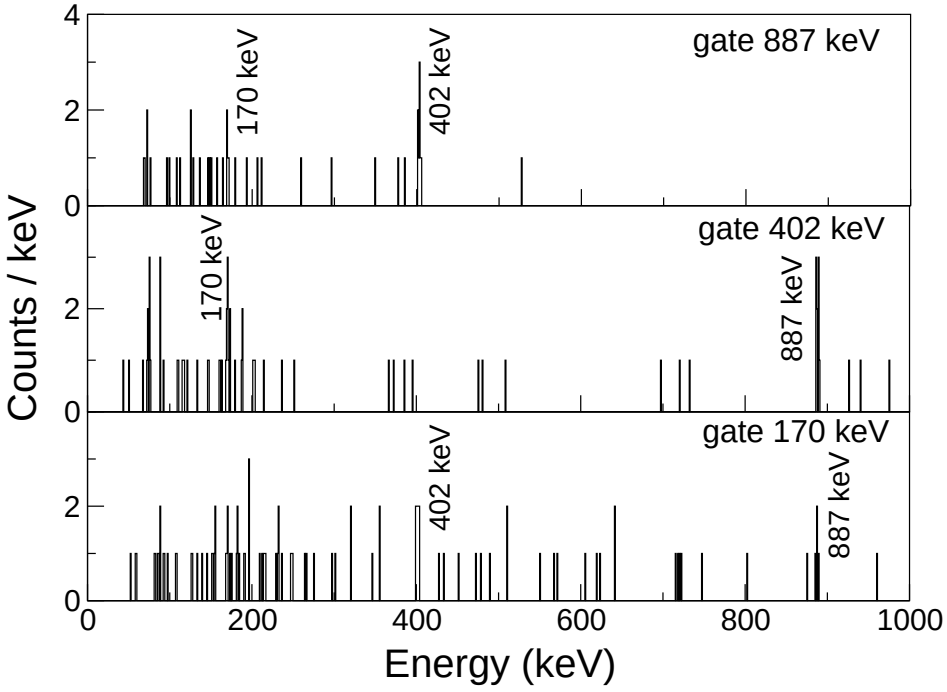

Figure 4.12: Gamma-ray prompt coincidence spectra for the decay from the isomeric state in ^{216}Pb, with gates on the three transitions following the isomer.

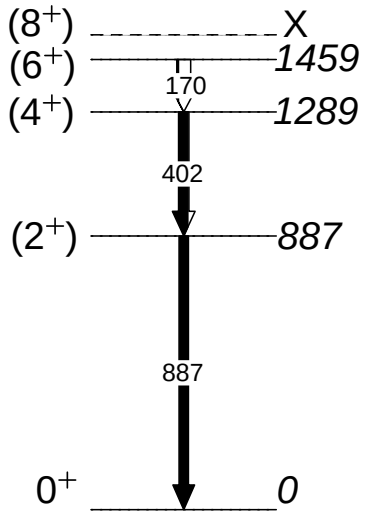

Figure 4.13: Level scheme deduced for ^{216}Pb. The arrows represent the observed γ rays. The white part of the arrow is the internal conversion percentage of the transitions. However, the ratio between γ decay and internal conversion has been changed for viewing purposes.

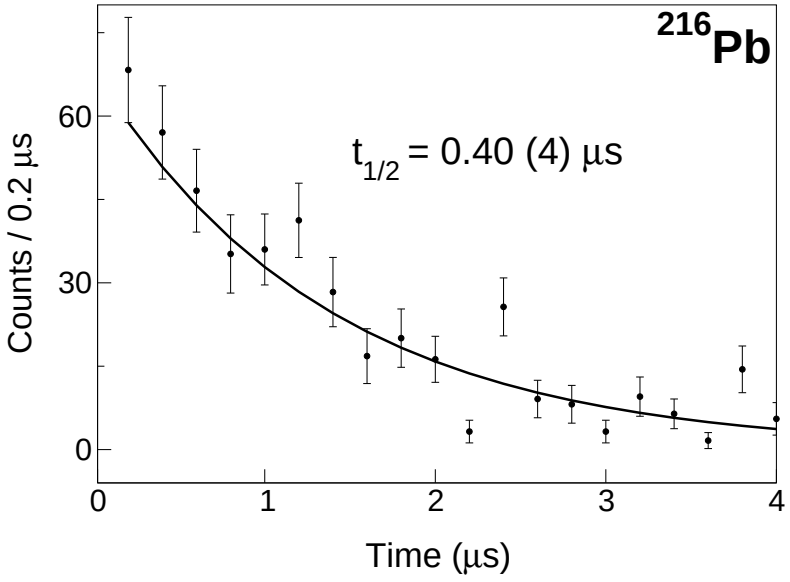

Figure 4.14: Decay curve of the summed time distributions of the 402- and 887-keV transitions in ^{216}Pb.

4.1.4 The nucleus ^{218}Pb

Shell-model calculations, which will be discussed in the next chapter, predict the presence of an 8^+ isomer also for ^{218}Pb, which represents the closure of the $g_{9/2}$ orbit, with a configuration $(g_{9/2})^{10}$. In total, around 800 ^{218}Pb ions were identified. The $4^+ \rightarrow 2^+$ transition would be expected at around 400 keV on the basis of the seniority scheme. It is then possible to establish if it could be detected considering our observational limit. The efficiency of the RISING array is about 20% at 400 keV and considering a 50% population of the isomeric 8^+ state with respect to the total yield of ^{218}Pb ions, one would thus expect to observe such γ ray depopulating the isomer with an intensity of around 40 events. Even with an implantation efficiency as low as 50% (^{218}Pb was at the side of the DSSSD stopper), the transition should be visible. Figure 5.14 shows the time-γ energy matrix for this very exotic lead isotope with the DGF and the short-range time circuits. There is no evidence of an isomeric state, either because it is too short ($\leq$ 10 ns) or too long (ms or more). The upper limit is set considering the total number of ions implanted, an isomeric ratio of 50% and a sensitivity limit of 10 counts to detect a peak. In case of a fully converted $8^+ \rightarrow 6^+$ transition (below $\sim$100 keV, as in the other even-even lead isotopes) this would enable to set a lower and upper limit for the B(E2$\downarrow$): B(E2$\downarrow$)$\geq$1100 e^{2}fm^4 for a lifetime shorter than 10 ns or B(E2$\downarrow$)$\leq$0.003 e^{2}fm^4 for a lifetime longer than 5 ms.

4.2 Odd-even lead isotopes

The odd-even lead isotopes produced and implanted in the present experiment are ^{213,215,217}Pb. ^{211}Pb could not be observed because it was out of the acceptance of the spectrometer which was set to observe more neutron-rich isotopes. The level scheme of ^{211}Pb is well known from Ref. [48], and it is shown in Fig. 4.16. Isomeric levels are observed, in particular the one with spin $21/2^+$ and lifetime 60 ns, which correspond to the seniority isomer $\nu g^3_{9/2}$. The other isomer ($\tau = 230$ ns) originates from a $g^2_{9/2}h^1_{11/2}$ configuration. Assuming the validity of the seniority scheme, a similar structure is expected also in ^{213,125}Pb.

4.2.1 The nucleus ^{213}Pb

^{213}Pb is the only odd-even nucleus where isomeric γ transitions are observed in our experiment. The γ spectrum in Fig. 4.17 is obtained by gating on the time window of 0.12 - 2.2 μs after implantation for fully-stripped ions ($\Delta q = 0$). Two lines, at 772 keV and 488 keV are clearly identified. Two other lines, at 309 keV and 369 keV are also assigned to ^{213}Pb. Table 4.4 shows the relative areas of the peaks. The analysis of $\gamma\gamma$ coincidences, in Fig. 4.18, reveals that the 772 keV and 488 keV transition are in mutual coincidence, while the 309 keV transition seems not to be in coincidence with

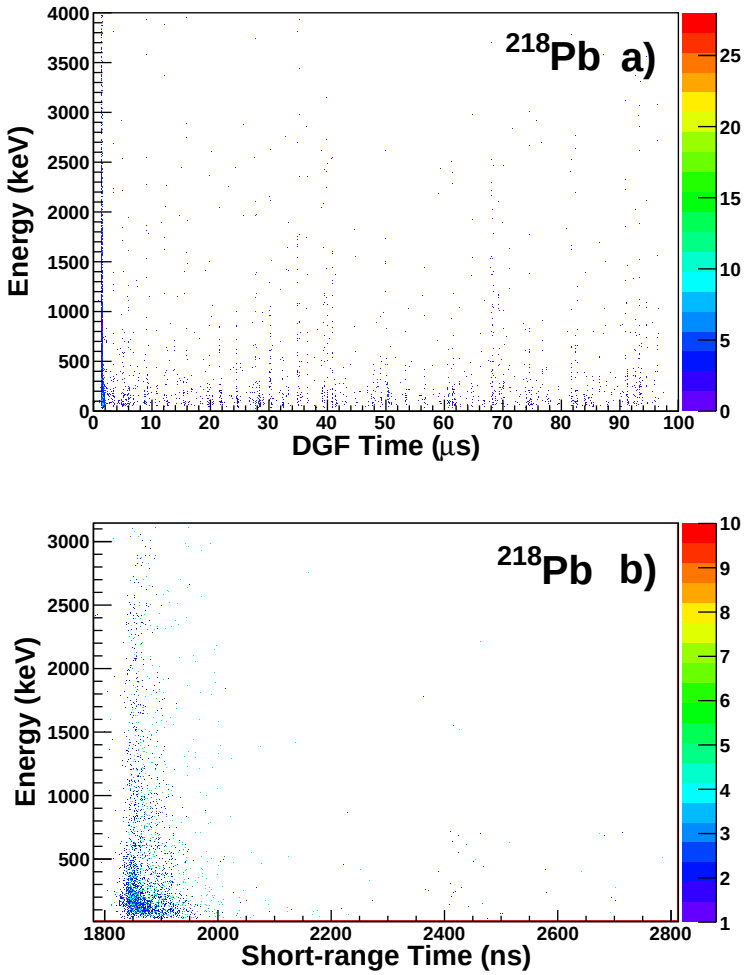

Figure 4.15: a) Time-γ energy spectrum for ^{218}Pb with the DGF circuit; b) Time-γ energy spectrum for ^{218}Pb with the short-range circuit. Both spectra show no presence of isomers in these nuclei.

anything. The 369 keV γ ray seems to have a line in coincidence at 192 keV, but this transition is not clearly visible in the total γ spectrum. Naively, one would expect, similarly to the even-even lead isotopes, the cascade from the seniority isomer (which is also observed in ^{211}Pb): $21/2^+ \rightarrow 17/2^+ \rightarrow 13/2^+ \rightarrow 9/2^+$. The population of the $27/2^+$ isomer is less likely, due to its higher spin. Considering the seniority scheme prediction that the energies should remain almost constant irrespectively of the number of neutrons, the 772 keV could correspond to the $13/2^+ \rightarrow 9/2^+$ transition. A tentative assignment can also be made for the 488 keV line as the $17/2^+ \rightarrow 13/2^+$ transition. This is supported by $\gamma\gamma$ coincidences, but its intensity is incompatible with the one of the

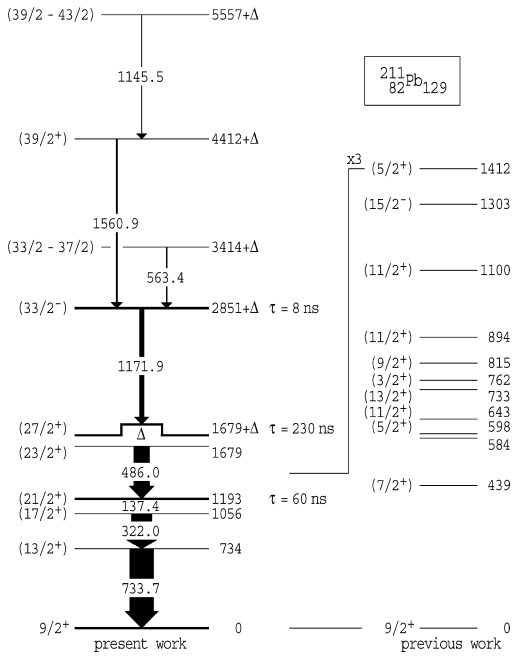

Figure 4.16: ^{211}Pb partial level scheme, showing the two isomers discussed in the text. Figure taken from Ref. [48].

772 keV line, as can be inferred from Table 4.4. Moreover, its energy is 166 keV larger than the corresponding transition in ^{211}Pb, a difference that is not found in even-even lead nuclei. On the contrary, the energy of 488 keV is almost identical to the one of the $23/2^+ \rightarrow 21/2^+$ in ^{211}Pb. However, this assignment is also problematic, as the prompt ($\sim$ 50 ns) coincidence with the 772 keV line would imply a very short lifetime for the seniority isomer. Furthermore, the non observation of the $17/2^+ \rightarrow 13/2^+$ transition in coincidence with the 772 keV line would also be difficult to justify. Figure 4.19 shows the exponential fit to the decay curves of the four γ rays detected. The errors are quite large due to the low statistics. Nevertheless, the 772 keV line seems to have a decay time longer than the other three γ rays. Consequently, the presence of more than one isomer cannot be excluded.Therefore, a level scheme cannot be firmly established.

4.2.2 The nuclei $^{215-217}$Pb

Figures 4.20 and 4.21 shows the time-γ energy matrix with the DGF time circuit: no isomers are observed for ^{215,217}Pb. A similar check with the short-range SR TAC gives a similar result. In ^{215}Pb, following the seniority scheme from ^{211,213}Pb, one would expect to find a short isomeric state with an half life of the order of a hundred ns. The non-observation of this isomer with the present setup, even with the large statistics for the

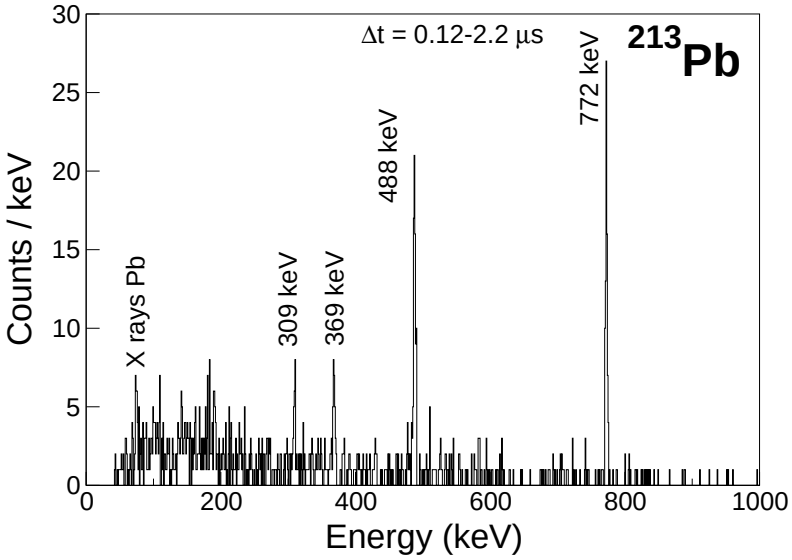

Figure 4.17: Gamma-ray spectrum from the decay of the isomeric state in ^{213}Pb. The spectrum has been obtained by gating on the time window 0.12 - 2.2 μs.

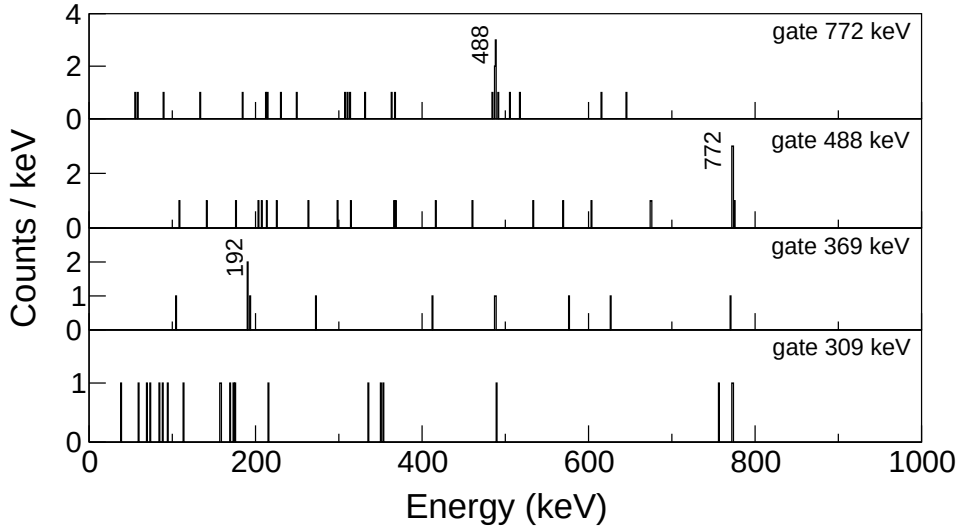

Figure 4.18: Gamma-ray prompt coincidence spectra for the decay from the isomeric state(s) in ^{213}Pb, with gates on the four transitions following the isomer(s).

implanted ^{215}Pb ions, implies a lifetime shorter than 10 ns as explained in the previous chapter. In principle, a too long lifetime, around ms or more, would be compatible with

γ energy (keV)	Area	Area corrected
772	105 (11)	672 (70)
488	90 (10)	442 (49)
369	52 (11)	221 (47)
309	43 (7)	168 (27)

Table 4.4: ^{213}Pb γ-ray intensities corrected for efficiency and electron conversion.

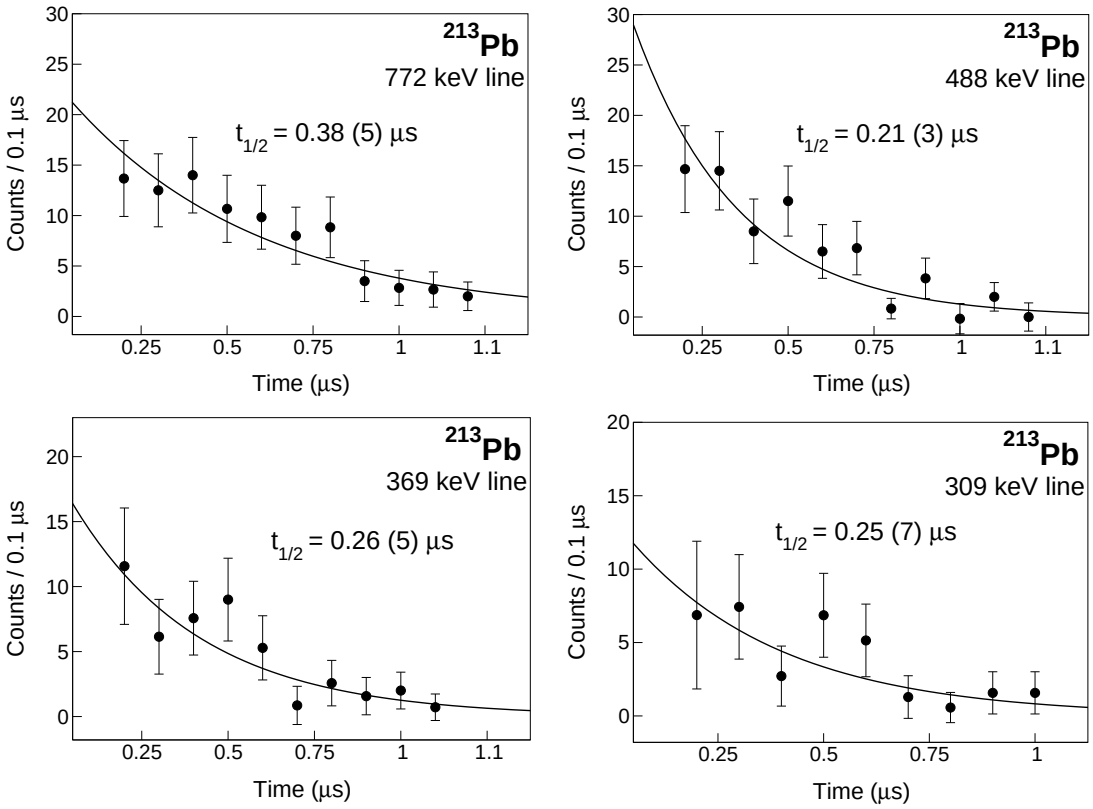

Figure 4.19: Time distribution curves for the four γ rays observed in ^{213}Pb.

the experiment, but less likely, as the seniority scheme predicts a lifetime close to the one of ^{211}Pb (60 ns). In case of a fully converted transition (below ∼100 keV) this would enable to set a lower limit for the B(E2): B(E2↓)≥1100 e^2fm^4. If the energy of the transitions is higher, it is less converted and thus the B(E2) could become smaller, as proved by Eq. 1.11.

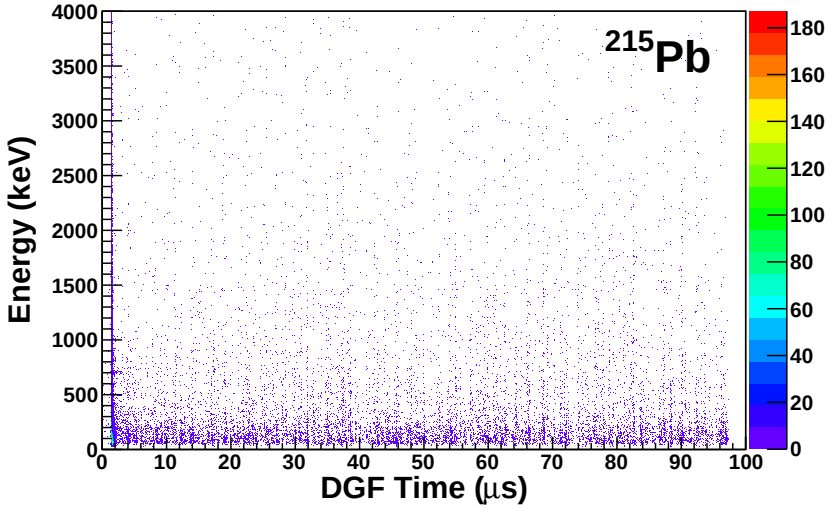

Figure 4.20: Time-γ energy spectrum for ^{215}Pb with the DGF circuit, showing that no isomer is present.

4.3 Bismuth isotopes

The odd-even bismuth isotopes are an interesting case to study, as their structure should be the result of the coupling of the unpaired proton above the Z = 82 core with the excited states of the even-even lead nuclei. Since the lower proton orbit outside the closed core is $h_{9/2}$, one expects to observe a $\pi h_{9/2} \otimes \nu 8^+$ isomer with spin $25/2^-$, and then the γ-ray cascade to the states resulting from the couplings $\pi h_{9/2} \otimes \nu 6^+ \rightarrow \pi h_{9/2} \otimes \nu 4^+ \rightarrow \pi h_{9/2} \otimes \nu 2^+ \rightarrow \pi h_{9/2} \otimes \nu 0^+$, i.e., the sequence: $25/2^- \rightarrow 21/2^- \rightarrow 17/2^- \rightarrow 13/2^- \rightarrow 9/2^-$. The transition depopulating the isomeric state, $25/2^- \rightarrow 21/2^-$, may not be detected since it is expected to be strongly converted due to its low energy, as in the lead isotopes. Such a seniority isomer has been observed only in ^{211}Bi. In fact, ^{213}Bi [89] has been only scarcely studied and the isomer measured in ^{215}Bi [49] is not a seniority isomer, but it originates from an inversion of the $27/2^-$ or $29/2^-$ levels with the $25/2^-$ level. In any case, this isomer cannot be observed because its half life is 36.9 s, well above the observational limit of our setup (around 10 ms).

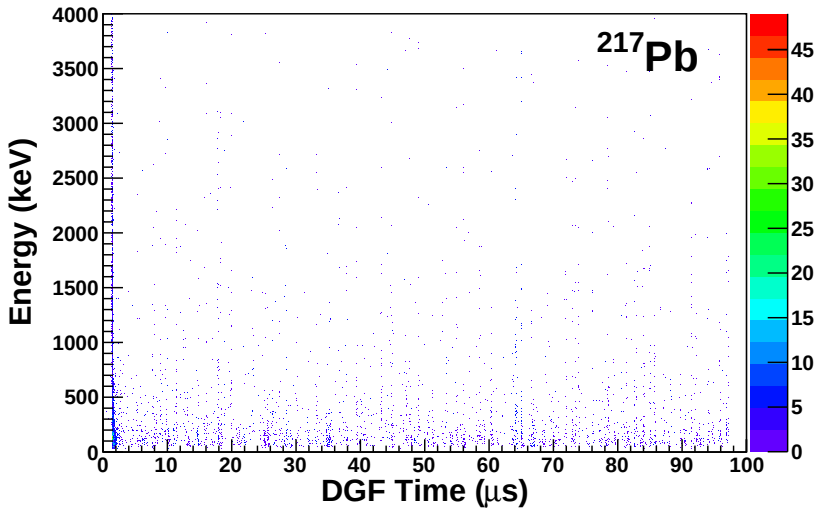

Figure 4.21: Time-γ energy spectrum for ^{217}Pb with the DGF circuit, showing that no isomer is present.

4.3.1 The nucleus ^{217}Bi

The nucleus ^{217}Bi is the only Bi isotope for which an isomer is observed. Figure 4.22 shows the γ spectrum obtained with a time gate 0.12 - 15 μs. Three γ rays are clearly present, while the nature of the smaller two peaks labeled with an asterisk is not clear. Figure 4.23 and Table 4.5 prove that the three observed lines are in mutual coincidence and of comparable intensity, respectively. Therefore, also considering the systematics from the lighter isotopes, the γ rays are attributed to the cascade $21/2^- \rightarrow 17/2^- \rightarrow 13/2^- \rightarrow 9/2^-$. The isomeric state would thus be $25/2^-$, with the $25/2^- \rightarrow 21/2^-$ transition not observed due to its low energy. The deduced level scheme is in Fig. 4.24. The decay curve of the sum of the 743- and 491-keV γ lines is fitted with an exponential function to extract the isomer half life of 2.70 $\pm$ 0.06 μs: see Fig. 4.25. The B(E2$\downarrow$) for the isomeric $25/2^- \rightarrow 21/2^-$ transition is calculated considering the conversion coefficient and the limits 20-80 keV for its energy: it ranges from 5.2 $\pm$ 0.1 e^{2}fm^4 for E$_\gamma$ = 20 keV to 3.6 $\pm$ 0.1 e^{2}fm^4 for E$_\gamma$ = 80 keV.

γ energy (keV)	Area	Area corrected
743	275 (36)	1720 (194)
491	308 (36)	1518 (177)
199	426 (33)	2083 (161)

Table 4.5: ^{217}Bi γ-ray intensities corrected for efficiency and electron conversion.

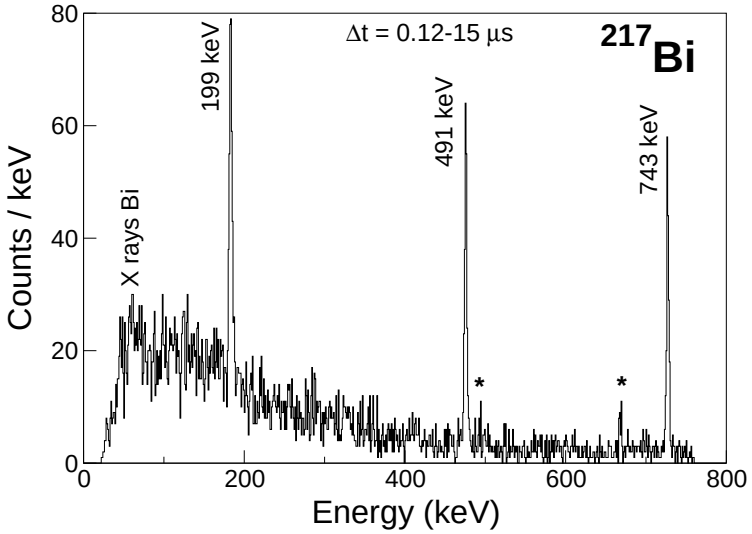

Figure 4.22: Gamma-ray spectrum from the decay of the isomeric state in ^{217}Bi. The spectrum has been obtained by gating on the time window 0.12 - 15 μs.

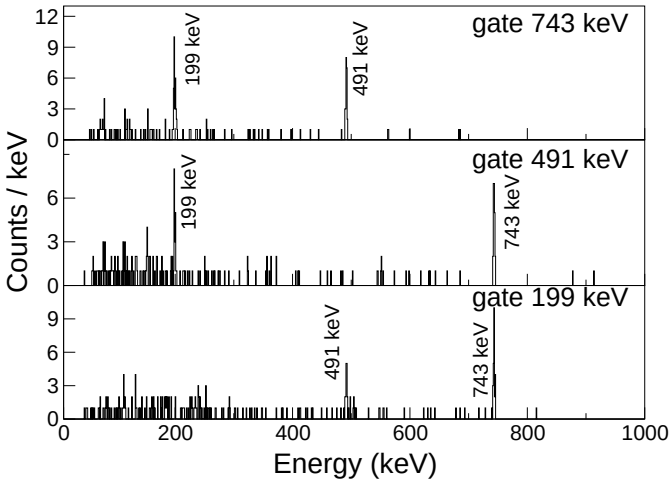

Figure 4.23: Gamma-ray prompt coincidence spectra for the decay from the isomeric state in ^{217}Bi, with gates on the three transitions following the isomer.

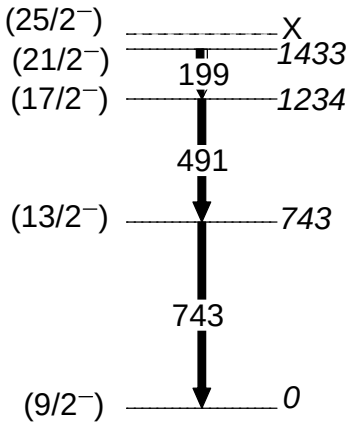

Figure 4.24: Level scheme proposed for ^{217}Bi. The arrows represent the observed γ rays. The white part of the arrow is the internal conversion percentage of the transitions. However, the ratio between γ decay and internal conversion has been changed for viewing purposes.

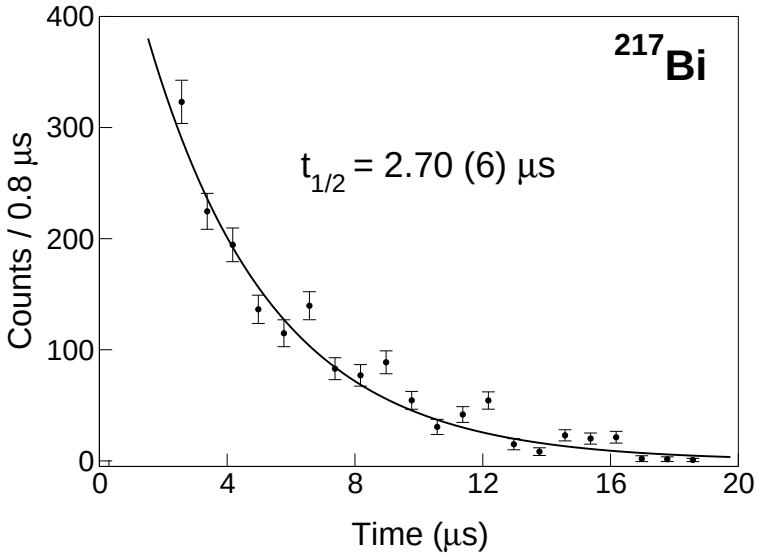

Figure 4.25: Summed time-distribution of the 491- and 743-keV transitions in ^{217}Bi.

4.4 Thallium isotopes

The thallium isotopes beyond N = 126 were first studied in Ref. [50], were one isomer was observed in ^{209}Tl. In the present experiment this nucleus was outside the acceptance of the spectrometer, but in Fig. 4.26 the spectrum obtained in Ref. [50] is reported, to be compared later with the heavier thallium fragments from our study (the isomer decay of ^{208}Hg is also in the figure and we will deal with it later). The transitions in the spectrum were attributed to the decay of an isomer with half life of 95 ± 11 ns. Spin-parity $17/2^+$ was assigned to the isomer, with a suggested $\nu(g_{9/2})^2_{8+}\pi s_{1/2}$ configuration, as shown in the level scheme of Fig. 4.27 where also shell-model calculations are presented. The decay cascade was then interpreted as $17/2^+ \rightarrow 13/2^+ \rightarrow 9/2^+ \rightarrow 7/2^+ \rightarrow 3/2^+ \rightarrow 1/2^+$, where the $17/2^+ \rightarrow 13/2^+$ E2 and the $9/2^+ \rightarrow 7/2^+$ M1 transitions were not observed because fully converted due to their low energy. The shell-model calculations will be discussed in the next chapter. This level scheme will be used as a guidance for interpretation of the observed isomeric decays in the odd-even ^{211,213}Tl. In fact, from the systematics and the seniority scheme, one would expect that ^{211,213}Tl will also have a $17/2^+$ isomer. Therefore, their structure should correspond to the coupling of the corresponding even-even lead isotope neutron levels with the hole in $s_{1/2}$ below the Z = 82 core. However, these predictions will not prove to be completely correct.

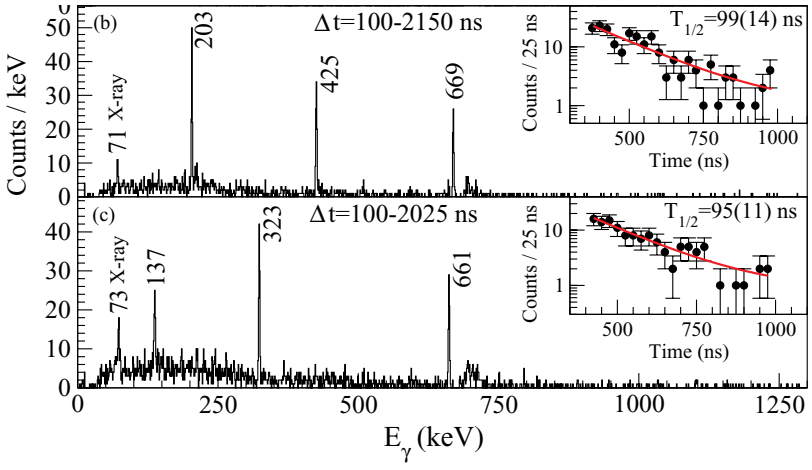

Figure 4.26: ^{208}Hg (above) and ^{209}Tl (below) γ-ray spectra from the decay of the isomeric states. The spectra have been obtained by gating on the time windows indicated in the picture, which is taken from Ref. [50].

4.4.1 The nucleus ^{211}Tl

Figure 4.28 shows the γ-ray spectrum obtained for ^{211}Tl with a time gate 0.12 - 3 μs. One transition at 144 keV dominates the spectrum. The 144 keV γ ray is not in coincidence

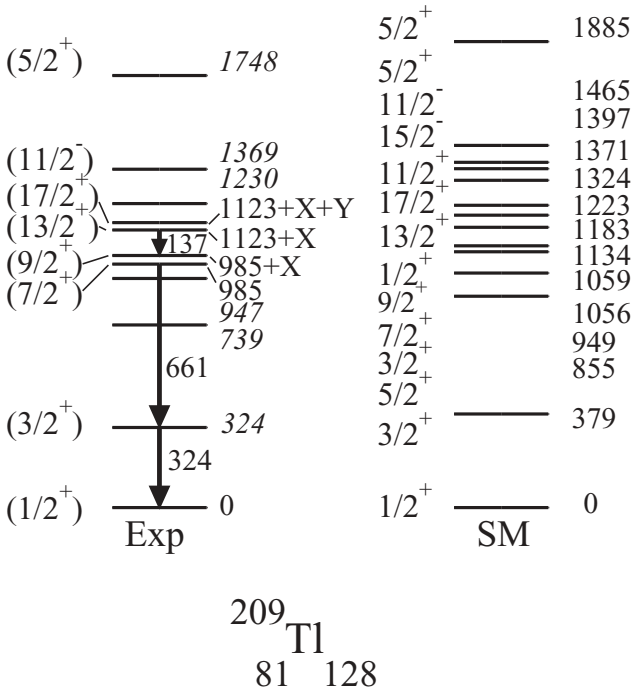

Figure 4.27: ^{209}Tl experimental and calculated levels. Picture taken from Ref. [50].

γ energy (keV)	Area	Area corrected
144	227 (31)	431 (57)

Table 4.6: ^{211}Tl 144 keV γ-ray intensity corrected for efficiency and electron conversion.

with other transitions, as shown in Fig. 4.29. Table 4.6 reports the area ot the 144 keV transition with the associated error. The time distribution of the γ ray was fitted with an exponential curve, see Fig. 4.30, to derive an half life of 0.58 $\pm$ 0.03 μs. Apparently, the spectrum in Fig. 4.28 is different from what was observed in ^{209}Tl. In the next chapter an interpretation of the structure of ^{211}Tl will be provided by comparing the data with the same shell-model calculation which has proved successful in reproducing ^{209}Tl. We will assume that the observed γ ray belongs to the γ cascade depopulating a $17/2^+$ isomer. If, as in ^{209}Tl, the non-detected $17/2^+ \rightarrow 13/2^+$ transition is highly converted, the B(E2$\downarrow$) is calculated to range from 35 $\pm$ 2 e^{2}fm^4 for E$_\gamma$ = 20 keV to 24 $\pm$ 1 e^{2}fm^4 for E$_\gamma$ = 80 keV.

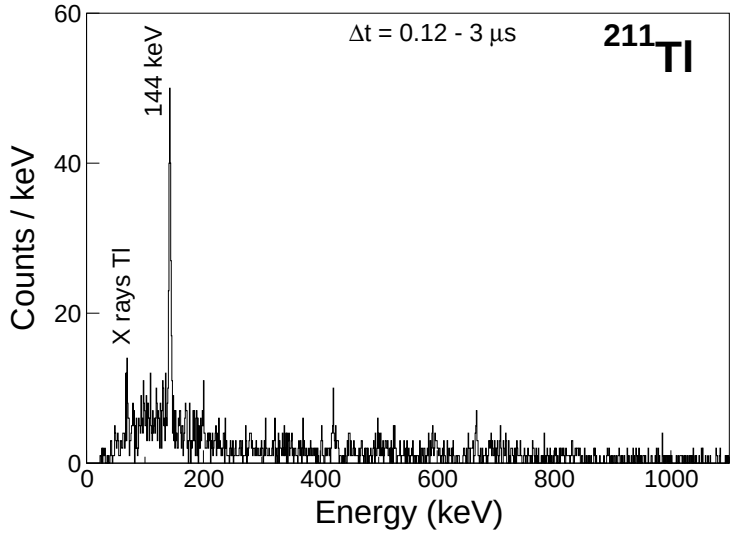

Figure 4.28: Gamma-ray spectrum from the decay of the isomeric state in ^{211}Tl. The spectrum has been obtained by gating on the time window 0.12 - 3 μs

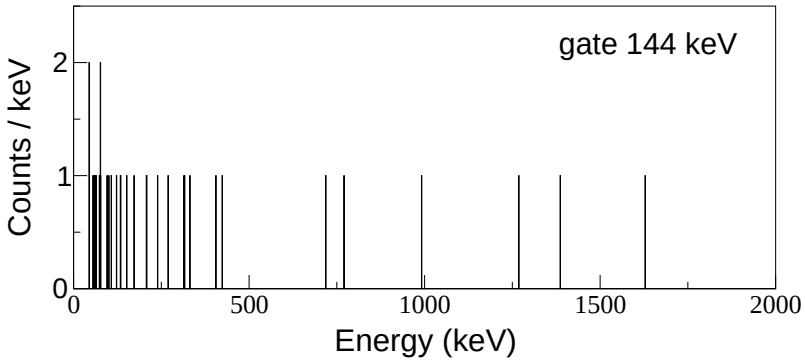

Figure 4.29: Gamma-ray prompt coincidence spectrum for the decay from the isomeric state in ^{211}Tl, with gate on the 144-keV transition.

4.4.2 The nucleus ^{213}Tl

Figure 4.31 shows the γ-ray spectrum obtained for ^{213}Tl with a gate 0.12 - 20 μs: two transitions appear, at 380 keV and 698 keV. Fig. 4.32 shows that the two γ rays are not in coincidence. Table 4.7 reports the areas of the two γ lines. The time distributions of the γ-rays were fitted with an exponential curve, see Fig. 4.33 and Fig. 4.34, to calculate

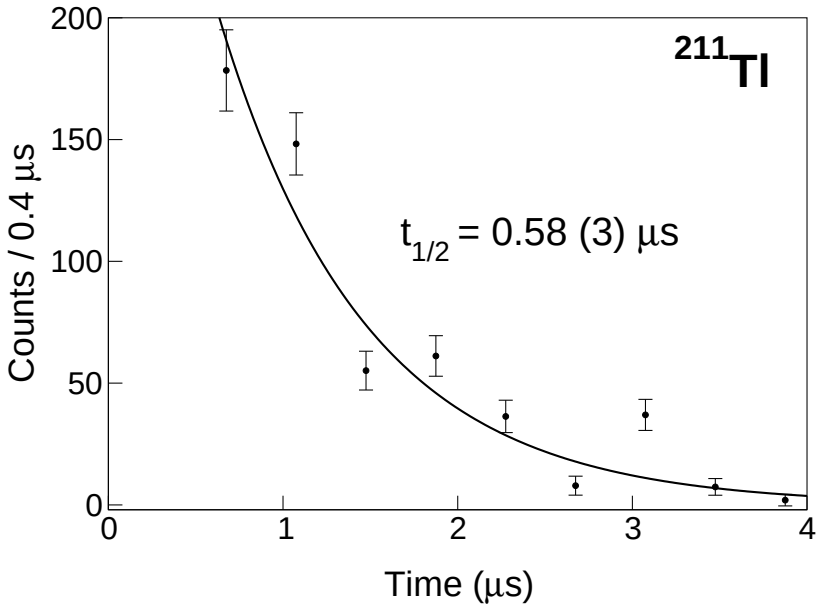

Figure 4.30: Time distribution for the 144-keV transition in ^{211}Tl.

γ energy (keV)	Area	Area corrected
380	91 (11)	392 (47)
698	17 (5)	102 (30)

Table 4.7: ^{213}Tl γ-ray intensities corrected for efficiency and electron conversion.

an half life of 4.1 $\pm$ 0.4 μs for the 380 keV line and of 0.2 $\pm$ 0.05 μs for the 698 keV γ ray. They are not compatible, possibly indicating the existence of two isomers. The spectrum in Fig. 4.31 is very different from what was observed in ^{209}Tl and also from ^{211}Tl. The low statistics of the 698 keV line may also imply that it comes as a contamination from another nucleus, even if the $\Delta q = 0$ gate was set. In the next chapter an interpretation of the structure of ^{213}Tl will be attempted by comparing the data with shell-model calculations, but it is anyhow already evident that the simplistic view based on the seniority scheme is not correct for the thallium isotopes.

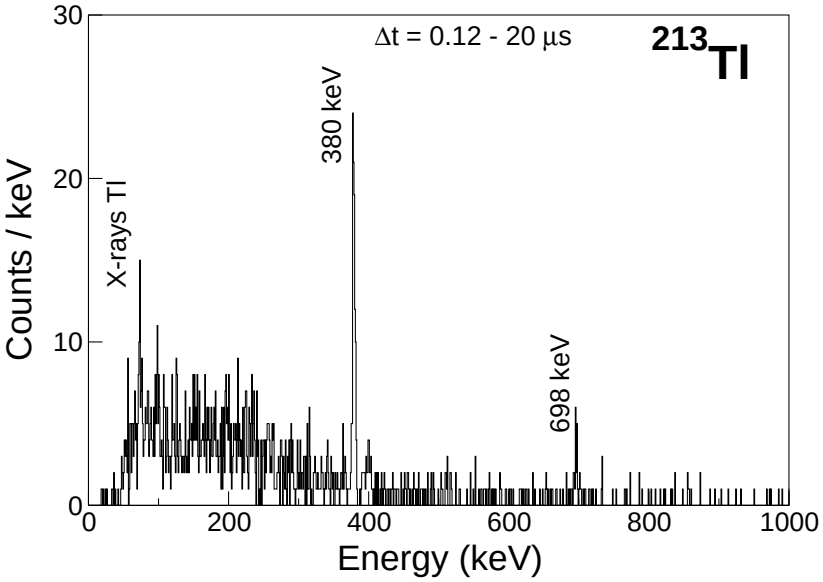

Figure 4.31: Gamma-ray spectrum from the decay of the isomeric state in ^{213}Tl. The spectrum has been obtained by gating on the time window 0.12 - 20 μs.

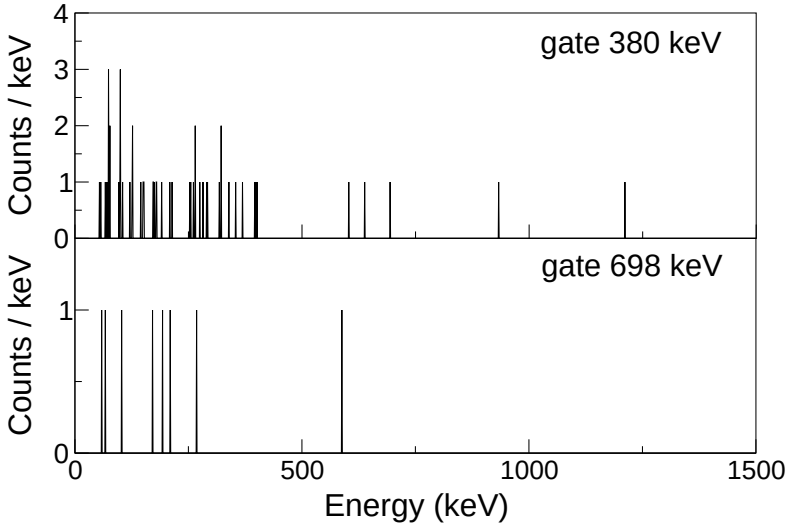

Figure 4.32: Gamma-ray prompt coincidence spectra for the decays from the isomeric state in ^{213}Tl, with gates on the two transitions following the isomers.

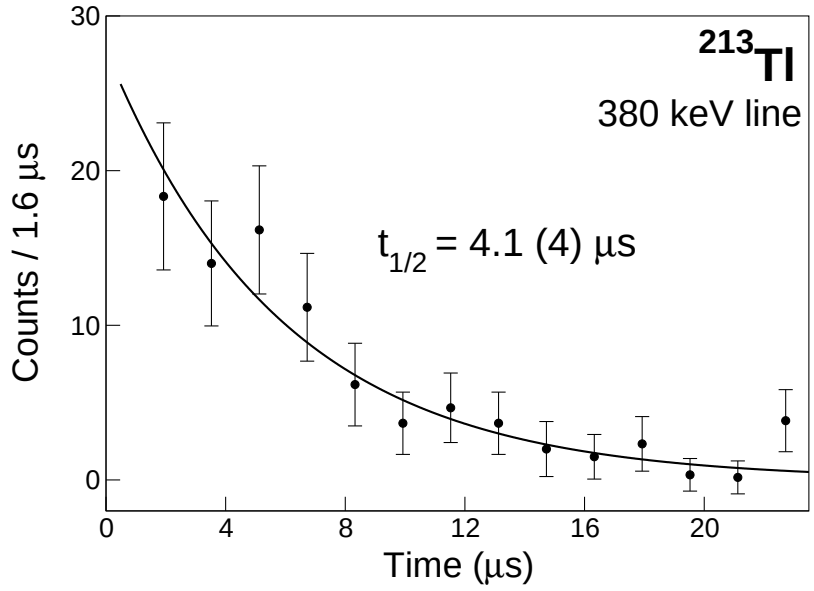

Figure 4.33: Time distribution of the 380-keV transition in ^{213}Tl.

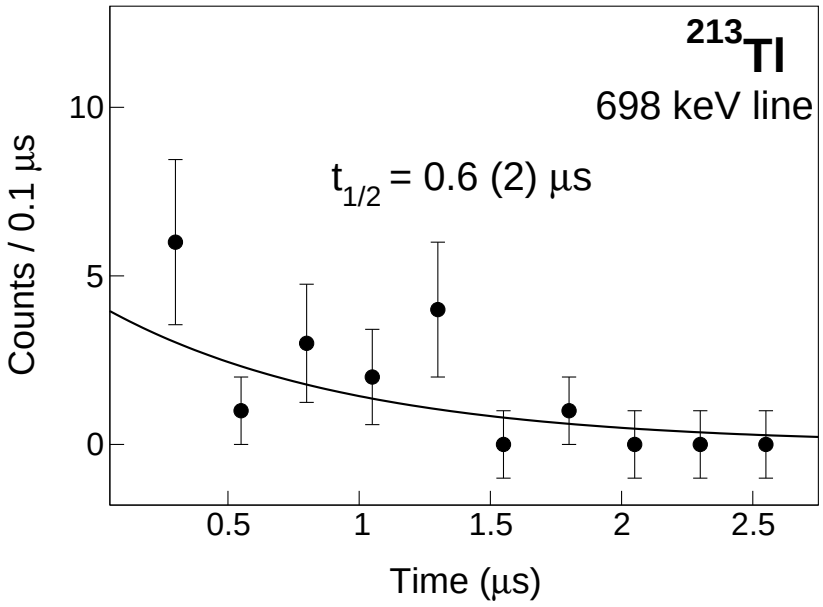

Figure 4.34: Time distribution of the 698-keV transition in ^{213}Tl.

4.5 Mercury isotopes

In the FRS settings the Hg isotope transmission was not optimized, since the main concern was the production of neutron-rich Pb isotopes. Nevertheless, they were implanted in the DSSSD detector and studied in some detail. The even-even mercury isotopes above N = 126 and with two proton holes with respect to the Z = 82 core should present a structure where the excited states result from the coupling of the corresponding states of lead with the two proton holes. ^{208}Hg was for the first time studied in Ref. [50] where an isomeric state, with a half life of 99 ±14 ns, was measured. The γ spectrum observed in Ref. [50] was already shown in Fig. 4.26. The isomer was interpreted as the 8^+ state and the sequence of γ rays is similar to the one in the even-even lead isotopes, see Fig. 4.35 where the experimental levels are also compared to shell-model calculations. It is therefore reasonable to assume the validity of the seniority scheme in $(g_{9/2})^n$ configuration for the even-even mercury isotopes. On the contrary, ^{210}Hg – two proton holes with respect to ^{212}Pb – will show a significant deviation from this expectation.

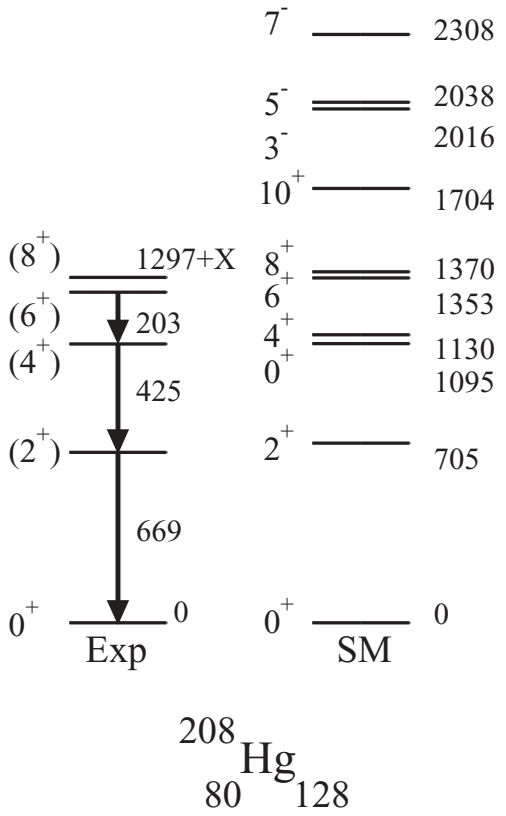

Figure 4.35: ^{208}Hg experimental and calculated levels. Picture taken from Ref. [50].

4.5.1 The nucleus ^{208}Hg

As stated above, ^{208}Hg was already studied in Ref. [50], with the same experimental setup used for the present experiment, but different FRS settings. The results presented here for ^{208}Hg serve thus as a consistency test for the data analysis procedure employed. Figure 4.36 presents the γ-ray spectrum obtained with a time window of 0.1 - 0.5 μs. The spectrum can be directly compared to the one in Fig. 4.26: they are almost identical, but the statistics in the previous experiment was larger because the transmission through the FRS was higher for this isotope in that FRS setting. Table 4.8 points out that the three lines observed are of comparable intensity, confirming the level scheme in Fig. 4.35. The decay curve of the two transitions at 425 keV and 669 keV has been fitted with an exponential function. Since the lifetime is very short, around 100 ns, both the DGF and the short-range SR time circuits were used. Figure 4.37 shows the fit with the SR TAC, which yields an half life of 113 $\pm$ 5 ns. The same fit performed with the DGF time circuit gives the very compatible value of 117 $\pm$ 6 ns. These results are perfectly consistent with the one (99 $\pm$ 14 ns) in Ref. [50]. As a consequence, our B(E2$\downarrow$) value is almost identical to the one already calculated in that paper, ranging from 199 $\pm$ 8 e^{2}fm^4 for E_γ = 20 keV to 161 $\pm$ 6 e^{2}fm^4 for E_γ = 80 keV.

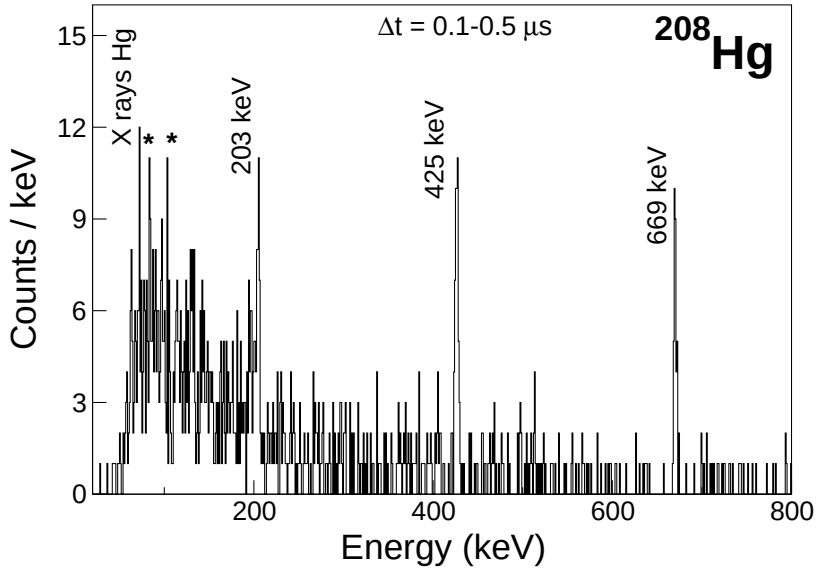

Figure 4.36: ^{208}Hg γ-ray spectrum from the decay of the isomeric state. The spectrum has been obtained by gating on the time window 0.1 - 0.5 μs.

γ energy (keV)	Area	Area corrected
669	61 (12)	358 (71)
425	74 (21)	339 (96)
203	73 (28)	341 (133)

Table 4.8: ^{208}Hg γ-ray intensities corrected for efficiency and electron conversion.

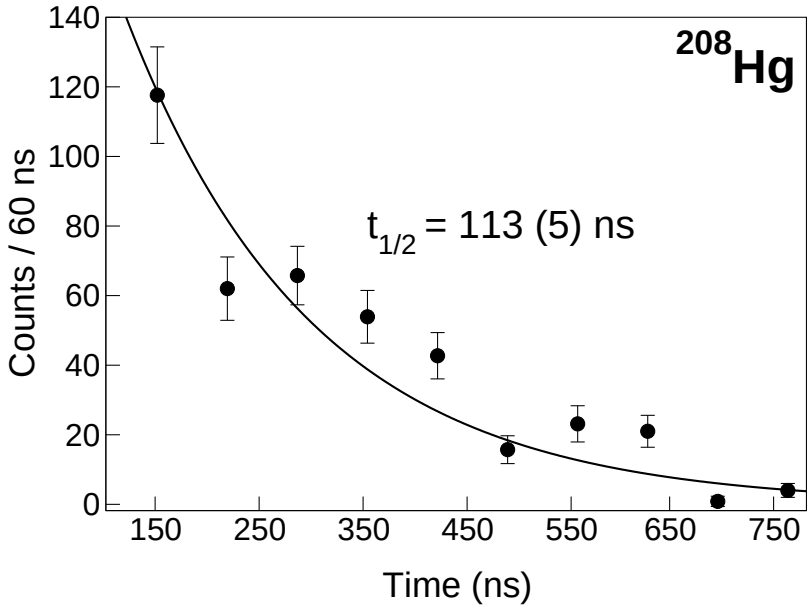

Figure 4.37: Summed time distribution of the 425- and 669-keV transitions in ^{208}Hg. The short-range time circuit has been used, due to the short half life of the isomer.

4.5.2 The nucleus ^{210}Hg

The nucleus ^{210}Hg was populated with much lower statistics with respect to ^{208}Hg, but isomeric states are nonetheless clearly identified. A somehow naïve or simplistic expectation based on systematics from even-even lead isotopes would be to observe the same 8^+ seniority isomer as in ^{208}Hg. Figure 4.38 shows the γ spectrum obtained by gating on the time window of 0.1 - 5 μs after implantation, with the $\Delta q = 0$ condition applied. Four peaks clearly appear in the spectrum, while other lines are visible, but they are too weak and compatible with background fluctuations. The spectrum is quite different from the one of ^{208}Hg, and its understanding demands a more careful analysis. The $\gamma\gamma$ coincidence matrix in Fig. 4.39 provide important indications for building a level scheme for ^{210}Hg. The 643- and 553-keV lines are in mutual coincidence and another line at 170 keV emerges from the background when the coincidence condition is applied. These three transitions could be, as a first guess, attributed to the cascade from the predicted

γ energy (keV)	Area	Area corrected
553	12 (4)	12 (4)
643	45 (7)	49 (8)
663	25 (6)	28 (7)
170	13 (7)	13 (7)

Table 4.9: ^{210}Hg γ-ray intensities corrected for efficiency and electron conversion.

8^+ isomer, where the $8^+ \rightarrow 6^+$ transition is fully converted due to its low energy. This simplistic idea is not confirmed by the analysis of γ-ray intensities in Table 4.9. In fact, while the intensities of the 553- and-170 keV transitions are compatible, the 643-keV line has an intensity which is much larger. On the other side, the 663-keV γ ray present in Fig. 4.38 is not in coincidence with the others (see Fig. 4.39). Figure 4.40 shows the exponential fit to the decay curves of the three most intense lines, since the transition at 170 keV has too low statistics to derive a decay time. The measured half lives are compatible within their large errors. On this basis, also considering systematics and the seniority-scheme prediction, the 170-, 553- and 643-keV transitions are attributed to the cascade $6^+ \rightarrow 4^+ \rightarrow 2^+ \rightarrow 0^+$, respectively, from the decaying 8^+ isomeric state, see Fig. 4.41. The intensity analysis has however shown that there must be a transition feeding the 2^+ level at 643 keV, of intensity compatible with the feeding from the isomeric state decay. This transition is not observed in the γ spectra and has thus to be low in energy, below 150 keV for an E2 transition, considering the intensity, the conversion coefficient and a sensitivity limit of 10 counts to detect a transition. It could also be above 4 MeV, out of the range of the γ-ray array. The γ ray at 663 keV, which is not in coincidence with other lines, is also problematic to place in the level scheme. A possibility is to link this state to the unobserved strength feeding the 643 keV γ ray, thereby suggesting the level scheme of Fig. 4.41. The nature of the state at 663 keV will be discussed in more detail in the next chapter, but it is reasonable to think that it could correspond or to a 3^- state, decaying to the ground state with an E3 transition (the lifetime of $\sim 1\mu$s is typical of such multipole), or a quite suppressed E2 transition. This state at 663 keV is 20 keV above the first 2^+, and would also have a decay branch to it. This γ ray of 20 keV would be totally converted and thus not observed in any case, and its multipolarity could be E1 or M1 according to the 663 keV state being a 3^- or a 2^+, respectively. The lifetime of this branching has to be ~ 1 μs, since the lifetime of $4^+ \rightarrow 2^+$ and $2^+ \rightarrow 0^+$ transitions are both $\sim 1\mu$s.

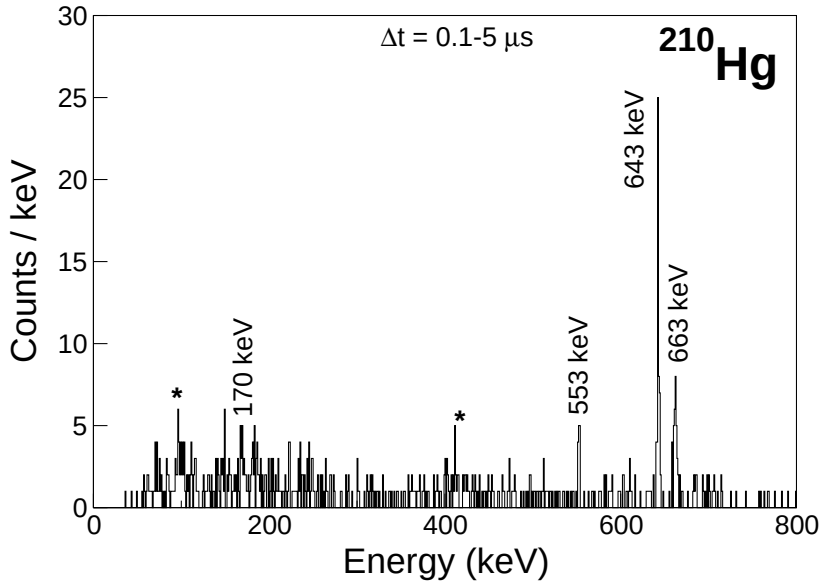

Figure 4.38: ^{210}Hg γ-ray spectrum from the decay of isomeric state(s). The spectrum has been obtained by gating on the time window 0.1- 5 μs.

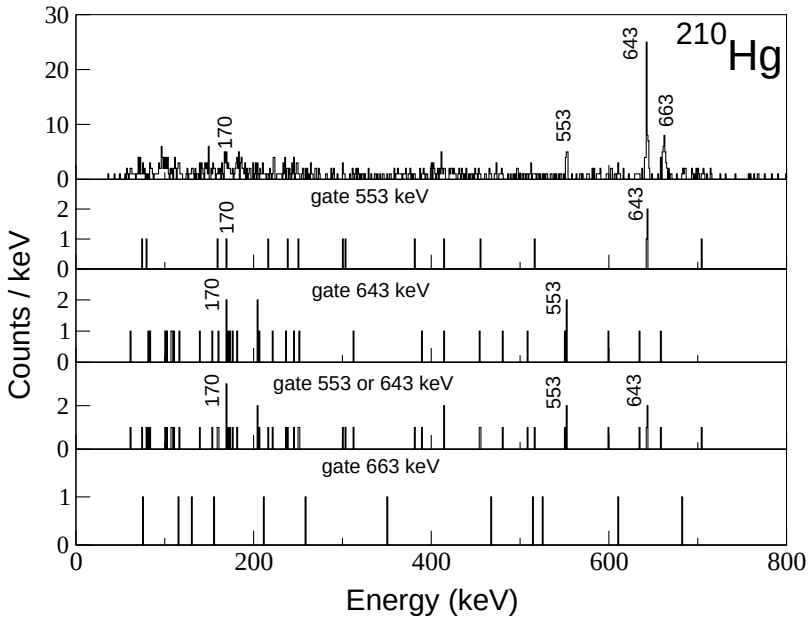

Figure 4.39: Gamma-ray prompt coincidence spectra for the decay from isomeric state(s) in ^{210}Hg, with gates on the four transitions of ^{210}Hg. The γ spectrum of ^{210}Hg is reported on top for eye guidance.

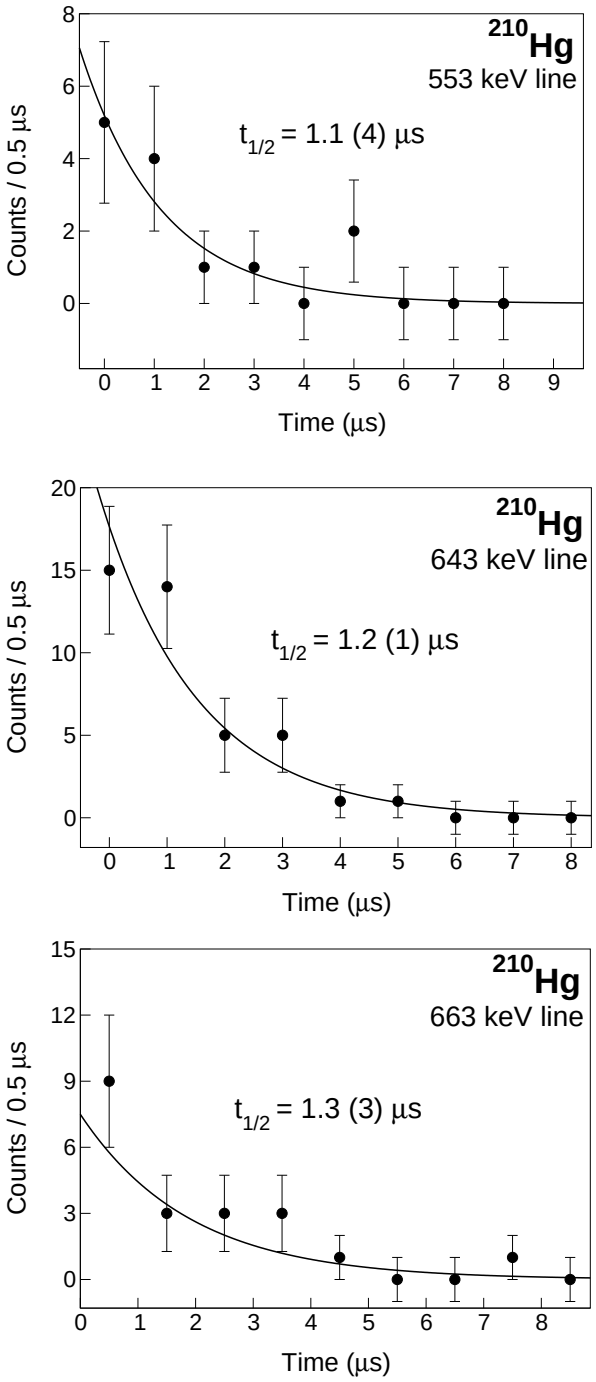

Figure 4.40: Time distributions for the 553-, 643- and 663-keV transitions assigned to ^{210}Hg.

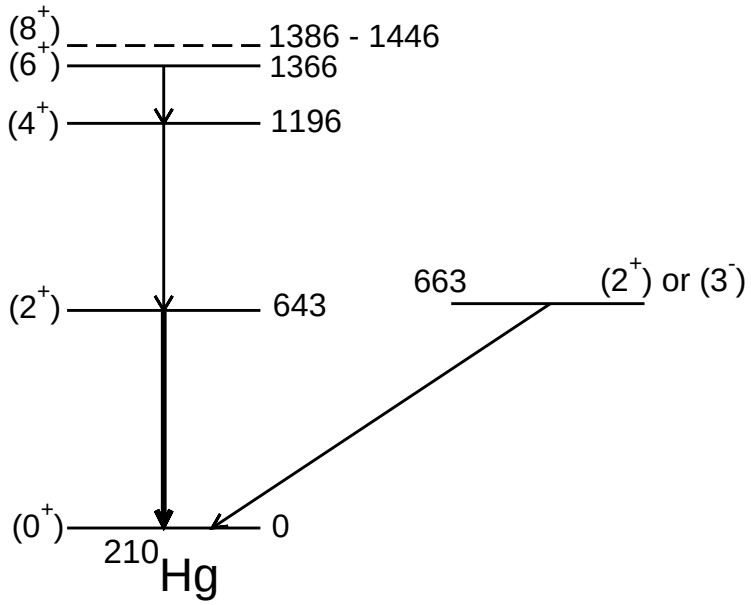

Figure 4.41: Level scheme proposed for ^{210}Hg. The arrows represent the observed γ rays.

Whenever a theory appears to you as the only possible one, take this as a sign that you have neither understood the theory nor the problem which it was intended to solve

Objective Knowledge: An Evolutionary Approach – Karl Raimund Popper

5 Theoretical analysis

The lead and nearby isotopes studied in this thesis are systems with few neutron particles and one or two proton holes or particles with respect to the doubly-magic ^{208}Pb. Consequently, their behaviuor can be interpreted within a shell-model framework, as calculations with few nucleons are feasible even in the quite large valence space (high-j orbitals) above the ^{208}Pb closed core. The basic notions of nuclear shell model were introduced in the first chapter. However, when realistic calculations are required, one needs to start from modern shell model techniques and computer codes, which are nowadays a powerful tool to understand nuclear structure [12]. In this chapter the most relevant concepts behind a shell-model calculation are described. There is also a discussion on more schematic models, such as the idea of seniority conservation, which nonetheless are important as a first approach in the study of the observed exotic nuclei.
The main goal of the present theoretical analysis is to explain the structure of even-even lead isotopes and especially the problem of the transition strengths from the isomeric states that are significantly different from shell-model predictions. A detailed analysis will point out how the introduction of effective three-body forces, so far usually neglected, may reestablish at, least partially, agreement with the experimental data.
Also the other observed isomers, discussed and compared to shell-model calculations, exhibit important differences from the regular, seniority-scheme driven behaviour which is more effective for describing lead isomers.

5.0.3 Modern shell-model calculations

As the number of protons and neutrons departs from the magic numbers, the residual part of the hamiltonian in Eq. 1.2 should be introduced for a realistic calculation. This requires a precise formulation of the problem in second quantization, which starts from the choice of harmonic oscillator wave-function as the basis to define the Slater determinants for the full many-body system. As a result, the many-body problem reduces to the diagonalization of a matrix which is the nuclear hamiltonian written as:

$$H = \sum_{ij} K_{ij} a_i^\dagger a_j - \sum_{i \leq j, k \leq l} V_{ijkl} a_i^\dagger a_j^\dagger a_k a_l \tag{5.1}$$

where K is the kinetic energy and V is the potential energy. The construction and destruction operators obey the Pauli Principle ($a_i^\dagger a_j = \delta_{ij}$) and the wave function is constructed, for A nucleons, as $a_{i,1}^\dagger ... a_{i,A}^\dagger |0\rangle = |\Phi_I\rangle$. The dimensionality of the matrix is too large to enable diagonalization, except for light nuclei. Therefore, it is necessary to restrict the calculation to a valence space and to have an interaction suited for the space chosen: in this way the secular problem of the full system, not solvable analytically or numerically, is reduced to a much smaller space, which can be handled by modern computer codes.

The valence space Typically, for medium and heavy nuclei, one restricts to a valence space outside a doubly-magic nucleus, made of one major oscillator shell plus an intruder state from the major oscillator shell above. In order to fix ideas, for the lead isotopes investigated in this thesis, the valence space is the neutron space above ^{208}Pb, i.e. outside the Z = 82, N = 126 core. The shells are $g_{9/2}, i_{11/2}, d_{3/2}, d_{5/2}, g_{7/2}, s_{1/2}, j_{15/2}$, all belonging to the N = 6 major shell except $j_{15/2}$ that is the intruder state from N = 7 major shell.

The effective two-body interaction The nucleon-nucleon potential has been studied via nucleon-nucleon scattering since many years, and the amount of data gathered has allowed to extract very accurate nuclear potentials. The first pioneering attempts date back in the '60s, with the Kuo and Brown work [90]. Among the most modern potentials, the Argonne-V18 [4] and the CD-Bonn [91] interactions are the most used, and they fit the scattering data with a $\chi^2 \approx 1$. The renormalization of the repulsive part of the nucleon-nucleon force exploits methods such as G-matrix [90] and V_{lowK} approach [92] which are actually quite similar, conferring them a model-independent status (see also later the monopole/multipole discussion on this point).
Once the two-body interaction has been obtained, it has to be renormalized to be adapted to the chosen valence space, thus becoming an effective interaction.

Monopole and multipole components of the nuclear hamiltonian An effective approach to treat the nuclear many-body hamiltonian is to divide the operator in a

monopole (m) and multipole (M) part [93]:

$$H = H_m + H_M$$

H_m contains the kinetic energy and all the monopole part of two- and, in case, three-body interactions. It is thus responsible for the global saturation properties and for the spherical single-particle energies. H_m is not easy to renormalize and in general its centroids have to be empirically corrected if agreement with data is desired [94, 12]: it assumes the form of

$$H_m = \sum_i n_i \epsilon_i + \sum_{i \leq j} n_i n_j V_{ij}$$

where the sum is over all nucleons in the valence space, ϵ_i is the single particle energy and V_{ij} is the interaction. The presence of terms which are quadratic in the number of nucleons in different orbits implies that, with a sufficient number of particles, even small changes in the centroids may lead to major shift in the hamiltonian spectrum. Moreover, it has been proved that the inclusion of three-body terms is essential for the correct reproductions of the binding energies, the shell closures as N = 28 and, in general, many spectroscopic features of nuclear structure [4, 5, 6, 7].
On the contrary, the multipole part H_M is much more under control for its renormalization. It contains the important pairing, quadrupole, octupole terms, which are responsible for correlations and coherence in nuclei. By calculating the spectrum of the H_M operator with a standard interaction, it appears that the vast majority of eigenvalues have a gaussian distribution around zero, thus being very similar to the result of a random hamiltonian. The few eigenvalues which are detached from the gaussian distribution represents the pairing, quadrupole, octupole and other components (not all well understood) of the hamiltonian. In particular, the pairing and quadrupole terms are the most relevant ones [12, 93].

5.1 Electromagnetic nuclear transitions

The interaction between the nucleons and the electromagnetic field provides the most common de-excitation modes for excited nuclei. Moreover, the structure of the electromagnetic interaction is simple and well known (contrary to the case of nuclear interaction) and thus it is an effective probe to study nuclear structure. In particular, the quadrupole moment and the associated E2 transition probabilities are a fundamental tool to assess the nuclear wave function.

5.1.1 Quadrupole moment and E2 transitions

The quadrupole moment of a nucleus is a measure of the extent to which the proton distribution, i.e. the charge distribution in the nucleus, deviates from spherical symme-

try [14]. For a state with angular momentum I and projection M it is defined by:

$$Q = \langle I, M = I | Q_{op} | I, M = I \rangle \tag{5.2}$$

where the quadrupole operator Q_{op} is:

$$eQ_{op} = \int \rho_e(\overrightarrow{r}) r^2 (3\cos^2\vartheta - 1) d^3r \tag{5.3}$$

In Eq. (5.3) e is the electric charge, r the radius of the nucleon shell, and $\rho_e(\overrightarrow{r})$ is the charge density distribution.
The quantity Q is actually the diagonal matrix element of the quadrupole operator: the non-diagonal matrix elements represent the transition moment $E2$ which is involved in processes like γ decay and Coulomb excitation. The matrix element of the electric quadrupole tensor is:

$$M(E2, \mu) = \int \rho_e(\overrightarrow{r}) r^2 Y_{2\mu}(\vartheta, \varphi) d^3r \tag{5.4}$$

where $Y_{2\mu}(\vartheta, \varphi)$ are the usual spherical harmonic functions. If $\mu = 0$ then $M(E2, 0) = Q_{op}$, which is the static quadrupole moment. The Wigner-Eckart theorem states that the matrix element of any spherical tensor, in a basis which is an eigenstate of the angular momentum, can be written as the product of two factors. One of them is a Clebsch-Gordan coefficient, while the other, called reduced matrix element, contains the physical information and is independent of the angular momentum orientation. The corresponding reduced transition probability between states with angular momentum I_1 and I_2 is:

$$B(E2, I_1 \to I_2) = \sum_{\mu, M_2} |\langle I_2 M_2 | M_{E2,\mu} | I_1 M_1 \rangle|^2 = \frac{1}{2I_1 + 1} |\langle I_2 || M(E2) || I_1 \rangle|^2 \tag{5.5}$$

Equation 5.5 gives a straightforward result for the transition of a single proton:

$$B_{sp}(E2, j_1 \to j_2) = \frac{5}{4\pi} e^2 \langle j_1 \frac{1}{2} 20 | r^2 | j_2 \frac{1}{2} \rangle^2 \langle j_2 | r^2 | j_1 \rangle^2 \tag{5.6}$$

However, the experimental evidences have pointed out that even when there is really only one nucleon involved in the quadrupole transition, Eq. 5.6 often largely underestimates the transition rate. The most striking case is the one of a single-neutron transition which should have a B(E2) equal to zero, being instead often very different from such value.

5.1.2 Effective charges

The introduction of an effective charge for protons and neutrons renormalizes the effects not taken into account in the calculation. The origin of the effective charge for a nucleon outside a closed core can be viewed as a polarization of the core due to the presence

of external nucleons [14]. The extra field generated by the particle outside the core is non-spherical and its order of magnitude can be estimated by considering that the eccentricity of mass distribution in nuclei is of the order of A^{-1} [14]. Therefore, the orbit of the protons in the core is distorted and will acquire an extra quadrupole moment of the order $A^{-1}Q_{sp}$, where Q_{sp} is the quadrupole operator in the single-particle estimation. The resulting quadrupole moment induced by polarization would be $Q_{pol} \sim \frac{Z}{A}Q_{sp}$ [14]. Microscopically, the polarization of the core corresponds to the virtual excitations of particles in closed orbits into higher shells [95]. The associated frequencies ($\Delta E \sim 2\ \hbar\omega \sim 80\ A^{-1/3}$ MeV) are thus very high compared with the transition energies ($\Delta E \sim 1$ MeV) involved in the transitions usually observed in the low-excitation region of atomic nuclei. As a consequence, the polarization follows adiabatically these transitions and the renormalization due to core polarization acts for both static quadrupole moments and transition moments. Being the effect of core polarization a small perturbation of the spherical configuration, the action of the external particles can be regarded as simply additive, and in calculations it is often interpreted as a correction to the charge of each individual nucleon outside the core, which thus assumes an effective charge e_{eff} [95]. This, for an E2 transition between states with momenta j_2 and j_1, is defined as:

$$(e_{eff})_{E2} = \frac{\langle I_2 = j_2 | M_{E2,\mu} | I_1 = j_1 \rangle}{\langle j_2 || r^2 Y_2 || j_1 \rangle} = e\left(\frac{1}{2} - t_z\right) + (e_{pol})_{E2} \tag{5.7}$$

where t_z is the isospin. It can be seen that the polarization charge e_{pol} is simply the difference between the effective charge and the charge of the single nucleon.
A more quantitative estimation of the effective charge for E2 transitions can be performed by explicitly considering the coupling of the valence nucleon to the high-frequency quadrupole excitation modes of the core [95]. It is also fundamental to take into account whether e_{pol} is different for neutrons and protons, i.e. if there is also an isovector component besides the isoscalar one in the quadrupole polarization. The quantitative estimation starts by considering the isoscalar quadrupole field F responsible for the deformation of the spherical potential:

$$F = \sum_k (r^2 Y_{20}(\theta))_k$$

A similar potential is used to evaluate the isovector component of the quadrupole polarization:

$$F = \sum_k (r^2 Y_{20}(\theta)\tau_z)_k$$

where τ_z is the isospin third component. After these fields are introduced, the sum rule of the quadrupole operator is calculated and the following expression is derived for the static quadrupole moment [95]:

$$e_{pol}(E2, \Delta E) = e\left(\frac{Z}{A} - 0.32\frac{N-Z}{A} + \left(0.32 - 0.3\frac{N-Z}{A}\right)\tau_z\right)\frac{\frac{3}{5}R^2}{\langle j_2 | r^2 | j_1 \rangle} \tag{5.8}$$

where the last factor takes into account the dependence of the effective charge on the radial matrix elements of the different orbits, which has recently been experimentally outlined in Ref. [96]. Table 6-9 of Ref. [95, pag. 517] shows the calculated and measured effective charges, which are in quite good agreement. In particular, we point out the value for the unpaired neutron in ^{209}Pb, $e_{eff} = 0.8$, as it is the relevant one for the neutron-rich lead nuclei that will be discussed in the following.

5.2 Calculations for the even-even lead isotopes

The general behaviour of the isomers in the even-even lead isotopes will be first discussed with the seniority scheme, which provides an analytical solution for the transition energies and the for transition operator matrix elements. Afterwards, more detailed, and realistic, shell-model calculations will be presented.

5.2.1 Seniority scheme in the even-even lead isotopes

The seniority quantum number ν emerges naturally when one tries to provide a complete set of eigenvalues to describe a certain nuclear state in a given j shell [21, 22]. It is the number of particles not coupled to angular momentum zero. One of the most important properties of nuclear states with good seniority is that the two-body interactions of odd-tensor operators are linear in the number of paired particles, $(n - \nu)/2$. It follows that the energy differences between states with $\nu = 0$ and $\nu = 2$ and between states with $\nu = 2$ but different angular momentum J are identical to the two-particle system, independently of the number n of particles in the j shell [21, 22]:

$$E(j^n, \nu = 2, J) - E(j^n, \nu = 0, J = 0) = \langle j^2 J|V|j^2 J\rangle - V_0$$

$$E(j^n, \nu = 2, J) - E(j^n, \nu = 2, J') = E(j^2, \nu = 2, J) - E(j^2, \nu = 2, J')$$

where V_0 is the energy of a pair of particles coupled to zero. Therefore, if, for example, the valence neutrons in the lead isotopes occupy the $\nu g_{9/2}$ shell, in the four even-even isotopes (^{210,212,214,216}Pb) the same levels will have the same energy. The resulting levels schemes will thus behave according to Fig. 5.1.

This can be compared to the actual levels schemes deduced from this and the previous works, in Fig. 5.2. The experimental levels resemble very much those of the seniority scheme, apart form a slight tendency of the levels to increase their energies with increasing neutron number, which will be discussed in the next section. For even-tensor operators the seniority scheme provides similar simplification and the result for electrical quadrupole transition strength B(E2) is of particular importance in the present case. The reduced quadrupole matrix element between states with good seniority is a function of the transition matrix element for two particles (essentially the matrix element of $\mathbf{r}^2$)

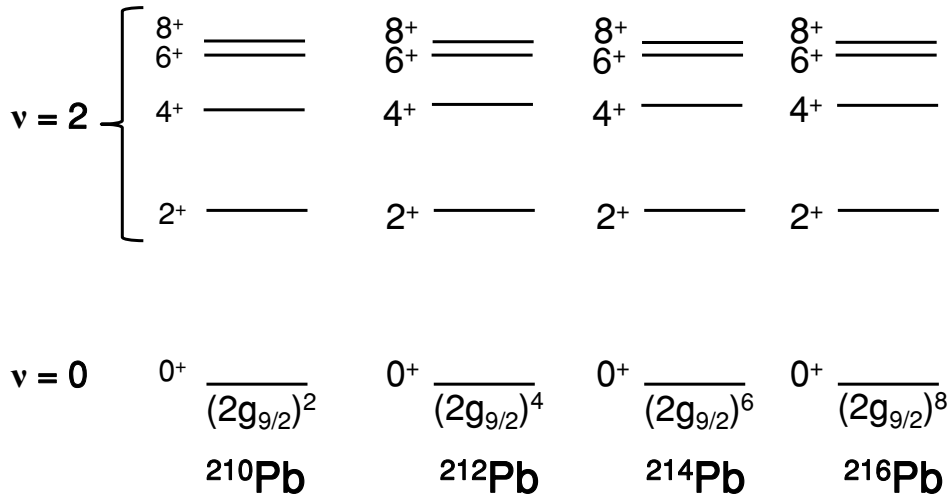

Figure 5.1: Energy levels in a seniority scheme for the $(g_{9/2})^n$ configuration.

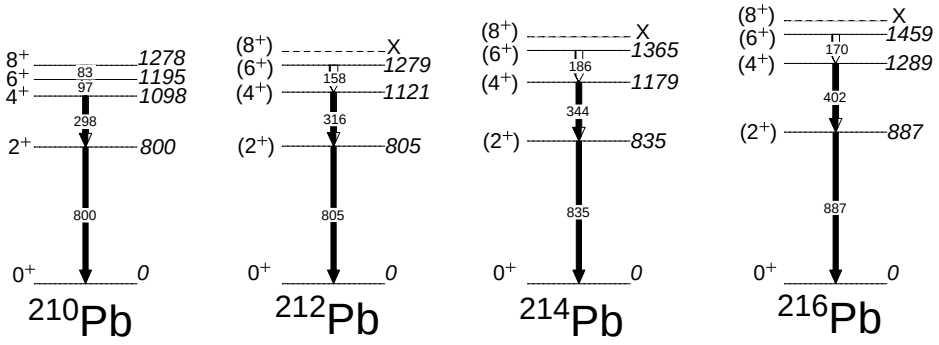

Figure 5.2: Experimental level schemes for the neutron-rich lead isotopes $^{210-216}$Pb. The level schemes of ^{212,214,216}Pb have been derived from the present work.

and of the square of the number of particles [22]:

$$\langle j^n J = 2^+ || \mathbf{Q} || j^n J = 0^+ \rangle^2 = \left(\frac{n(2j+1-n)}{2(2j+1)} \right) \langle j^2 J = 2^+ || \mathbf{Q} || j^2 J = 0^+ \rangle^2 \qquad (5.9)$$

In the case of the $\nu g_{9/2}$ shell, the Eq. 5.9 implies that the B(E2;$8^+ \rightarrow 6^+$) should show a parabolic behaviour with respect to the number of particles, with a ratio 9:1:1:9 for the chain ^{210}Pb,^{212}Pb,^{214}Pb,^{216}Pb. In a more realistic picture, one should consider the presence of other orbitals, in particular the $\nu i_{11/2}$. With more shells involved, as the number of neutrons grows, the E2 strengths start to be the sum of many more

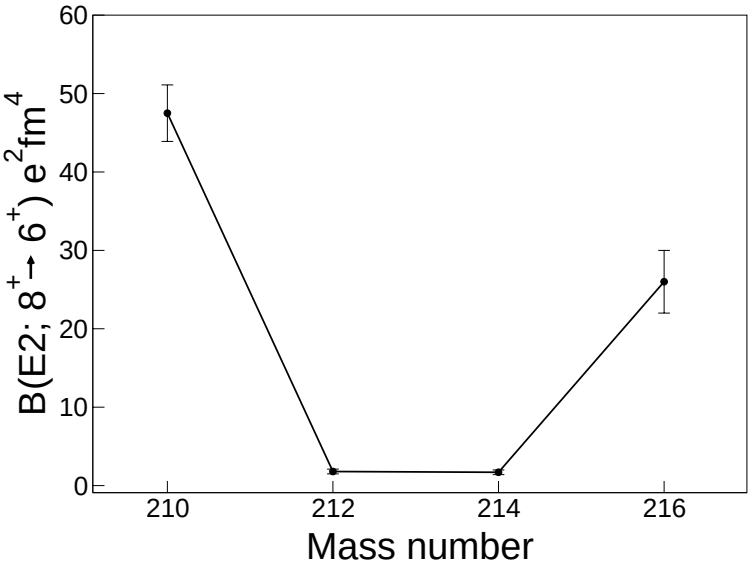

Figure 5.3: B(E2)values for the $8^+ \rightarrow 6^+$ transitions in lead isotopes extracted from the experimental data of the present thesis. A solid line was added to provide eye guidance.

contributions. Therefore, one can expect that the B(E2;$8^+ \rightarrow 6^+$) of ^{212}Pb, ^{214}Pb, ^{216}Pb become larger with respect to the prediction of the pure seniority scheme. As it will be shown in the following, this is not the case. The experimental B(E2) values in Fig. 5.3 follow roughly the expected quadratic behaviour and a precise comparison with the shell-model estimations will be presented in the next section.

5.2.2 Seniority conservation in the $\nu g_{9/2}$

It is essential to highlight at this point some general properties of seniority conservation rules and their effect on the B(E2) strengths and hence on nuclear isomerism. The conservation of seniority by the nuclear hamiltonian is a well-studied subject. A theorem [21] states that any two-body interaction is diagonal in seniority if it is so in the j^3 configuration. This second condition is satisfied if there are no matrix elements connecting the $\nu = 1$ and $\nu = 3$ states. This is always true for $j \leq 7/2$, because there are no states with different seniorities 1 and 3 and the same j, which could be mixed by the nuclear hamiltonian (a proper nuclear hamiltonian can only mix states with same J). For larger angular momenta this property does not hold anymore. Therefore, in the $\nu g_{9/2}$ shell the seniority can be, and actually is, violated. More in detail, the general condition for seniority conservation in a j shell, with particles coupled to $J = 0, 2, ..., 2j - 1$ is given

by [28, 97, 98]:

$$\sum_{J=2}^{2j-1}(2J+1)\sqrt{2I+1}\left(\frac{\delta_{JI}}{\sqrt{(2J+1)(2I+1)}}+2\begin{Bmatrix} j & j & J \\ j & j & I \end{Bmatrix}-\frac{4}{4j^2-1}\right)V_J=0 \quad (5.10)$$

where V_J is the interaction matrix element, $I = 2, 4, ..., 2j-1$, and the symbol between curly brackets is a $6j$ Racah coefficient. Consistently with what stated above, this system of equations does not provide any condition on V_J until $j \leq 7/2$, i.e. seniority is always conserved. For $j \geq 9/2$ there is one condition on the interaction matrix element, and thus a general hamiltonian violates seniority conservation. The mixing of states with different seniority can be particularly relevant for the B(E2) values, since the E2 transition is strongly favoured between states with different seniority. More specifically, in the case of the $\nu 2g_{9/2}$ isomers in lead isotopes, the nature of the 8^+ and 6^+ states which determine the existence of the observed isomers can be investigated in terms of their seniority. For the four- and six-particle systems ^{212}Pb, ^{214}Pb there are one $\nu = 2$ and two $\nu = 4$ 6^+ states, and two 8^+ states, one with $\nu = 2$ and one with $\nu = 4$. In the next section it will be shown the effect produced by the fact that the B(E2) between the $\nu = 2$ and the $\nu = 4$ states is two orders of magnitude larger that the one between $\nu = 2$ states. This means, for example, that a μs half life is reduced to 10 ns one in case the 6^+ state is a mixing of $\nu = 2$ and $\nu = 4$ seniorities. Since the extent of the mixing is related to the relative position in energy of the three 6^+ states, i.e. to the nuclear interaction, different regions of the Segrè chart show dissimilar behaviour. A further complication actually arises for the $g_{9/2}$ shell: it has been demonstrated, see Ref. [99, 100], that one of the two $\nu = 4$, 6^+ states does not mix with the $\nu = 2$ state, while the other does. This is however true only in a pure $g_{9/2}$ configuration, whereas the participation of other shells (such as $i_{11/2}$ or $j_{15/2}$) in the wave function will determine the mixing of all the three 6^+ states. In any case, the nature of the 6^+ states has to be assessed carefully in order to calculate their mixing. In Fig. 5.4 and 5.5 the level schemes of the isotones with protons in the $\pi 1g_{9/2}$ orbit and of the isotopes with neutrons in the $\nu 1g_{9/2}$ shell is shown, respectively [101, 27]. The $\nu = 4$ levels are in bold. In the case of the $\pi 1g_{9/2}$ [102] the 6^+ state with $\nu = 4$ is far in energy from the $\nu = 2$ state, and thus their mixing is negligible in ^{94}Ru and ^{96}Pd [27]. As a consequence, these nuclei present an 8^+ isomer, similarly to the lead isotopes [103]. On the contrary, in the isotopes with neutrons in the $\nu 1g_{9/2}$ the 6^+ state with $\nu = 4$ is lower in energy than the $\nu = 2$ level [27]: it can be that the yrast 6^+ has actually $\nu = 4$. This fact results in large B(E2) values from the 8^+ state, which thus is not anymore an isomeric state in ^{72,74}Ni [104]. In the case of lead isotopes, shown in Fig. 5.6 the experimental levels are compared with the ones obtained from an empirical shell model [101]: the interaction is taken from the spectrum of ^{210}Pb and then refitted to the nuclei up to ^{216}Pb. The neutrons filling the $2g_{9/2}$ give origin to an excitation scheme similar to the one of proton filling the $1g_{9/2}$, and in fact the 8^+ state is isomeric.

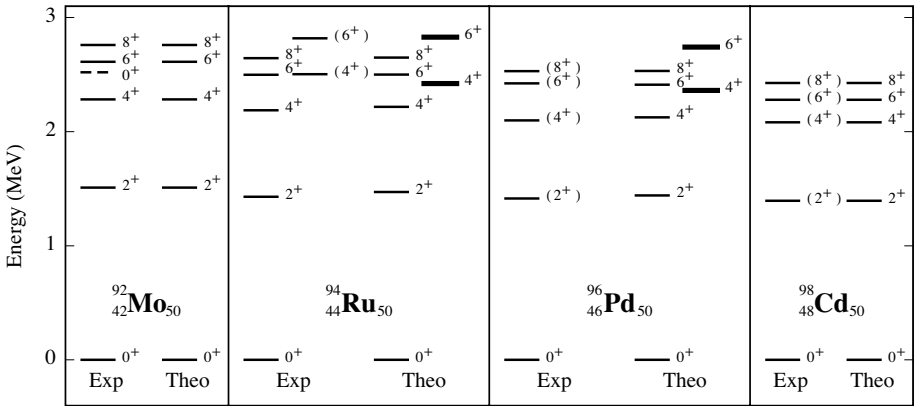

Figure 5.4: Relevant level schemes for the isotones with protons filling the $1g_{9/2}$. The left-hand parts of each panel show the observed levels while the right-hand parts contain the results of a $(1\pi g_{9/2})^n$ shell-model calculation with linearly varying two-body matrix elements. The $J^\pi = 4^+$ and 6^+ levels with exact $\nu = 4$ are shown with thick lines; the dashed line corresponds to an intruder level. Picture taken from Ref. [101, 27].

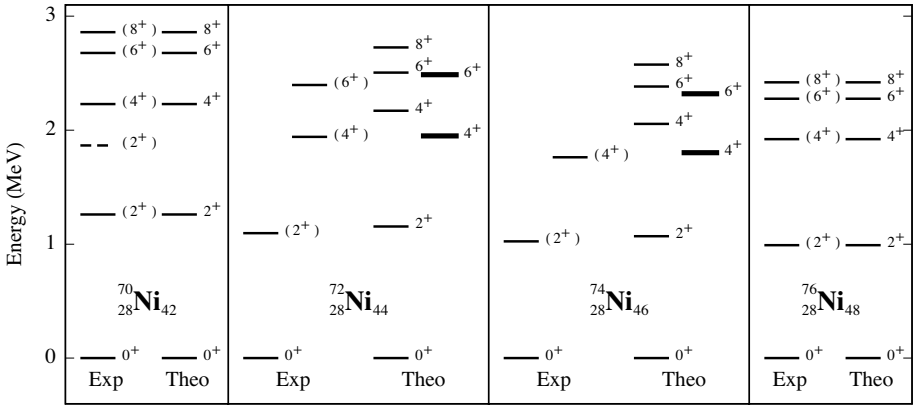

Figure 5.5: Relevant level schemes for the Ni isotopes with neutrons filling the $1g_{9/2}$. The left-hand parts of each panel show the observed levels while the right-hand parts contain the results of a $(1\nu g_{9/2})^n$ shell-model calculation with linearly varying two-body matrix elements. The $J^\pi = 4^+$ and 6^+ levels with exact $\nu = 4$ are shown with thick lines; the dashed line corresponds to an intruder level. Picture taken from Ref. [101, 27].

5.2.3 Shell-model calculations

In the previous section the importance of shell-model calculations to better understand the level structure of lead isotopes has been pointed out. This region of the chart of nuclides, being close to the doubly-magic nucleus ^{208}Pb, is also an effective testing

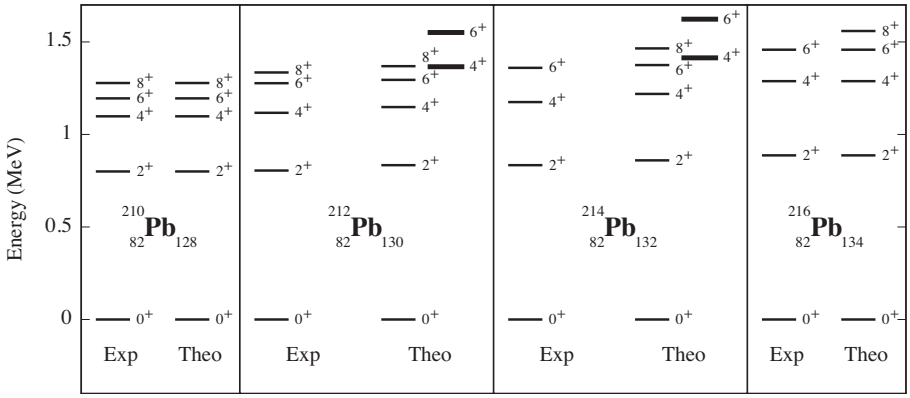

Figure 5.6: Level schemes for Pb isotopes with neutrons filling the $2g_{9/2}$. The left-hand parts of each panel show the observed levels while the right-hand parts contain the results of a $(2g_{9/2})^n$ shell-model calculation with linearly varying two-body matrix elements. The $J^\pi = 4^+$ and 6^+ levels with exact $\nu = 4$ are shown with thick lines. Picture courtesy of P. Van Isacker [101].

ground for nuclear interactions. Modern shell-model calculations, involving many shells, give a much more realistic description of the nuclear structure with respect to the quite schematic seniority concept.

Empirical shell model The most direct interpretation of the structure of neutron-rich Pb isotopes can be inferred from an empirical shell model: the interaction is derived from the spectrum of ^{210}Pb, assuming that only the $\nu 2g_{9/2}$ is being occupied, and the ^{208}Pb core is completely closed [105]. In this model the excited levels of the different isotopes will be necessarily at the same energy of the experimental ones of ^{210}Pb. The B(E2) values are calculated using an effective charge for neutrons equal to 0.8: this is the effective charge expected for neutrons in this region and valence space, see Ref. [95, 106] and Eq. 5.8. Figure 5.7 shows the comparison between theoretical and experimental values obtained from the experiment. The agreement seems satisfactory for all the isotopes except ^{216}Pb, even though the empirical shell model is not derived from a realistic-nucleon-nucleon potential. However, to better understand the result, the wave function of the states in ^{212}Pb ($\nu 2g^4_{9/2}$) and ^{214}Pb ($\nu 2g^6_{9/2}$) has to be investigated in terms of seniority 2 and 4 components. In the interaction used the $\nu = 4$, 6^+ state which can mix is about 250 keV higher in energy than the $\nu = 2$ partner, in both isotopes. Their mixing is thus very small, of the order of 1/1000, and the resulting B(E2) from the 8^+ state is 3.7 e^{2}fm^4, whereas a pure $\nu = 2$ 6^+ state would imply a B(E2) of 5.5 e^{2}fm^4 [105]. This change with such a small admixture is due to the much larger transition strength in case of a $\nu = 4$ 6^+ state, as pointed out in the previous section. This confirms how even very

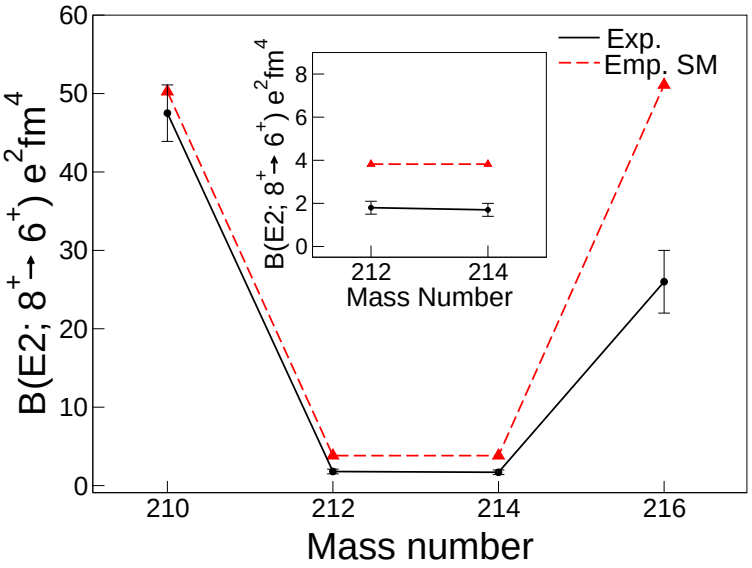

Figure 5.7: B(E2) values for the $8^+ \rightarrow 6^+$ transitions in lead isotopes extracted from experimental data compared with the ones obtained from an empirical shell model.

small mixings of the wave function could generate large changes in the sensitive nuclear observables, such as lifetimes.

Shell model with the Kuo-Herling interaction A more realistic calculation of the nuclear wave functions can be done using the full major-shell valence space above N = 126, but always keeping closed the doubly-magic core ^{208}Pb. The Kuo-Herling interaction, in its modified version as in Ref. [106], is a well-establish model of nuclear forces in this region of the chart of nuclides [106, 107]. The single-particle energies of the valence orbitals are reported in Fig. 5.8: they are deduced from the excitation spectrum of ^{209}Pb [106]. The codes ANTOINE and NATHAN [108, 109] were employed and the full neutron valence space was taken into consideration. The resulting levels schemes are in Fig. 5.9, where they are also compared with the experimental results. The overall agreement is very satisfactory and even the slight tendency of the level energies (see for example the 2^+ energy) to increase as a function of atomic mass A is reproduced. However, this behaviour is better understood as an increasing binding energy of the ground state, as a consequence of its increased pairing. Shell-model calculations confirm this fact, showing also that the binding energy of the 8^+ states remains roughly constant.

In Tab. 5.1 the wave functions (occupational numbers) of the isomeric states are reported. As expected, the $\nu 2g_{9/2}$ is the most important orbital, but the wave function becomes more fragmented going towards more neutron-rich nuclei. The $\nu 1i_{11/2}$, in particular, is important, with a contribution to the wave function up to 20%. The wave

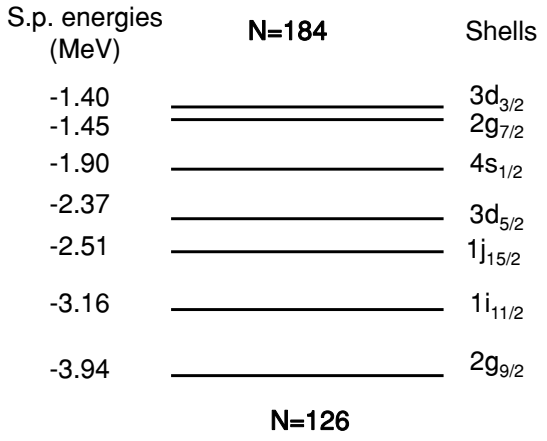

Figure 5.8: Neutron single-particle energies above N = 126 from the Kuo-Herling interaction.

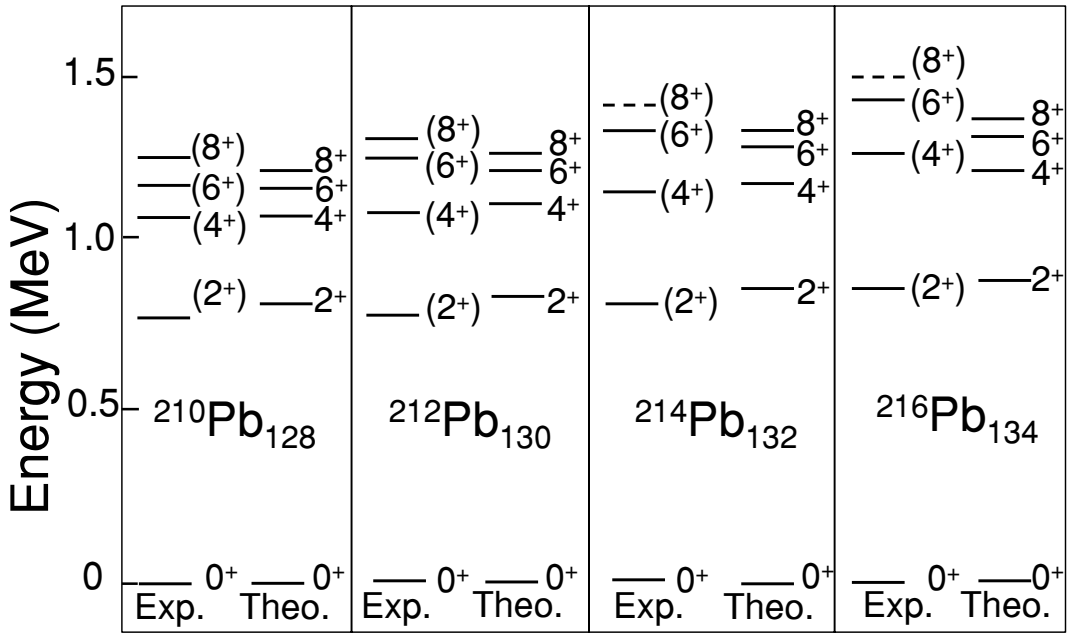

Figure 5.9: Comparison between theoretical and experimental level schemes for lead isotopes showing up to the 8^+ state. The theoretical calculations performed with ANTOINE, using the KH interaction and a ^{208}Pb core, with the valence space with neutrons filling the $2g_{9/2}$, $1i_{11/2}$, $1j_{15/2}$, $3d_{5/2}$, $3d_{3/2}$, $4s_{1/2}$, $2g_{7/2}$ shells.

	^{210}Pb	^{212}Pb	^{214}Pb	^{216}Pb	^{218}Pb
$2g_{9/2}$	1.99	3.39	4.78	6.21	6.96
$1i_{11/2}$	0.005	0.33	0.68	1.04	2.16
$1j_{15/2}$	0.002	0.16	0.32	0.43	0.59
$3d_{5/2}$	0.0008	0.04	0.08	0.11	0.14

Table 5.1: Occupational numbers of the most relevant valence orbitals for the 8^+ states in lead isotopes, as calculated by ANTOINE

functions are thus quite pure, even though the significant contribution of $\nu 1i_{11/2}$ can lead to a divergence from the B(E2) values expected in a seniority scheme. The B(E2) from the 8^+ have been calculated with the ANTOINE and NATHAN codes, using an effective charge of 0.8 for the neutrons, as for the empirical shell model, and the results are shown Fig. 5.10.

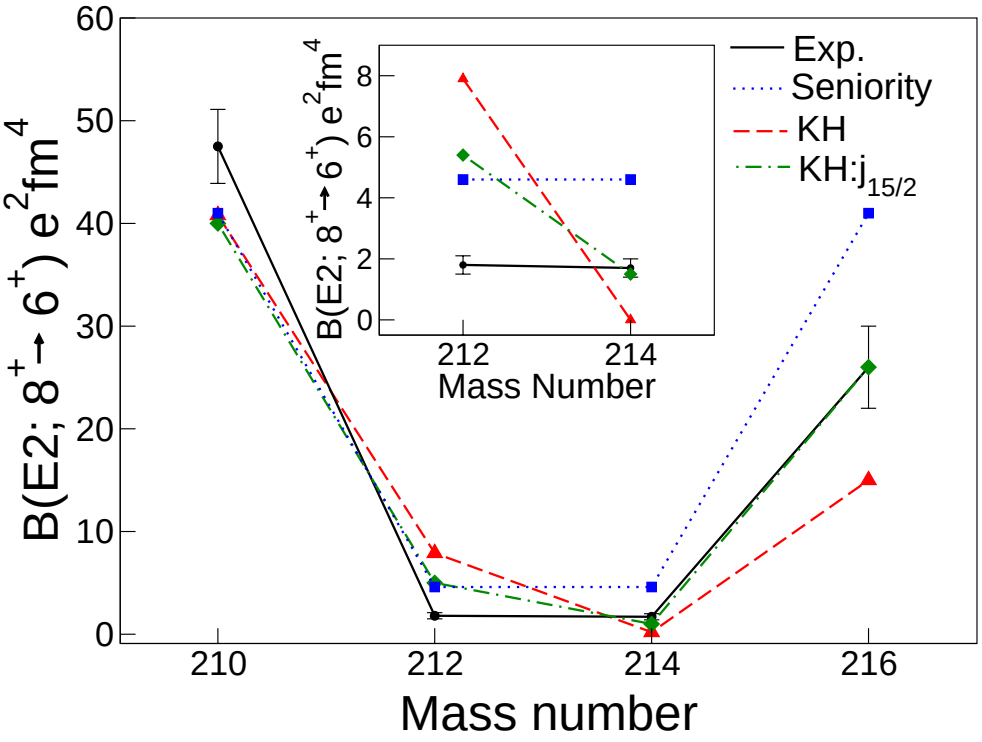

Figure 5.10: B(E2;$8^+ \rightarrow 6^+$) extracted from experimental data in lead isotopes. They are compared with the ones obtained from the seniority scheme, from the original KH interaction, and from the KH interaction when the $j_{15/2}$ shell single-particle energy is increased by 1 MeV.

The disagreement for ^{212}Pb and ^{214}Pb, roughly a factor 4, is too large to be justi-

fied by a change in the effective charge. In fact, a factor 4 discrepancy in the B(E2) means a factor 2 change in the effective charge, as it scales with the square root of the transition strength. It is worth noticing that the behaviour for ^{212}Pb predicted by the Kuo-Herling interaction is consistent with what one would expect in a seniority scheme with a correction due the presence of the $\nu i_{11/2}$. In fact, the quadrupole moment of four neutrons coupled in the $(\nu g_{9/2})^2(\nu i_{11/2})^2$ configuration has the same sign of that of the $(\nu g_{9/2})^4$ wave function [105]. As a consequence, a component $(\nu g_{9/2})^2(\nu i_{11/2})^2$ in the wave function of ^{212}Pb leads to a significant increase of the expected B(E2) value. This is clearly shown by the theoretical ratio between the B(E2) values of ^{210}Pb and ^{212}Pb, which is 5:1, smaller than the ratio 9:1, valid for a pure $g_{9/2}$ shell.
The calculation for ^{214}Pb indicate a similar disagreement with the experimental value, but in this case the theoretical B(E2) is five times smaller than the measured one. This behaviour can be understood if one considers that the quadrupole moment of the $(\nu g_{9/2})^6$ configuration is now of opposite sign with respect to the $(\nu g_{9/2})^4(\nu i_{11/2})^2$ one. As a result, the destructive interference between the two components of the wave function leads to a very small transition strength [105]. Since, in this situation, small changes of the contributions from various configurations can produce large differences, it is not surprising that the final result is strongly model-dependent, although remaining very different from the experimental data.

Previous problems in the $1g_{9/2}$ shell It is also important to note that discrepancies between calculated and experimental B(E2) values of seniority isomers in the first $g_{9/2}$ shell have been found for protons in ^{98}Cd [110] and neutrons in ^{72}Ni [104]. In Ref. [110] the authors found that the B(E2) strenght from the 8^+ isomer is a factor 4 less than what calculated from shell model, and speculated that this was related to effects induced by the vicinity of the proton drip line and by the differences in the proton-holes and neutron-particles wave functions. In Ref. [104] the non-detection of the 8^+ isomer in ^{72}Ni allowed to put an upper limit to its lifetime which is lower with respect to expectations from the seniority scheme, being known the lifetime of the same isomer in ^{70}Ni. It was claimed that the non existence of the isomer was linked to seniority-mixing effects (see later).

Comparison between interactions In order to assess if the discrepancy with experimental data is due to a problem with the interaction used, different nuclear hamiltonians have been tested. Besides the Kuo-Herling interaction, two other interactions were used. One of the interactions was derived from first principles, the CD-BONN nucleon-nucleon interaction, using the V_{lowK} approximation [105]. The other hamiltonian is a simple Delta interaction of the form $V(\vec{r_1}, \vec{r_2}) = -V_0\delta(\vec{r_1} - \vec{r_2})$, where V_0 is the strength of the interaction [105]. The results for the B(E2) values are reported in Tab. 5.2

The Kuo-Herling and CD-BONN interaction, both from first principles, gives very similar results. The only significant difference is for ^{214}Pb, because the B(E2) is very sensitive to small changes in the matrix elements, as stated above. However, the ratio

Hamiltonian	^{210}Pb	^{212}Pb	^{214}Pb	^{216}Pb
B(E2) (e^2fm^4) Kuo-Herling	40.9	7.9	0.2	14.8
B(E2) (e^2fm^4) CD-BONN	41.6	8.1	0.1	12.3
B(E2) (e^2fm^4) Delta	39.4	9.3	0.005	5.6

Table 5.2: Theoretical B(E2) values for different interactions, for harmonic-oscillator (HO) potential, for the isomeric states in lead isotopes.

between ^{210}Pb and ^{212}Pb is similar in both interaction and in strong disagreement with the experimental values. Also for ^{214}Pb the disagreement does not change qualitatively. Concerning the Delta interaction, the results for two and four neutrons in the valence space are consistent with the realistic interactions from first principles, whereas the value for ^{214}Pb is almost zero due to the problem highlighted above. The agreement between the various interactions is remarkable and makes it difficult to identify how the nuclear hamiltonian should be modified to reproduce the experimental B(E2) values. In fact, the stability of the calculated B(E2) seems to suggest the lacking of some elements in the nuclear models applied in this region.

5.2.4 The puzzle of B(E2) values: the role of the $\mathbf{j}_{15/2}$

One objection to these calculations could be due to the single particle energy used for the $\nu j_{15/2}$ orbital. It is extracted from the energy of the $15/2^-$ level in ^{209}Pb, but the spectroscopic factor of this state is about half that of its *bona fide* single-particle value, due to a strong mixture of the $j_{15/2}$ shell with the $g_{9/2} \otimes 3^-$ configuration [111, 112]. If half of the spectroscopic strength is assumed to be at about 3.5 MeV [113], then a 1 MeV shift of the single particle energy is a reliable estimation of its actual value. When this is applied in the calculations, the excitation spectra change by no more than 50 keV, but the disagreement with the B(E2) rates decreases, though not completely, as it is evident from Fig. 5.10. However, other problems arises, such as the tendency of the B(E2) of 4^+ state in ^{214}Pb to go to zero, making it a long-lived isomeric state not observed experimentally.

5.2.5 Seniority-mixing and core-breaking effects

Seniority mixing The seniority is not a good quantum number when the total angular momentum of the nucleons is larger than 7/2, and it is certainly violated when more orbitals are occupied, as in the present case. As discussed in the previous section, the quadrupole transition strength between states of different seniority is large and thus even small mixing in the wave function can significantly change the final B(E2) value. In this specific case the 6^+ states with seniority 4 generate transition quadrupole matrix elements from the 8^+ isomer with opposite sign with respect to the seniority 2 states. The

destructive interference can easily lower the calculated B(E2) by the factor four needed to match the experimental data. On the other hand, the mixing of the $\nu = 4$ configuration in ^{214}Pb can increase the very small calculated B(E2), restoring the agreement with the measured value. However, changing the seniority mixing, even by a small amount, means playing with the multipole part of the interactions, in particular a significant modification of the pairing matrix elements is required. From the consideration written above, these adjustments cannot be justified and would appear quite arbitrary.

Core breaking From the considerations made so far, it appears quite evident that there is some physics lacking in the model used to describe the structure of the neutron-rich lead nuclei. All the shell model calculations presented so far were performed in a pure neutron valence space above the closed shells N = 126 and Z = 82. However, it is also possible to consider the breaking of the doubly-magic ^{208}Pb core, by allowing neutrons and protons to be excited from shells below N = 126 and Z = 82 to the valence space above. A full diagonalization in this space is not feasible, but the first step of a full perturbative treatment will provide hints on what may be the physical processes causing the observed discrepancies. This will be discussed in the following sections.

5.2.6 Core excitations and effective three-body forces

In order to introduce the concept of effective three-body forces, it is useful to start from a different point of view on the perturbative treatment for the study of nuclear structure. Instead of applying the perturbation theory to the operators involved in the problems, it is the wave function that is developed in a perturbative manner. The idea is to start from a bare many-body state and then dress it, giving origin to a quasiconfiguration [114, 115]. The quasiconfiguration method originates from the idea to separate a full space into a model (or valence) part containing states $|v\rangle$ and an external one made of states $|e\rangle$. The $|v\rangle$ and $|e\rangle$ are then dressed through a transformation [93]:

$$|\bar{v}\rangle = |v\rangle + \sum_e A_{ve}|e\rangle \tag{5.11}$$

$$|\bar{e}\rangle = |e\rangle + \sum_i A_{ve}|v\rangle \tag{5.12}$$

where the dressed states $|\bar{v}\rangle$ and $|\bar{e}\rangle$ are orthogonal and the coefficients A_{ve} are defined by the condition:

$$\langle\bar{v}|H|\bar{e}\rangle = 0 \tag{5.13}$$

This technique allows one to make analytic calculations, and, as it is shown below, it transforms the dressing of the states into the dressing of the operators.
Let the bare orbit above a closed core configuration be called f (it is the model part v of the valence space), and let it be only partially occupied. The external orbits e

can be either part of the closed core, whose shell(s) is called h, or an empty orbit lying above, p. If the f^n configuration is assumed to be a good model space, its dressing with particle-hole excitations is the first order perturbative step. The following process is an example of such excitations:

$$f^n \xrightarrow[W_{fhff}]{} f^{n+1}h^{-1} \xrightarrow[W_{fffh}]{} f^n$$

where W_{fffh} and W_{fhff} are the matrix elements connecting different states. Other common cases of dressing with particle-hole excitations are the core polarization:

$$f^n \xrightarrow[W_{fhfp}]{} f^n ph^{-1} \xrightarrow[W_{fpfh}]{} f^n$$

or the pairing:

$$f^n \xrightarrow[W_{hhff}]{} f^{n+2}h^{-2} \xrightarrow[W_{ffhh}]{} f^n$$

As a consequence, the bare f^n configuration is dressed as:

$$|\overline{f^n}i\rangle = |f^n i\rangle + \frac{1}{\varepsilon_{iJ}}|f^{n+1}h^{-1}J\rangle\langle f^{n+1}h^{-1}J|W_{fffh}|f^n i\rangle \tag{5.14}$$

where i, J are the necessary quantum numbers to completely define the state and ε_{iJ} is the energy of the unperturbed state. An hamiltonian matrix element is thus calculated as:

$$\begin{aligned}\langle\overline{\overline{f^n}}i|H|\overline{\overline{f^n}}i'\rangle = \langle f^n i|H|f^n i'\rangle + \sum W_{f_1hf_2f_3}W_{f_4f_5f_6h} \times \\ \times \frac{1}{2}\left(\frac{1}{\varepsilon_{iJ}} + \frac{1}{\varepsilon_{i'J'}}\right)\langle f^n i|a^\dagger_{f_1}a^\dagger_h a_{f_2}a_{f_3}|f^{n+1}h^{-1}J\rangle\langle f^{n+1}h^{-1}J|a^\dagger_{f_4}a^\dagger_{f_5}a_{f_6}a_h|f^n i\rangle\end{aligned} \tag{5.15}$$

where the sum extends to all the magnetic substates f_k relevant for the intermediate configurations. The dressed $\overline{\overline{f^n}}$ states are orthonormalised. If the energy denominators $\varepsilon_{i'J'}$ are assumed to be constant over all sets of intermediate states [115], it is possible to rewrite the matrix element, using the Wick's theorem to bring operators in the normal order and to introduce the diagrammatic representation, as:

$$\langle\overline{\overline{f^n}}i|H|\overline{\overline{f^n}}i'\rangle = \langle f^n i|H|f^n i'\rangle + \langle f^n i|\omega_1 + \omega_2 + \omega_3|f^n i'\rangle \tag{5.16}$$

with:

$$\begin{aligned}\omega_1 &= -\sum \frac{1}{\varepsilon}a^\dagger_{f_1}a_{f_6}W_{f_1hf_2f_3}W_{f_3f_2f_6h} \\ \omega_2 &= -\sum \frac{1}{\varepsilon}a^\dagger_{f_1}a^\dagger_{f_5}a_{f_2}a_{f_6}W_{f_1hf_2f_3}W_{f_3f_5f_6h} \\ \omega_3 &= -\sum \frac{1}{\varepsilon}a^\dagger_{f_1}a^\dagger_{f_4}a^\dagger_{f_5}a_{f_2}a_{f_3}a_{f_6}W_{f_1hf_2f_3}W_{f_4f_5f_6h}\end{aligned} \tag{5.17}$$

Therefore, the dressing of the bare f^n state generates a quasiconfiguration that represents the space in which the Hamiltonian H is diagonalised, ignoring the external degrees of freedom. From Eq. 5.17, one can see that the perturbative process at the lowest order already generates one- (ω_1), two- (ω_2) and three-body (ω_3) effective terms which add to the original Hamiltonian. The fact that, already at the lowest orders, three-body effective forces appear should be a warning against the common practice of ignoring them, as it will be shown for the even-even lead nuclei. In Fig. 5.11 the diagrammatic representation of the different terms in Eq. 5.17 is provided, pointing out the nature of the effective three-body force.

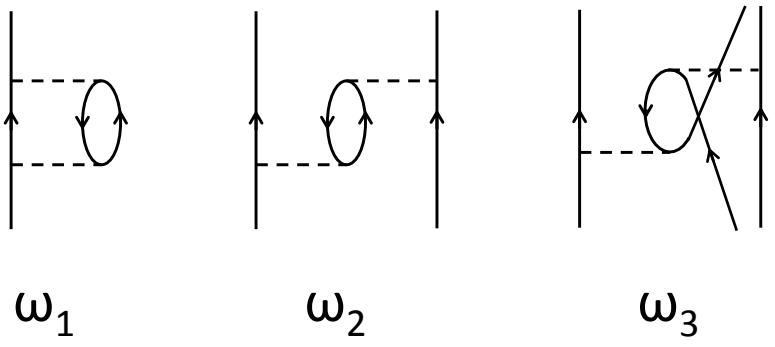

Figure 5.11: The diagrammatic representation of the lowest order dressing of the bare wave function. The open lines correspond to valence orbits v. The interaction lines are associated to matrix elements W_{veve} or W_{vvve} where e are the external orbits.

Besides the dressing of the wave function, also the operators have to be dressed, becoming effective operators. An operator Q of the form:

$$Q = \sum_{r \leq s} Q_{rs}(a_r^\dagger a_s + a_s^\dagger a_r)$$

where r, s are the indexes representing the different p, h, f shell mentioned above. It becomes, following the same procedure used for the wave function:

$$\langle \overline{\overline{f^n}} i | Q | \overline{\overline{f^n}} i' \rangle = \langle f^n i | Q | f^n i' \rangle + \langle f^n i | q_1 + q_2 | f^n i' \rangle \tag{5.18}$$

The operators q_1, q_2 are the one- and two-body terms, respectively:

$$\begin{aligned} q_1 &= -\sum \frac{Q_{f_1 h}}{\varepsilon} W_{f_1 f_2 f_3 h}(a_{f_3}^\dagger a_{f_2} + (a_{f_2}^\dagger a_{f_3}) \\ q_2 &= -\sum \frac{Q_{fh}}{\varepsilon} W_{f_2 f_3 f_4 h}(a_{f_1}^\dagger a_{f_4}^\dagger a_{f_2} a_{f_3} + a_{f_2}^\dagger a_{f_3}^\dagger a_{f_1} a_{f_4}) \end{aligned} \tag{5.19}$$

They also have a diagrammatic representation shown in Fig. 5.12.

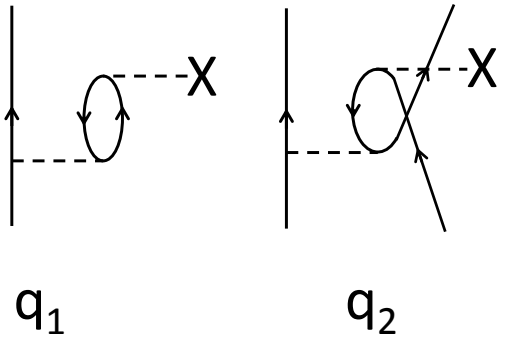

Figure 5.12: The diagrammatic representation of the effective operator Q showing the one- (q1) and two-body (q2) terms.

5.2.7 Effective three-body forces: B(E2) values of the lead isomers

The following discussion focusses on the results obtained when the effective three-body terms are considered for to calculate the B(E2) strenghts for the neutron-rich lead isotopes. Since the shell model codes used (ANTOINE, NATHAN) only permit to perform two-body calculations, the only possibility of including the effect of the ω_3 term is to explicitly introduce the process of particle-hole excitation discussed above. In fact, in this way the expectation value of the Hamiltonian and of the transition operators is calculated directly between the dressed wave functions, thus also including the many-body terms otherwise neglected.
As the B(E2) strength from the isomeric state involves the quadrupole operator, the most relevant shells from the core to be included are the ones linked in the quasi-SU3 scheme [12]. If the quadrupole operator is defined, separating angular and radial dependence, as $q^{20} = r^2 C^{20}$, than the angular part C^{20} has matrix elements:

$$\langle jm|C^2|j+2m\rangle \approx \frac{3[(j+3/2)^2 - m^2]}{2(2j+3)^2} \tag{5.20}$$

$$\langle jm|C^2|j+1m\rangle \approx \frac{3m[(j+1)^{1/2} - m^2]}{2j(2j+2)(2j+4)} \tag{5.21}$$

It is evident that the quadrupole strength is large for shell with $\Delta j = 2$, whereas it is small for $\Delta j = 1$, and the latter can thus be neglected. Therefore, for neutrons the $i_{13/2}$ will couple to the $g_{9/2}$, and for protons the $h_{11/2}$ will couple to the empty $f_{7/2}$ orbital above Z = 82. Consequently, the calculations were performed by dressing the $g_{9/2}$ shell with particle-hole excitations to/from the following shells:

- $i_{13/2}$ and $h_{11/2}$ below the closed N = 126 and Z = 82 cores, respectively
- $i_{11/2}, d_{3/2}, d_{5/2}, g_{7/2}, s_{1/2}, j_{15/2}$ above the N = 126 core, and $f_{7/2}$ above the Z = 82 core.

These particle-hole excitations from the core consist of excitations at 0 or $1\hbar\omega$ (as the 2^+ and 3^- in ^{208}Pb) or $2\hbar\omega$ (giant quadrupole resonance) that affect all model spaces and lead in particular to the standard effective charges $e_\nu = 0.5e$, $e_\pi = 1.5e$ [93]. Concerning the coupling to the 3^- state, it affects the $g^n_{9/2}$ bare wave function only indirectly in higher order perturbation theory. Therefore, only the two-body effective contributions included in the interaction will be taken to represent the octupole coupling. On the contrary, the 2^+ "phonon" couples directly to the dominant $g^n_{9/2}$ configuration in second order through the very specific $\Delta j = 2$ particle-hole jumps responsible for quadrupole coherence [12, p. 463], as stated above. Their effects are important and are estimated using the Kahana Lee Scott (KLS) interaction [93] calculated at $\hbar\omega = 7$ MeV and multiplied by the overall factor of 1.3 for all matrix elements except for the $JT = 01$ ones (pairing), whose factor is set at 1.5. This ensures correct quadrupole and pairing strengths coming from the $2\hbar\omega$ (giant quadrupole resonance) jumps [93]. KLS is an old realistic potential, whose matrix elements are identical to the most modern ones with a 96% overlaps [93, 12] or better. Simple diagonalizations including these jumps are no substitute for a full perturbative treatment but give indications of what could be expected, regarding in particular the restoration of the observed seniority regularities. The final results are given in Fig. 5.13, which compares the experimental data for the E2 strengths with the calculations. The theoretical values for the other states of the cascade to the ground state and the sign of the quadrupole moments Q are also given for comparison.

Case A (red dashed line) corresponds to the bare single-shell $\nu g^n_{9/2}$ space in which the pairing matrix element has been made more attractive to reproduce the 2^+ energy. Particle hole conjugation symmetry between pairs $^{210-216}$Pb and $^{212-214}$Pb is obviously valid. Case B (green dashed-dotted line) includes single jumps from $g_{9/2}$ to shells above. It should be viewed as a rough simulation of the exact diagonalization. Case C (blue dotted line) is as B plus the coupling to the 2^+ excitation from the core, and thus it also includes the three-body effective forces shown in Fig. 5.11. In cases B and C the pairing matrix element is maintained as in case A and taken to be representative of the two-body renormalisation. Effective charges are the standard $1.5e$ and $0.5e$ for protons and neutrons, respectively. The important trend that emerges is that in case C the transition rates nearly double with respect to B, which corresponds to e_ν going roughly from $0.5e$ to $0.7e$, not far from the $0.8e$ adopted in Fig. 5.10. However, in case B, without excitations from the core, the need for state-dependent effective charges shows clearly, in particular through the breakdown of conjugation symmetry around midshell. The explicit inclusion of core excitation in case C restores the regular behaviour, in $g_{9/2}$ dominance, experimentally observed for the $8^+ \to 6^+$ transitions. Although the

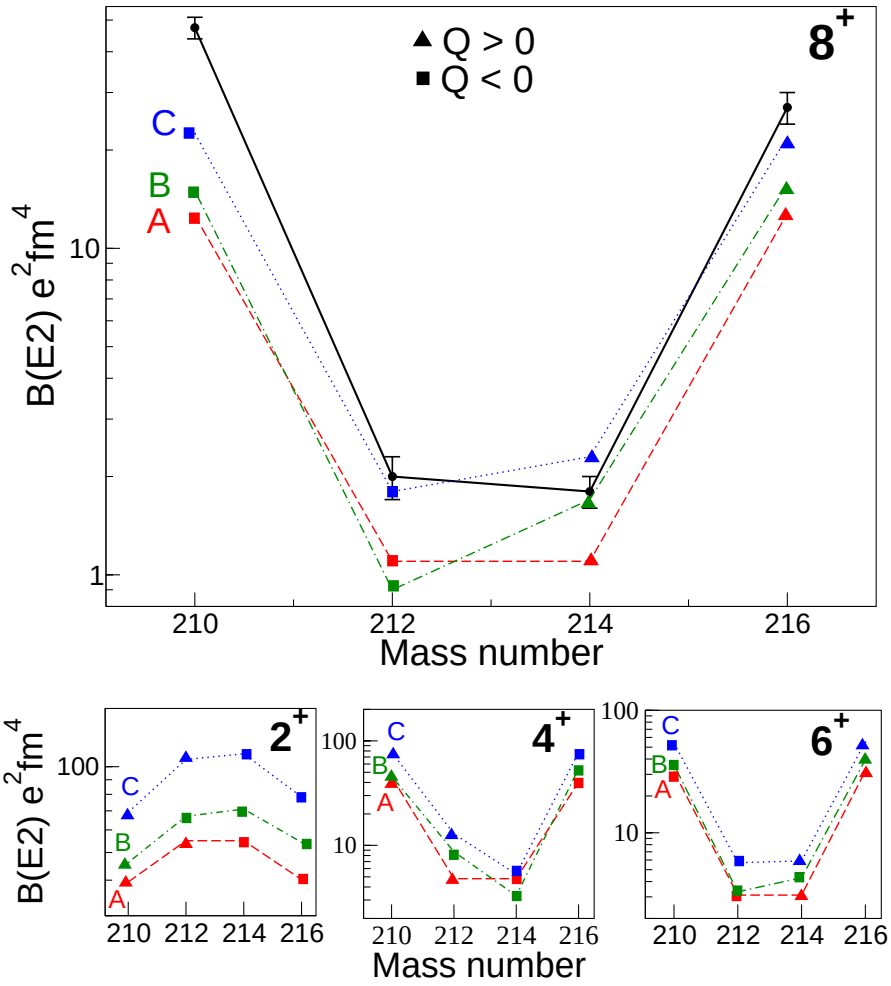

Figure 5.13: Transition rates and sign of the quadrupole moments for the even-even Pb isotopes. Diagonalizations are made in the following spaces: case A (red line, dashed) $\equiv g^n$; case B (green line, dot-dashed) $\equiv g^n+g^{n-1}r$; case C (blue line, dotted) $\equiv g^n+g^{n-1}r+g^n([h^{-1}_{11/2}f_{7/2}]_\pi+[g\ i^{-1}_{13/2}]_\nu)$. Definitions of shells: $g \equiv g_{9/2}$, $r \equiv i_{11/2}d_{3/2}d_{5/2}g_{7/2}s_{1/2}$. The experimental data are plotted with a black continuous line for eye guidance.

B(E2) from the other states are not measured, the restoring of a symmetric parabolic behaviour in case C also for them strengthens the result for the isomeric decay B(E2). The anomalous behavior of the $4^+ \rightarrow 2^+$ transition is anyway a puzzle. Note that the sign of the quadrupole values in C is coherent with A, very much in line with the restoration of symmetry in the B(E2) values. Therefore, the inclusion of the quadrupole coupling and its related three-body effective forces (the diagrams in Fig. 5.11) goes in

the direction of improving the agreement with the experimental data. It also shows the origin of the effective charge $0.8e$ used in a pure neutron space, and gives hints to the need of state-dependent effective charges if one restricts himself to this space. The problem of reproducing the correct ratio between the B(E2) of ^{210}Pb and ^{212}Pb is not completely solved, but significantly reduced in magnitude.
The results of the calculations for transition rates turn out to be a delicate balance between different effects that tend to break and restore the $g^n_{9/2}$ dominance, which is reaffirmed by the quadrupole couplings and their related three-body effective force just studied. Nevertheless, the result is the regular seniority-like behaviour observed: *natura nihil frustra facit*. Further experimental work in this region is imperative to better assess the role of effective three-body terms, and a fully perturbative treatment of the problem is needed, in particular with respect to the coupling to the octupole core excitation.

5.2.8 Calculations for the ^{218}Pb isotope

In Chapter 4 it was shown that there is no evidence of isomeric states in ^{218}Pb within the observational limits. Shell-model calculations have been performed with NATHAN to see whether the non existence of an isomer is predicted by the KH interaction. The pure neutron valence space is the same already used for the other even-even lead isotopes, with the exception of the $g_{7/2}$ shell which was excluded to make the calculation feasible. The neglecting of this shell should not significantly influence the results, since it is quite distant in energy from the $g_{9/2}$ orbital and thus it is almost not involved in the nuclear wave function. For the same computational limitations, the number of broken nucleon pairs was also restricted to four (five is the maximum possible, as there are ten neutrons in the valence space). Figure 5.14 presents the theoretical results. The level scheme is very similar to the other neutron-rich even-even lead nuclei, with a low-energy $8^+ \rightarrow 6^+$ transition. The B(E2) predicted for this transition, with effective charge $e_\nu = 0.8$, is 38 e^2fm^4. Consequently, there should be a 8^+ isomer with an half life of about 200 ns. The non observation of this isomeric state suggests that the KH interaction may have problems in reproducing the nuclear structure when going far from stable nuclei.

5.3 Calculations for the odd-even lead isotopes

The odd-even lead isotopes ^{211,213,215}Pb should also follow the seniority scheme in the $g_{9/2}$ shell. The seniority isomers are expected to originate from a state with a spin-parity $21/2^+$, the maximum possible alignment of three nucleons in this orbit. ^{211}Pb was studied in the past exploiting deep-inelastic reactions, confirming the existence of such an isomer. Figure 5.15 shows the shell model calculations for the odd-even neutron-rich lead nuclei, and the experimental levels of ^{211}Pb are reported for comparison. The valence space is the same used for the even-even lead isotopes, and the interaction used is the KH. The results for ^{211}Pb agree very well with the experimental data. The theoretical

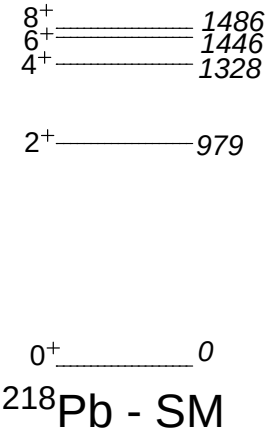

Figure 5.14: Shell-model calculation with the KH interaction for the ^{218}Pb isotope.

calculations also confirm the seniority scheme as the level energies of the three isotopes remain roughly constant.

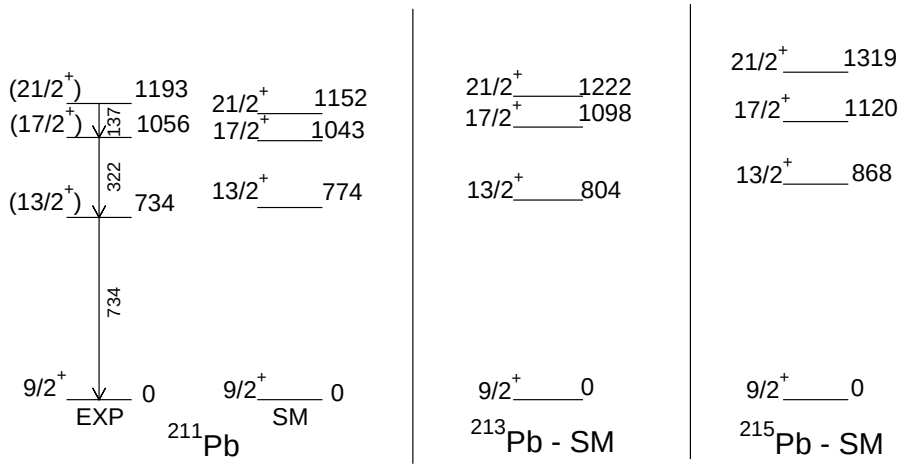

Figure 5.15: Shell-model (SM) calculations with the KH interaction for the odd-even lead isotopes. The experimental levels of ^{211}Pb are reported for comparison.

Using a neutron effective charge state $e_\nu = 0.8$, the calculated B(E2) from the isomer state of ^{211}Pb is 87 e^2fm^4, in fair agreement with the experimental value of 104 ± 18 e^2fm^4 [48].

The nucleus ^{213}Pb The KH interaction indicates that a "standard" seniority scheme is expected for the excitation spectrum of ^{213}Pb, but this does not correspond with what observed experimentally in Fig. 4.17. As discussed in the previous chapter, the analysis of coincidences shows that the 772- and 488-keV transitions belong to the same cascade, but the 772 keV transition has higher intensity, which means that it should receive some feeding from other isomeric states. To assign these two transitions to the cascade from the seniority isomer (488 keV: $17/2^+ \rightarrow 13/2^+$, 772 keV: $13/2^+ \rightarrow 9/2^+$) would be quite natural, since the energies are not far from those predicted by the shell model. However, it is not clear the role of the other two transitions observed. It may be that the fragmentation reaction is populating other isomeric states that then decay to the $13/2^+$ state. It would have been interesting to perform isomer decay spectroscopy also in ^{211}Pb: its level scheme is quite well known and the observed isomers would have given indication on what to expect for heavier fragments. This nucleus was however excluded from the acceptance of the FRS, due to the primary-beam charge-state problem already discussed in Chapter 3.

The nucleus ^{215}Pb No isomer was observed in ^{215}Pb. This is in agreement with the shell-model calculations which predict a transition of 199 keV depopulating the $21/2^+$ isomer. This γ ray is not strongly converted; moreover, the predicted B(E2) from the isomer is 49 e^2fm^4. As a consequence, the theoretical results are consistent with the experimental finding that the lifetime of the seniority isomer is below 10 ns, taking also into account that the isomer would partially decay already along the FRS flying path (around 300 ns).

5.4 Calculations for the bismuth isotopes

The level scheme of ^{217}Bi can easily be interpreted as the coupling of the unpaired proton in the $h_{9/2}$ orbital with the states of ^{216}Pb. As a result its level scheme, as well as those of the whole chain of even-odd Bi isotopes $^{211-217}$Bi, follows the seniority scheme in the $g_{9/2}$ shell. In the following, a comparison with shell-model calculations using the KH interaction is presented. The neutron valence space above the shell closure N = 126 is the same used for the lead isotopes, while the proton valence space above Z = 82 is constituted by the shells: $1h_{9/2}$, $2f_{7/2}$, $2f_{5/2}$, $1i_{13/2}$. The orbitals $2p_{3/2}$ and $2p_{1/2}$ have been excluded to reduce an otherwise too large configuration space, but it was checked that their effect on the final results is not important in ^{211}Bi, where a calculation with the whole valence space is feasible. The proton single-particle energies have been extracted from the spectrum of ^{209}Bi.
Figure 5.16 shows the results of the shell-model calculations with the NATHAN [108, 109] code and the experimentally known levels of bismuth isotopes. The agreement is very good in all cases. As for the lead isotopes, a stringent test is offered by the comparison

of the calculated E2 strengths with the experimental ones extracted from the isomer lifetime. This is possible only for ^{211}Bi [39] and ^{217}Bi, as in ^{213}Bi [89] no isomeric state is known and in ^{215}Bi [49] the isomeric state is not a seniority isomer, being instead originated by the inversion of the $25/2^-$ state with the $27/2^-$ or the $29/2^-$ state.

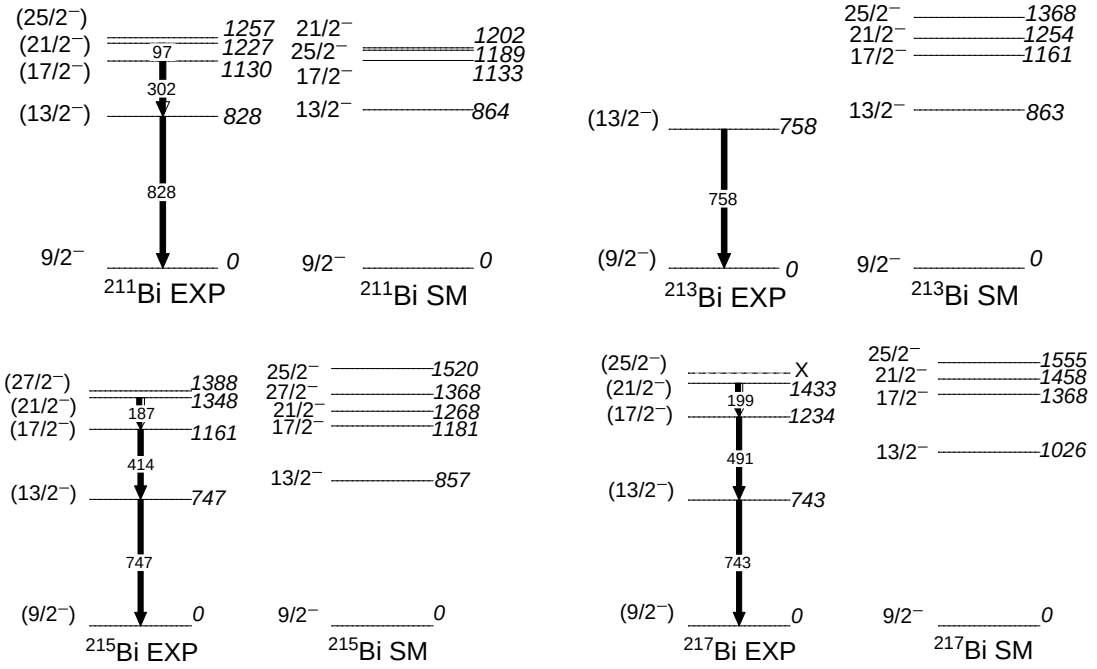

Figure 5.16: Experimental and calculated level schemes for the odd-even bismuth isotopes. The calculations were performed using the KH interaction. The ^{217}Bi level scheme is deduced from the present work.

The experimental B(E2) for ^{211}Bi is 8(2) e^{2}fm^4 [39], while for ^{217}Bi ranges from 3.6(1) e^{2}fm^4 to 5.2(1) e^{2}fm^4. The calculated B(E2) values, with effective charges $e_\nu = 0.8$ and $e_\pi = 1.5$, are 92 e^{2}fm^4 and 1.0 e^{2}fm^4 for ^{211}Bi and ^{217}Bi, respectively. These values of the effective charges are adopted considering that the calculations are performed in the KH valence space, with no ^{208}Pb core breaking. In a pure seniority scheme in the $g_{9/2}$ shell one would expect the two experimental strengths of ^{211,217}Bi to be the same, instead the measured B(E2) differ by a factor two. However, this is not a significant discrepancy, as a similar difference was also observed ^{210,216}Pb, due to the role play by the other valence neutron shells. On the contrary, the comparison of the measured values with the KH calculation reveals a large disagreement: the predicted B(E2) values are, in ^{211}Bi, more than an order of magnitude larger. This cannot be justified by a readjustment in the effective charges of protons or neutrons, and demands further theoretical investigation, including also in this case effective three-body forces.

5.5 Calculations for the thallium isotopes

In order to perform shell-model calculations for isotopes beyond N = 126 but below lead one needs an interaction containing both the neutron valence space of KH and the proton space below Z = 82. The model space considered includes the neutron orbitals $2g_{9/2}$, $1i_{11/2}$ and $1j_{15/2}$ above the N = 126 shell closure and the proton shells $2d_{5/2}$, $2d_{3/2}$, $h_{11/2}$ and $3s_{1/2}$ below the Z = 82 core. No excitations across the ^{208}Pb core are thus allowed. The neutron-neutron and proton-proton matrix element are from the KH interaction, while the proton-neutron matrix elements have been deduced from the bare H7B G matrix [116], without core polarization, as explained in Ref. [117]. The only change made to the hamiltonian is to increase the matrix element $(\nu g_{9/2})^2_{8^+}$ by 40 keV to get the correct ordering of 6^+ and 8^+ in ^{208}Hg, as suggested in Ref. [50]. Therefore, the wave functions of the holes in the proton core will mainly be constituted by the $s_{1/2}$ and $h_{11/2}$ orbits, while the particle wave function for neutrons will be dominantly $(g_{9/2})^n$, as in the case of lead isotopes. In Fig. 4.27 of Chapter 4 it was shown, for ^{209}Tl, the comparison between shell-model calculations using this interaction and the experimental data from Ref. [50]. As claimed in the quoted paper, the agreement is quite good for both energies and B(E2). Figure 5.17 reports our calculation performed with NATHAN [108, 109]: the small differences with respect to those of Ref. [50] are due to the numerical approximations. The model space used is a particle space for neutrons above N = 126 and a one-hole space for protons below Z = 82. The calculated B(E2) from the isomeric $17/2^+$ state is 244.5 e^{2}fm^4, identical to the value reported in Ref. [50], and well compatible with the experimental value. ^{209}Tl is, in fact, the one-proton hole counterpart of ^{210}Pb, and its isomer results, with 94.5 % probability, from the coupling between the lead isotope 8^+ isomer and the unpaired proton hole in $s_{1/2}$.
The spectra we obtain for $^{211-213}$Tl are anyway quite different from that of ^{209}Tl, and in the next section we will discuss if the difference can be explained by shell-model calculations.

5.5.1 Calculations for the ^{211}Tl isotope

Only one γ line at 144 keV is observed in the spectrum of ^{211}Tl, indicating the presence of at least one isomer, with an half life of 0.58 ± 0.03 μs. At first sight, within the framework of the seniority-scheme, one could suggest that the observed transition corresponds to $13/2^+ \rightarrow 9/2^+$, since in ^{209}Tl it has a very similar energy of 137 keV. It is then possible that the transitions between the lower energy levels are not observed because the 144 keV line is feeding an isomer with a long lifetime outside the range of our experiment.
The shell-model calculation is performed in the same model space as in the case of ^{209}Tl, and the resulting levels are shown in Fig. 5.18. The $17/2^+$ level is isomeric as in ^{209}Tl, due to the low energy of the E2 transition to the $13/2^+$ state. The calculated B(E2) is 34.5 e^{2}fm^4 using $e_\pi = 1.5$ and $e_\nu = 1$. The effective charge of neutrons is increased

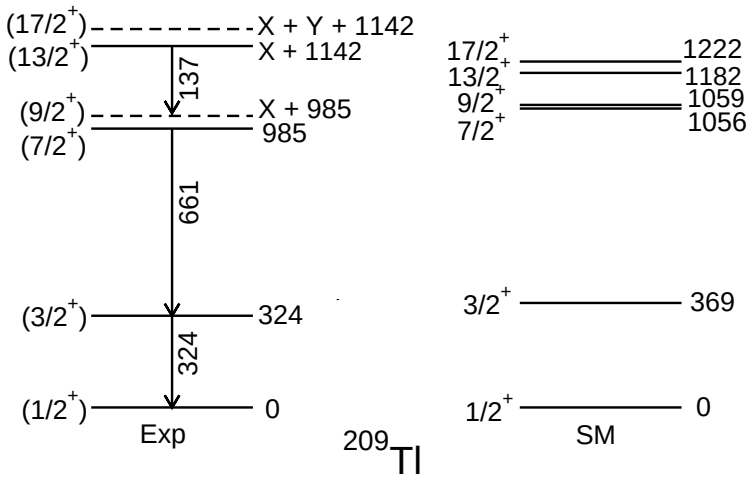

Figure 5.17: Experimental [50] and theoretical level scheme of ^{209}Tl.

from 0.8 to 1 because the neutron valence space has been reduced to only three shells for thallium isotopes, to make the calculations feasible. The $13/2^+ \rightarrow 9/2^+$ transition is possibly the 144 keV γ line observed. In ^{209}Tl the $9/2^+$ then decays via a mainly M1 transition to the $7/2^+$ state: the calculation suggests that in ^{211}Tl the $7/2^+$ level is higher than $9/2^+$, which thus can only decay to the $3/2^+$ state. This would be an E4/M3 transition, highly hindered due to its high multipolarity. For a M3 character with an energy of 900 keV its Weisskopf single-particle estimate leads to a lifetime of 160 μs, while for an E4 character the estimate is 153 ms. This means that the lifetime for an E4 transition is outside the observational limit of the experimental setup. A factor 10 of hindrance of the M3 strength would be sufficient to make it unobservable. It is difficult to estimate M3 and E4 strengths with shell-model codes, since the parameters for these cases are not well known, differently from the case of M1 or E2 transitions.
Nevertheless, if this interpretation is correct, one can compare the calculated B(E2) from the isomeric $17/2^+$, 34.5 e^{2}fm^4, with the measured one, which ranges between 35(2) and 24(1) e^{2}fm^4. The agreement is remarkable, reinforcing our interpretation of the nature of the observed isomer.

5.5.2 Calculations for the ^{213}Tl isotope

The spectrum we obtain for ^{213}Tl is different from both ^{209}Tl and ^{211}Tl, showing only a single strong γ line of 380 keV, and another weaker line at 698 keV. In terms of a seniority scheme, it is possible that the 380 keV line corresponds to the $3/2^+ \rightarrow 1/2^+$ transition observed with a similar energy in ^{209}Tl. The 698 keV could then be the $9/2^+ \rightarrow 3/2^+$ γ ray, but its low intensity and the fact that it is not in coincidence with the 380 keV line

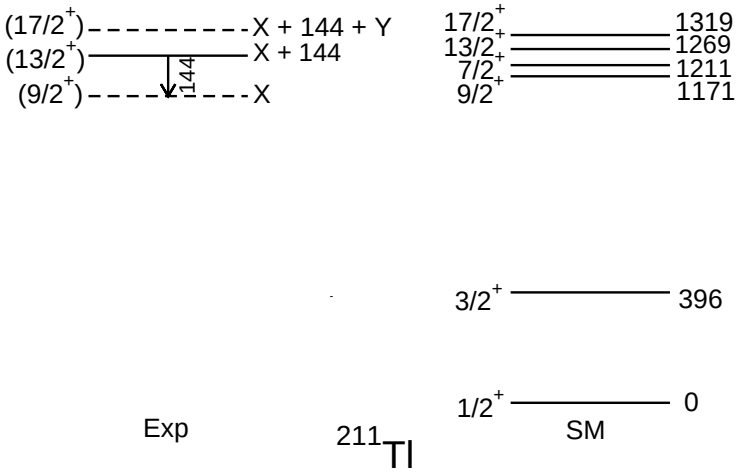

Figure 5.18: The proposed experimental level scheme of ^{211}Tl compared with shell-model calculations performed with the interaction and valence space from Ref. [50].

implies that it is either a contamination or a γ ray connecting other two levels, following another isomer.
We have however performed shell-model calculations also for this nucleus. Figure 5.19 shows the calculated levels scheme, which is very similar to the one obtained for ^{211}Tl. With our data it is difficult to reach any conclusion, besides the presence of an isomer also in ^{213}Tl.

5.6 Calculations for the mercury isotopes

Mercury isotopes are also discussed within a shell-model framework. The interaction is the same used for the thallium isotopes, as well as the valence space which includes the $2g_{9/2}$, $1i_{11/2}$ and $1j_{15/2}$ orbitals above the N = 126 shell closure and the $2d_{5/2}$, $2d_{3/2}$, $1h_{11/2}$ and $3s_{1/2}$ proton orbitals below the Z = 82 core. In the following sections the comparisons with our shell-model calculation will be provided.

5.6.1 Calculations for the ^{208}Hg isotope

In Chapter 4, the calculations for the ^{208}Hg nucleus from Ref. [50] were reported. In Fig. 5.20 we present our calculations using the codes ANTOINE, NATHAN [108, 109]. The calculated B(E2), 96 e^{2}fm^4, is identical to the one reported in Ref. [50], which is also in excellent agreement with the measured data. Similarly to ^{209}Tl, ^{208}Hg is the two proton-hole counterpart of ^{210}Pb, where the shell-model estimates for electromagnetic strength are in very good agreement with the experiment. This could imply that the two proton

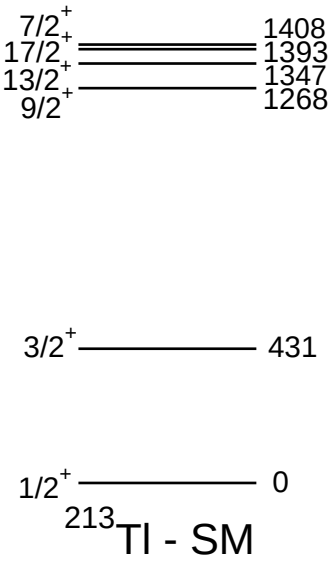

Figure 5.19: Shell-model calculations for ^{213}Tl, performed with the interaction and valence space from Ref. [50].

holes, mainly in $s_{1/2}$ wave function, are just "spectators", while the active parte of the wave function is given by the two neutrons outside the N = 126 core.

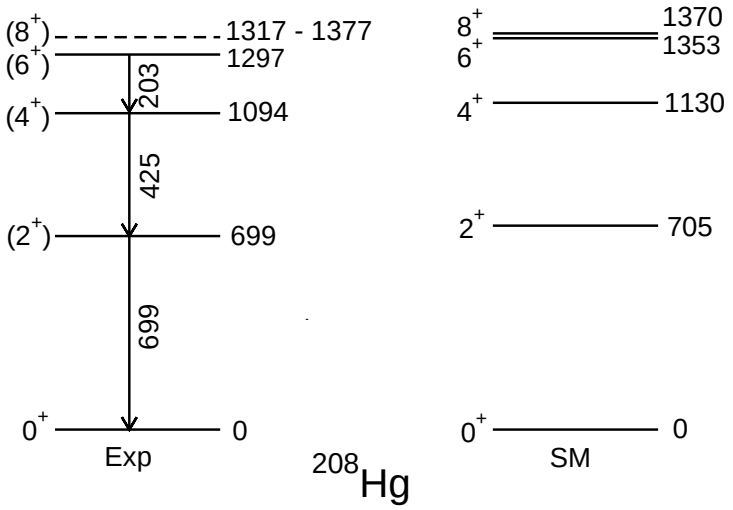

Figure 5.20: Experimental level scheme of ^{208}Hg [50] compared with shell-model calculations performed with the interaction and valence space from Ref. [50].

5.6.2 Calculations for the ^{210}Hg isotope

The experimental spectrum of ^{210}Hg shown in Fig. 4.38 is different from the one of ^{208}Hg as well as from that of the even-even lead isotopes. The level scheme we propose is presented in Fig. 5.21. Reference [118] reports calculations showing that the ^{210}Hg isotope has an almost spherical shape, as ^{208}Hg. Whereas the γ-ray cascade from an isomeric 8^+ state (of which we observe only the $6^+ \rightarrow 4^+ \rightarrow 2^+ \rightarrow 0^+$ part) is expected from the systematics and the seniority scheme, the possible presence of an isomeric 3^- or 2^+ state at low-energy is quite unusual for an almost spherical nucleus. The comparison of the experimental findings with shell-model calculations is presented in Fig. 5.21. The results (in black lines) of theoretical predictions are obtained with the codes ANTOINE, NATHAN [108, 109], and using the same interaction and valence space already exploited and proven valid for ^{208}Hg. The yrast sequence $8^+ \rightarrow 6^+ \rightarrow 4^+ \rightarrow 2^+ \rightarrow 0^+$ is the same as in the other even-even lead and mercury isotopes. The $4^+ \rightarrow 2^+$ transition becomes of comparable energy with respect to the $2^+ \rightarrow 0^+$ γ ray, in agreement with the calculations. Also the other level energies of the yrast sequence seem to be well reproduced. From this point of view, ^{210}Hg appears as the two-proton hole partner of ^{212}Pb, and the validity of the canonical seniority scheme in the $g_{9/2}$ shell is upheld. However, the intensity of the detected γ rays and their coincidence matrix clearly shows that the 2^+ level is fed by another, non observed transition. The fact that the feeding branch is not detected means that it is low in energy[1] and thus at least partially converted. Due to the fact that the lifetime derived from the $2^+ \rightarrow 0^+$ transition is compatible with the one from the $4^+ \rightarrow 2^+$ γ ray, one can conclude that the feeding of the first 2^+ proceeds from a state whose lifetime is of the order of a μs. This restricts the possible multipolarity of the feeding to E1, E2, M1 or E3 character. Considering the internal conversion coefficient, the γ efficiency and setting 10 counts as the observational threshold, the upper energy limit would be 90 keV, 170 keV, 250 keV and 290 keV, for E1, E2, M1, E3 character, respectively. A possibility would be that the state at 663 keV decays to the 2^+ state via a 20-keV transition which is within the aforementioned limits. Moreover, no other line has been observed in coincidence with the 663-keV γ-ray. Taking into account that the lifetime of this transition is also of the order of 1 μs, the most intuitive assumption would be a 3^- spin-parity assumption, because the Weisskopf lifetime estimate of a 663-keV E3 transition is 0.34 μs. The decay to the 2^+ would then have a E1 character: a E1 transition of 20 keV has a lifetime of 4.5 ps, according to the Weisskopf estimates. This would then correspond to an E1 transition suppressed by a factor about 10^5. The presence of a 3^- at only 663 keV is unlikely: although there are nuclei with 3^- levels at low energies (few hundreds keV), as in the actinide region, in ^{208}Pb the octupole excitation lies 2.6 MeV, decreasing to 1.9 MeV and 1.8 MeV in $^{210-212}$Pb, respectively. Furthermore, particle-vibration coupling models predict it around 1.3 MeV in N = 130

[1] In principle, it could also be impossible to detect because the energy is above 4 MeV, which is the upper energy visible by RISING. However, this possibility is less likely, and thus not discussed here.

nuclei [119]: see Fig. 5.21 where the theoretical 3^- level is plotted in red. The 3^- assignment can thus be regarded as quite improbable. Another possibility is that the 663 keV is a second 2^+ level, decaying with a highly-converted M1/E2 transition to the first 2^+. This assignment however arises four questions:

- The 20 keV transition to the first 2^+ would be quite fast if mainly or only M1: 24 ps according to Weisskopf estimate.
- The E2 663 keV transition to the ground state should be a very hindered B(E2) to give a lifetime of around 1 μs
- There are no evidences in the Segrè chart of nuclei with a second 2^+ at only 20 keV above the first one, especially in nuclei which are not deformed.
- The second 2^+ is predicted at much higher energy by the shell-model calculations, see Fig. 5.21.

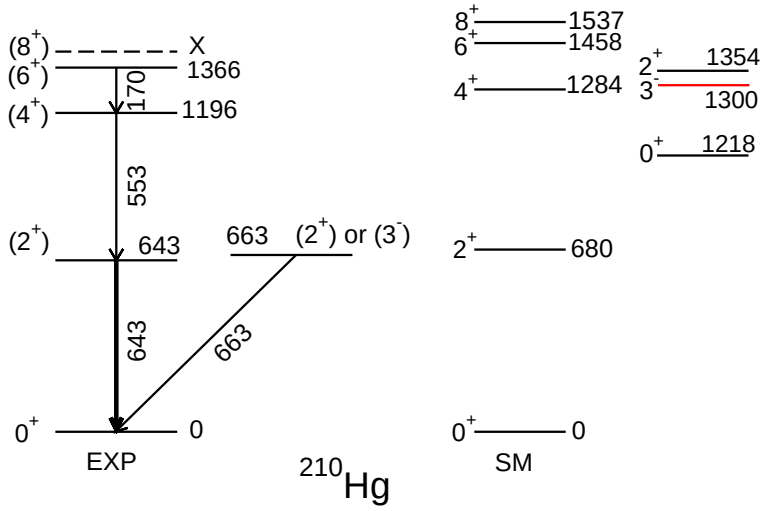

Figure 5.21: Level scheme proposed for ^{210}Hg compared with shell-model calculations performed with the interaction and valence space from Ref. [50]. The 3^- state, in red, is determined through particle-vibration coupling models [119].

In conclusion, it is difficult to firmly establish the level scheme of ^{210}Hg, also due to the low statistics, and uncertainties remain about the nature of the 663-keV state.

Ergo vivida vis pervicet et extra
processit longe flamentia moenia mundi
atque omne immensum peragravit mente animoque.[a]

De Rerum Natura – Titus Lucretius Carus

[a]The vivid force of his mind prevailed, and he fared forth far beyond the flaming ramparts of the heavens and traversed the boundless universe in thought and mind.

6 Conclusions

In the present thesis new results on the γ-decay spectroscopy of neutron-rich nuclei around lead have been presented. The production of unstable beams using the fragmentation of a primary uranium beam at relativistic energies and in-flight separation has proven an effective technique to study exotic nuclei. In the introductory chapter the main physical motivations for the study of exotic nuclei were outlined, pointing out the relevance of this research for both nuclear structure and nuclear astrophysics. The importance of the neutron-rich lead region was then described in this context. We also presented the main experimental challenges connected to the experiment, which were addressed in the following two chapters. The second and third chapters detailed the features of the experimental setup and the settings which were employed to overcome the aforementioned difficulties: a comprehensive description of the FRagment Separator FRS and of its detectors has been provided. A particular attention was also devoted to the description of the implantation setup and of the γ-ray array RISING. The detailed account of the technical features of the detectors is necessary to justify the choices made for the data analysis: the gates applied, the time circuits used and the isomer lifetime measurement. The experimental data were presented in chapter 4, providing for each isomer a measurement of its lifetimes and a first, tentative level scheme of the discovered nuclei, based on systematics and schematic theoretical arguments. While for even-even lead nuclei the results were quite clear, the interpretation of the data for nuclei below

the Z = 82 shell closure has revealed more difficult and it is not straightforward.
The main part of the theoretical analysis was focussed on the analysis of the neutron-rich lead isotopes. They were found to follow the expected seniority scheme in $(\nu g_{9/2})^n$ configuration, with the excited levels remaining almost at the same energy with the increasing number of neutrons. On the contrary, significant discrepancies were found in the E2 strengths from the isomeric 8^+ states. Although the B(E2)s follow the expected parabolic behaviour from the seniority-scheme, their absolute values are, in ^{212,214}Pb, a factor two less with respect to seniority-scheme predictions. Moreover, they are also in strong disagreement with predictions from realistic nuclear interactions, which in turn also exhibit a strong asymmetry around midshell not observed experimentally. It is not surprising that the interaction, which can predict the level energies quite accurately, fails in reproducing the B(E2) values: these are in fact much more sensitive to the nuclear wave function with respect to the energy spectrum. As a consequence, even small factors may induce significant changes in the final calculation. For example, in Ref. [96] a dependence on the particular occupied orbital in a single harmonic-oscillator major shell was found, against the usual tenet of shell model that effective charges are constant for all the orbitals belonging to the same harmonic-oscillator major shell. The introduction of effective charges that do not depend only on the shell, but even on the particular states involved in the transition, appears necessary to reestablish agreement with the experimental data in the even-even lead isotopes. However, we have shown that the inclusion of previously-neglected effective three-body forces (with the related two-body transition operators) improves the theoretical prediction preserving the midshell symmetry and reducing to about a factor two the discrepancy between calculated and measured B(E2) values for the lead isomers. This effect is visible even though the perturbation of the wave function is very small ($\sim$1%) when excitations from the core are introduced. Further studies are needed, as the approach adopted was useful to probe the effect of the inclusion of effective three-body forces but it is not a substitute for a full perturbative treatment. In particular, the coupling to the 3^- octupole excitation from the ^{208}Pb core appears an important step to improve the calculations. In conclusion, the results of the calculations for transition rates turn out to hinge on a delicate balance between different effects that tend to break and restore the $g^n_{9/2}$ dominance, which is reaffirmed by the quadrupole couplings and their related three-body effective forces studied. Nevertheless, the result is the regular seniority-like behaviour observed.
While the even-even lead isotopes have been found to provide a very interesting case pointing out the relevance of so far neglected effects, the situation is less clear for the other isomers. Apart from ^{217}Bi, whose level scheme is easy to interpret, ^{213}Pb, ^{211,213}Tl and ^{210}Hg are not fully understood in the framework of the calculations. The only isomers for which a quite reliable interpretation is found are $17/2^+$ in ^{211}Tl and 8^+ in ^{210}Hg. Interestingly enough, all these nuclei are somehow close or at the middle of the $\nu g_{9/2}$ shell: when crossing the midshell, a change from prolate to oblate deformation is expected. Moreover, for mercury and thallium the combination of proton holes and neu-

tron particles can also give rise to shape-coexistence phenomena. However, shell-model calculations do not give clear hints to the structure of these nuclei, but the validity of the interaction used for this proton-holes and neutron-particles valence space has not been tested enough. The most interesting case is ^{210}Hg, as it is an even-even nucleus and thus its structure should be easier to understand. If the assignment proposed is correct, the 2_2^+ state would be a unique case among all the nuclei studied so far.
Future investigations in this region are therefore imperative. On the one hand an increase in statistics appears essential in many of the cases studied (see next section), to be able to detect smaller decay branches and to perform more accurate $\gamma\gamma$ coincidence analysis. An implantation setup allowing to study conversion electrons would also be very important. On the other hand, further theoretical studies are demanded for this region. Besides the aforementioned full perturbative treatment for the even-even lead isotopes, a more reliable nuclear hamiltonian for mercury and thallium isotopes is necessary. Other approaches may also be attempted, using mean-field [118] or IBM2 [120] calculations to see weather there are indications of shape coexistence.

6.1 Future Perspectives

As mentioned in the introduction, the study of exotic nuclei is one of the major topics in modern nuclear physics. Their production and investigation is however a challenging technical and scientific issue. Consequently, several new facilities have been proposed and are now in the preparatory or construction phase.
There two main techniques to produce radioactive beams:

- ISOL (Isotope on-line separation): the exotic nuclei are obtained from the fission of a uranium target (induced by protons, neutrons or electrons), then extracted from the target, ionized and finally reaccelerated to be delivered to the experimental setups.

- In-flight separation: the exotic nuclei are produced from a fragmentation reaction at relativistic energies and then separated by a mass spectrometer to be used for in-beam or decay spectroscopy. This is the technique described in this thesis.

These two methods are complementary with respect to the production yield for different nuclei and to the physics that can be done with the beams made available. SPIRAL2 and SPES are among the most important developments for new-generation ISOL facilities. SPIRAL2 [121] is being built at the GANIL laboratory (Caen, France) and will use a high-intensity 200-kW deuteron beam which will impinge on a graphite rotating target generating a large flux of neutrons. The neutrons will induce fission of a uranium target and the exotic nuclei, once extracted and ionised, will be reaccelearated by a cyclotron up to 8 MeV·A. SPES (Selective Production of Exotic Species) [122] will be built at the LNL laboratory (Legnaro, Padova, Italy) and will produce the radioactive nuclei by

delivering a primary proton beam (8 kW power) in a uranium carbide target. The exotic nuclei will be reaccelerated by the ALPI LINAC at about 16 MeV·A.
However, the most relevant development for the present case – very heavy ions – is the FAIR (Facility for Antiproton and Ion Research) facility, being built at GSI, Darmstadt. Figure 6.1 shows the facility: it will address both hadronic and nuclear physics. For the nuclear structure part, the project of interest is NUSTAR (Nuclear STructure, Astrophysics and Reactions): it will exploit the in-flight beam separation technique to produce exotic beams with unprecedented intensities [123]. The mass separation will be performed with the new fragment separator Super-FRS [124, 125], which will improve the secondary beam purity. Due to the increased number of separation stages and to the improved detectors, the problem of uranium charge states will become less cumbersome. From this point of view, progresses are already being made at the existing FRS, in order to have detectors which can handle counting rate up to 1 MHz at the intermediate focal plane S2.

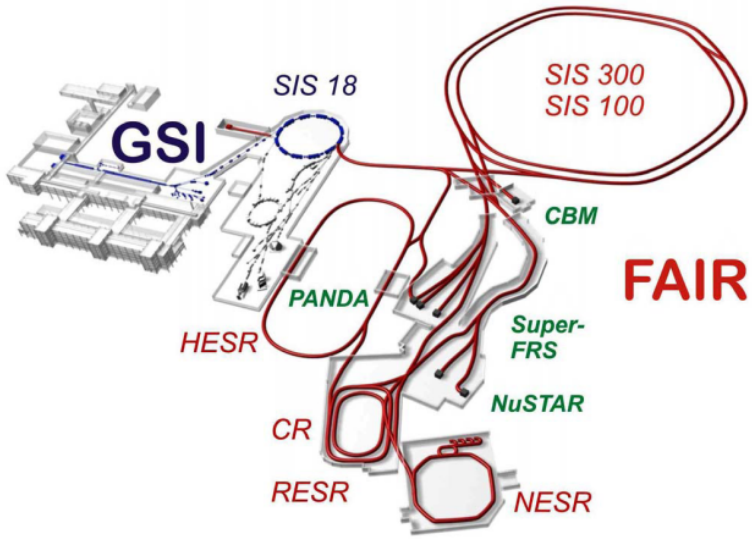

Figure 6.1: The future FAIR facility at GSI, Darmstadt. Acronyms: SIS 18, 100, 300 = synchrotrons with bending powers up to 18, 100 and 300 Tm, respectively; CR = Collector Ring; RESR = Accumulator Ring; NESR and HESR = low and high energy experimental storage rings, SuperFRS = Fragment Separator.

Other in flight facilities which are important to mention are FRIB [126, 127] , being built at MSU, East Lansing, USA and the recently commissioned RIBF [128, 129] facility, at the Riken laboratory, Tokyo, Japan. The latter is particularly interesting for the purpose of studying lead isotopes: it is already in operation and the mass spectrometers BigRips [130] and ZeroDegree, coupled to the γ-ray array EURICA [131], constitute a setup very similar to the one already successfully exploited at GSI.

Finally, another possibility offered by radioactive beam facility is to produce neutron-rich heavy nuclei in spallation reaction induced by high-energy protons on a uranium target. This method was attempted at ISOLDE, CERN, where the produced neutron-rich thallium nuclei were separated in mass and then implanted on a Si detector [132].
However, the developments concern not only the available intensity of the radioactive beams, but also the new detectors being built. It was already mentioned how our experiment benefited a much larger γ-ray efficiency with respect to the one in Ref. [39]. In this field, an unprecedented γ-ray detection efficiency (up to 40%) will be offered by the new array AGATA (Advanced GAmma Tracking Array) [133, 134]. AGATA is based on the technique of γ-ray energy tracking. This technique consists in the accurate determination of the energy, time and position of every interaction of a γ ray depositing its energy within the detector volume. This is possible thanks to the electrically segmented high-purity germanium crystals used and to the pulse-shape analysis of the signals produced. The spacial resolution achievable is of the order of 4 mm [133]. The reconstruction of the full interaction path results in the possibility of recuperating the Compton-scattering events which will otherwise be lost. As a consequence, this detector will have a very high efficiency, particularly at high energies, where the Compton scattering becomes dominant with respect to the photoelectric effect. The first five triple clusters of AGATA have already being built and installed at the Legnaro National Laboratories [134], see Fig. 6.2. In the future, AGATA will also be used for decay spectroscopy, allowing to detect weak γ transitions with its high efficiency.

In conclusion, the new radioactive beam facilities and experimental setups under construction or commissioning (as for example AGATA) will provide physicists unprecedent opportunities in the study of exotic nuclei. In the next ten to twenty years the knowledge of the atomic nucleus will probably advance at the same path of the glorious days of Rutherford's discovery.

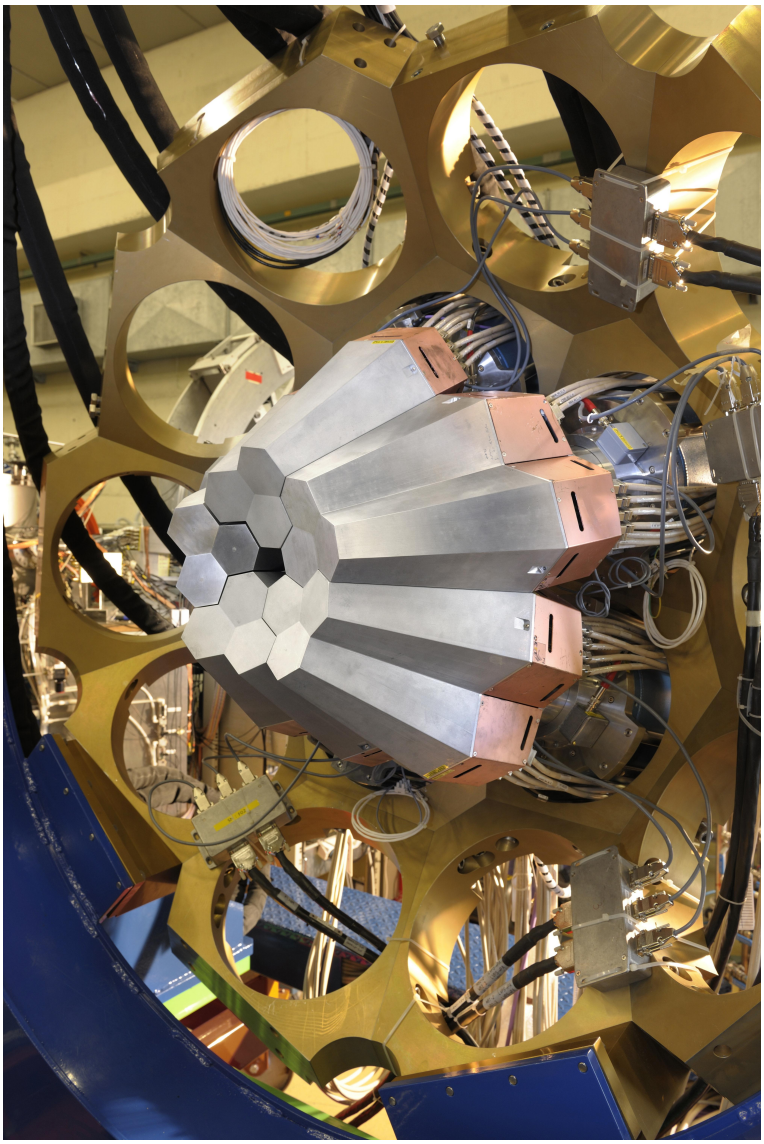

Figure 6.2: The AGATA Demonstrator array installed at the Legnaro National Laboratories. The five triple-clusters (fifteen crystals in total) are inside the aluminum casing.

Bibliography

[1] Rutherford, E. *Philosophical Magazine* **21**, 669 (1911).

[2] Dobaczewski, J. et al. *Phys. Rev. Lett.* **72**, 981 (1994).

[3] Sharma, M. M. and Farhan, A. R. *Phys. Rev.* **C65**, 044301 (2002).

[4] Wiringa, R. B. and Pieper, S. C. *Phys. Rev. Lett.* **89**, 182501 (2002).

[5] McCutchan, E. A. et al. *Phys. Rev. Lett.* **103**, 192501 (2009).

[6] Zuker, A. P. *Phys. Rev. Lett.* **90**, 042502 (2003).

[7] Otsuka, T. et al. *Phys. Rev. Lett.* **105**, 032501 (2010).

[8] Michel, N. et al. *Phys. Rev. Lett.* **89**, 042502 (2002).

[9] Betan, R. I. et al. *Phys. Rev. Lett.* **89**, 042501 (2002).

[10] Cederwall, B. et al. *Nature* **469**, 68 (2011).

[11] Goeppert-Meyer, M. and Jensen, J. D. H. *Elementary Theory of Nuclear Shell Structure*. John Wiley and Sons Inc., (1955).

[12] Caurier, E. et al. *Rev. Mod Phys.* **77**, 427 (2005).

[13] Holt, J. D. et al. *arXiv:1009.5984* (2010).

[14] Bohr, A. and Mottelson, B. R. *Nuclear Structure, Vol. I: Single-Particle Motion*. World Scientific Publishing, (1998).

[15] Blatt, J. M. and Wiesskopf, V. F. *Theoretical Nuclear Physics*. John Wiley and Sons Inc., (1952).

[16] de Sahlit, A. and Feshbach, H. *Theoretical Nuclear Physics Vol I: Nuclear Structure*. John Wiley and Sons Inc., (1974).

[17] Ring, P. and Schuck, P. *The Nucler Many Body Problems*. Springer-Verlag, (1980).

[18] Krane, K. S. *Introductory Nuclear Physics.* John Wiley and Sons Inc., (1988).

[19] Kibédi, T. et al. *Nucl. Instr. and Meth.* **A589**, 202 (2008).

[20] Kibédi, T. et al. `http://bricc.anu.edu.au/`, (2008).

[21] de Sahlit, A. and Talmi, I. *Nuclear Shell Theory.* Dover Publications, (1963).

[22] Casten, R. F. *Nuclear Structure from a Simple Perspective.* Oxford University Press, (2001).

[23] Broda, R. et al. *Phys. Rev. Lett.* **68**, 1671 (1992).

[24] Zhang, C. T. et al. *Phys. Rev.* **62**, 057305 (2000).

[25] Jungclaus, A. et al. *Phys. Rev. Lett.* **99**, 132501 (2007).

[26] Fogelberg, B. and Carlé, P. *Nucl. Phys.* **A323**, 205 (1979).

[27] Isacker, P. V. *Int. J. Mod. Phys.* **E20**, 191 (2011).

[28] Talmi, I. *Simple Model of Complex Nuclei.* Harwood, (1993).

[29] Burbidge, E. M. et al. *Rev. Mod. Phys.* **29**, 547 (1957).

[30] Motobayashi, T. et al. *Phys. Lett.* **B346**, 9 (1995).

[31] Scheit, H. et al. *Phys. Rev. Lett.* **77**, 3967 (1996).

[32] Sorlin, O. and Porquet, M.-G. *Prog. Part. Nucl. Phys.* **61**, 602 (2008).

[33] Otsuka, T. et al. *Phys. Rev. Lett.* **95**, 232502 (2005).

[34] Otsuka, T. et al. *Phys. Rev. Lett.* **97**, 162501 (2006).

[35] Otsuka, T. et al. *Phys. Rev. Lett.* **104**, 012501 (2010).

[36] Hoffman, C. R. et al. *Phys. Rev. Lett.* **100**, 152502 (2008).

[37] Janssens, R. V. F. *Nature* **459**, 1069 (2009).

[38] Browne, E. *Nucl. Data Sheets* **99**, 649 (2003).

[39] Pfützner, M. et al. *Phys. Lett.* **B444**, 32 (1998).

[40] Borzov, I. N. *Phys. Rev.* **C67**, 025802 (2004).

[41] Benlliure, J. et al. *Nucl. Phys.* **A660**, 87 (1999).

[42] Sümmerer, K. and Blank, B. *Phys. Rev.* **C61**, 034607 (2000).

[43] Gaimard, J. J. and Schmidt, K. H. *Nucl. Phys.* **A531**, 709 (1991).

[44] Bazin, D. et al. *Nucl. Inst. and Meth.* **A482**, 307 (2002).

[45] Eisenberg, Y. *Phys. Rev.* **96**, 1378 (1954).

[46] Schmidt, K. H. et al. *Phys. Lett.* **B300**, 313 (1993).

[47] Browne, E. *Nuclear Data Sheets* **99**, 649 (2003).

[48] Lane, G. J. et al. *Phys. Lett.* **B606**, 34 (2005).

[49] Kurpeta, J. et al. *Eur. Phys. J.* **A18**, 31 (2003).

[50] Al-Dahan, N. et al. *Phys. Rev.* **C80**, 061302(R) (2009).

[51] Pietri, S. et al. *Nucl. Instr. Meth.* **B261**, 79 (2007).

[52] Regan, P. H. et al. *Nucl. Phys.* **A787**, 491c (2007).

[53] `http://www.gsi.de/portrait/ueberblick.html`, (2011).

[54] `http://www-inj.gsi.de/index.php?section=3&subsection=1`, (2011).

[55] `http://www.gsi.de/beschleuniger/sis18/Sections.html`, (2011).

[56] Geissel, H. et al. *Nucl. Instr. Meth.* **B70**, 286 (1992).

[57] Dufour, J. P. et al. *Nucl. Instr. Meth.* **A248**, 267 (1986).

[58] Caamaño, M. et al. *Eur. Phys. J.* **A23**, 201 (2005).

[59] Wollink, H. *Optics of Charged Particles*. Accademic Press Inc., (1987).

[60] Stelzer, H. et al. *Nucl. Instr. Meth.* **A310**, 103 (1991).

[61] `http://www-linux.gsi.de/~weick/frs/mwpc.html`, (2011).

[62] Janik, R. et al. *Nucl. Instr. Meth.* **A640**, 54 (2011).

[63] `http://www-w2k.gsi.de`, (2009).

[64] `http://personal.ph.surrey.ac.uk/~phs1pr/rising/`, (2011).

[65] Baumann, T. www.nscl.msu.edu, (2001).

[66] Kumar, R. et al. *Nucl. Instr. Meth.* **A598**, 754 (2009).

[67] Regan, P. H. et al. *Prog. Part. Nucl. Phys.* **E17**, 8 (1992).

[68] Eberth, J. et al. *Int. J. Mod. Phys.* **28**, 495 (2008).

[69] X-ray Instumentation Associates. User's Manual: Digital Gamma Finder. (2004).

[70] Weick, H. et al. `http://www-linux.gsi.de/~weick/mocadi/u`, (2011).

[71] Tarasov, O. B. and Bazin, D. *Nucl. Instr. Meth.* **B266**, 4657 (2008).

[72] Scheidenberger, C. et al. *Nucl. Inst. Meth.* **B142**, 441 (1998).

[73] Audoin, L. et al. *Nucl. Instr. Meth.* **A548**, 517 (2005).

[74] `http://www-win.gsi.de/go4/`, (2010).

[75] Grebosz, J. *Comp. Phys. Comm.* **176**, 251 (2007).

[76] Brun, R. `http://root.cern.ch/drupal/`, (2010).

[77] Steer, S. J. *Isomer Decay Spectroscopy of N≤126 Neutron-Rich Nuclei.* PhD dissertation, University of Surrey, Department of Physics, October (2008). PhD Thesis.

[78] Mineva, M. N. *Spectroscopic Studies of Isomers Produced in Relativistic Projectile Fragmentation and In-Flight Fission.* PhD dissertation, Lunf University, Department of Physics, September (2004). PhD Thesis.

[79] Steer, S. J. et al. *Phys. Rev.* **C84**, 044313 (2011).

[80] Górska, M. et al. *Phys. Lett.* **B672**, 313 (2009).

[81] Wollersheim, H. J. et al. *Nuc. Instr. and Meth.* **A537**, 637 (2005).

[82] `radware.phy.ornl.gov`, (2000).

[83] Blomqvist, J. et al. *Nucl. Phys.* **A544**, 45 (1993).

[84] Antonot, B. et al. *Nucl. Instr. Meth.* **B99**, 513 (1995).

[85] Kondev, F. G. *Nucl. Data Sheet* **109**, 1527 (2008).

[86] Decman, D. J. et al. *Phys. Rev.* **C28**, 1060 (1983).

[87] Ellegaard, C. et al. *Nucl. Phys.* **A170**, 209 (1971).

[88] Walen, R. J. and Bastin, G. *Compt.Rend.Congr.Intern.Phys.Nucl.* , 910 (1959).

[89] Chumin, V. et al. *Z. Phys.* **A358**, 33 (1997).

[90] Kuo, T. T. S. and Brown, G. *Nuc. Phys.* **A85**, 40 (1966).

[91] Machleidt, R. et al. *Phys. Rev.* **C53**, R1483 (1996).

[92] Bogner, B. et al. *Phys. Rev.* **C51**, 38 (1995).

[93] Dufour, A. and Zuker, A. P. *Phys. Rev.* **C54**, 1641 (1996).

[94] Duflo, J. and Zuker, A. P. *Phys. Rev.* **C59**, R2347 (1999).

[95] Bohr, A. and Mottelson, B. R. *Nuclear Structure, Vol. II: Nuclear Deformations.* World Scientific Publishing, (1998).

[96] Valiente-Dobón, J. J. et al. *Phys. Rev. Lett.* **102**, 242502 (2009).

[97] Rowe, D. J. and Rosensteel, G. *Phys. Rev. Lett.* **87**, 172501 (2001).

[98] Rosensteel, G. and Rowe, D. J. *Phys. Rev.* **C67**, 014303 (2003).

[99] Escuderos, A. and Zamick, L. *Phys. Rev.* **C73**, 044302 (2006).

[100] Isacker, P. V. and Heinze, S. *Nucl. Instr. Meth.* **B142**, 441 (1998).

[101] Isacker, P. V. private communication, (2010).

[102] Kitching, J. E. et al. *Phys. Lett.* **B32**, 343 (1970).

[103] Grawe, G. et al. *Progr. Part. Nucl. Phys.* **38**, 15 (1997).

[104] Sawicka, M. et al. *Phys. Rev.* **C68**, 044304 (2003).

[105] Maglione, E. private communication, (2010).

[106] Warburton, E. K. and Brown, B. A. *Phys. Rev.* **C43**, 602 (1991).

[107] Caurier, E. et al. *Phys. Rev.* **C67**, 054310 (2003).

[108] Caurier, E. and Nowacki, F. *Acta Phys. Pol.* **B30**, 705 (1999).

[109] Caurier, E. and Martinéz-Pinedo, G. *Nucl. Phys.* **A704**, 60 (2002).

[110] Górska, M. et al. *Phys. Rev. Lett.* **79**, 2415 (1997).

[111] Hamamoto, I. *Phys. Rep.* **10**, 63 (1974).

[112] Rejmund, M. et al. *Eur. Phys. J.* **A8**, 161 (2000).

[113] Kovar, D. G. et al. *Nucl. Phys.* **A231**, 266 (1974).

[114] Poves, A. and Zuker, A. *Phys. Rep.* **81**, 141 (1981).

[115] Poves, A. et al. *Phys. Lett.* **B82**, 319 (1979).

[116] Hosaka, A. et al. *Nucl. Phys.* **A444**, 76 (1985).

[117] Warburton, E. K. *Phys. Rev.* **C44**, 233 (1991).

[118] Shen, Y.-S. et al. *Phys. Rev.* **C59**, 172 (1999).

[119] Hamamoto, I. *Phys. Rep.* **10**, 63 (1974).

[120] Iachello, F. and Arima, A. *The Interacting Boson Model*. Cambridge University Press, (2006).

[121] `http://www.ganil-spiral2.eu/spiral2-us`, (2011).

[122] `http://www.lnl.infn.it/~spesweb/`, (2011).

[123] `http://www.gsi.de/forschung/fair-experiments/NUSTAR/index.html`, (2010).

[124] Geissel, H. et al. *Nucl. Instr. and Meth.* **B247**, 368 (2006).

[125] Winkler, M. et al. *Nucl. Instr. and Meth.* **B266**, 4275 (2009).

[126] `http://frib.msu.edu/`, (2011).

[127] Cho, A. *Science* **322**, 1777 (2008).

[128] Yano, Y. *Nucl. Instr. Meth.* **B261**, 1009 (2007).

[129] Normille, D. and Cho, A. *Science* **314**, 1678 (2006).

[130] Kubo, T. *Nucl. Instr. Meth.* **B204**, 97 (2003).

[131] `http://ribf.riken.jp/EURICA/index.php?FrontPage`, (2012).

[132] Cocolios, T. private communication, (2011).

[133] Akkoyun, S. et al. *Nucl. Instr. Meth.* **A668**, 26 (2012).

[134] Gadea, A. et al. *Nucl. Instr. Meth.* **A654**, 88 (2011).

Our life is brief: we are always referring to centuries which preceed or follow our own as if they were totally alien to us, but I have come close to them in my play with stone. These walls which I reinforce are still warm from contact with vanished bodies; hands yet unborn will caress the shafts of these columns.

Memoirs of Hadrian – Marguerite Yourcenar

Acknowledgments

After three years of PhD it would be long to remember all the people who helped me in the data analysis, in preparing the papers, in not getting too bored during experiments... Not all moments were a pleasure, but on overall I cannot avoid to admit that these three years have been terrific! I particularly enjoy to travel in different countries and continents for conferences and experiments. Among the most beautiful places, I remember the wonderful landscapes of the Yosemite and Death Valley national parks (Nuclear Structure Conference 2010) and the charming, relaxing quietness of Vancouver (International Nuclear Physics Conference 2010).
Therefore, I think I should thank INFN (Istituto Nazionale di Fisica Nucleare) first, since it gave me the opportunity to visit so many places during my studies, allowing me not only to see and use the different nuclear-physics facilities available in world but also to get in contact with different cultures and different working philosophies.
Then I have to thank all the colleagues who helped me in running the experiment presented in this thesis and in doing the data analysis. José Javier has been a cornerstone for these last years with his help, his support and his advices (ehm... orders!). Prof. Lunardi was also always present with his experience and precious advices.
I have also to mention all the people who collaborate with me for my experiment, and in particular Sthepan, Plamen, Helmut Wieck, Zsolt, Fabio for their fundamental help in running so successfully the experiment. My deepest thanks also go to Jurek and to his very nice and user-friendly analysis programs (yes, there are user-friendly analysis programs!).
As one can easily infer from this thesis, I also worked a lot with theoreticians. Frédéric, Kamila, and Etienne Caurier introduced me to the secrets of shell-model calculations with their very instructive courses and their patience in dealing with all my questions and mistakes. A special mention goes to Enrico Maglione and Andres Zuker, whose deep insight into the problems of modern theoretical nuclear physics made me more aware of my own field of research.
Finally I also remind all my collegues and friends who supported me in this years: the two Daniele(s), especially the one who traveled with me in California, Eda, the two Enrico(s), Dino, Andres and his "you are a criminal!", Daniel, Silvia, Giacomo, Giovanna, Roberto, Anabel, Francesco, Caterina, Calin, Maria, Victor, Anna...
Also my "private" friends helped and supported me: Carlo, Rebecca, Enrico, Matteo,

the three Marco(s), Simone, Giulio, Tanio, Stefano, Davide, Marcello... Without them, these three years would have been terribly boring! A big thank also to my family for supporting me!

List of Tables

List of Figures